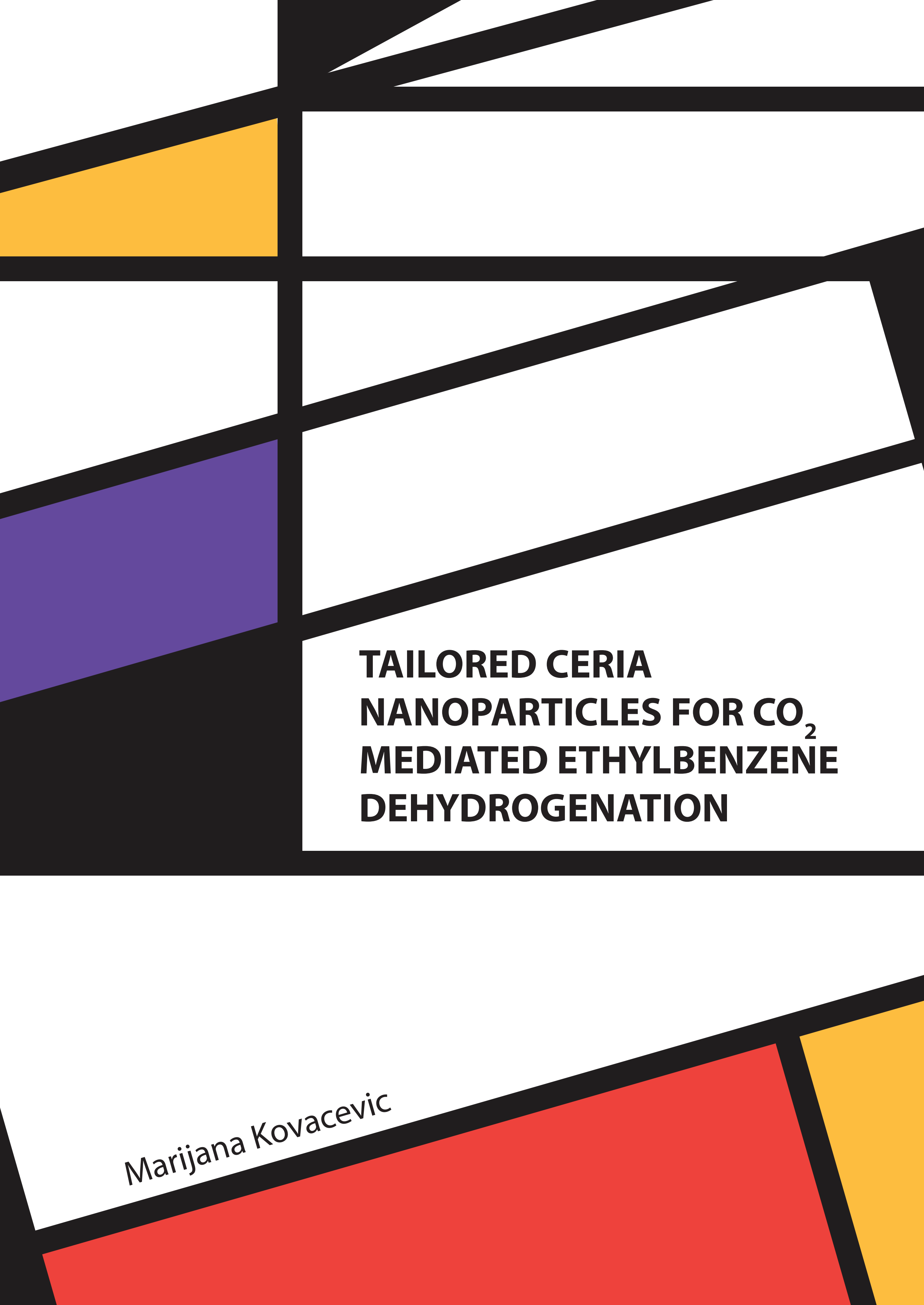

TAILORED CERIA NANOPARTICLES FOR CO_2 MEDIATED ETHYLBENZENE DEHYDROGENATION

Marijana Kovacevic

TAILORED CERIA NANOPARTICLES FOR CO_2 MEDIATED ETHYLBENZENE DEHYDROGENATION

Marijana Kovacevic

Graduation committee:

Prof. dr. ir J. W. M. Hilgenkamp, chairman	University of Twente, NL
Prof. dr. ir. L. Lefferts, promoter	University of Twente, NL
Dr. J. G. van Ommen, co-promoter	University of Twente, NL
Prof. dr. G. Mul	University of Twente, NL
Prof. dr. ir. N. E. Benes	University of Twente, NL
Prof. dr. ir. H. J. Heeres	RU Groningen, NL
Prof. dr. ir. M. Makkee	TU Delft, NL/ Politecnico di Torino, IT
Dr. R. Terorde	BASF, NL

The research described in this thesis was carried out at the Catalytic Processes and Materials (CPM) group of the University of Twente, The Netherlands. I acknowledge financial support for this research from *ASPECT*, *Advanced Sustainable Processes by Engaging Catalytic Technologies* (Project No. 05362021).

Cover design concept: Lolin Ivana and Marijana Kovacevic

Cover design: Off Page, Amsterdam, The Netherlands

Cover images: *Shkitov, M.*, Collection of infographics elements options in flat business Mondrian style, retrieved from http://www.shutterstock.com/s/mondrian/search.html

Publisher: Gildeprint, Enschede, The Netherlands

Copyright © 2016 by Marijana Kovacevic

All rights reserved. No part of this book may be reproduced or transmitted in any form or by any means, including but not limiting electronic, mechanical, photocopying, recording, or otherwise, without prior permission of the author.

ISBN: 978-90-365-4130-5

TAILORED CERIA NANOPARTICLES FOR CO_2 MEDIATED ETHYLBENZENE DEHYDROGENATION

DISSERTATION

to obtain
the degree of doctor at the University of Twente,
on the authority of the rector magnificus,
Prof. dr. H. Brinksma,
on account of the decision of the graduation committee,
to be publicly defended
on Wednesday 1st June 2016 at 16:45

by

Marijana Kovacevic

born on 31st July 1979
in Belgrade, Serbia

This thesis has been approved by:

Prof. dr. ir. L. Lefferts, promoter

and

Dr. J. G. van Ommen, co-promoter

Mojoj dragoj mami

To my dear mother

Toliko je bilo u životu stvari kojih smo se bojali. A nije trebalo.

Trebalo je živeti.

Ivo Andric

TABLE OF CONTENTS

Summary 1

Samenvatting 3

1 General introduction 7

1.1 Introduction 8

1.2 Cerium oxide, ceria 8

  1.2.1 Ceria defects and Mars Van Krevelen mechanism 8

  1.2.2 Low index ceria facets: structure and reactivity 11

  1.2.3 Effects of morphology in ceria catalysis 14

1.3 Commercial styrene synthesis 16

1.4 RWGS reaction 17

1.5 EB dehydrogenation in the presence of CO_2 18

  1.5.1 The role of acid-base properties for EBDH 20

  1.5.2 The role of redox properties in EBDH 20

1.6 Scope and outline of thesis 21

Bibliography 23

2 Calcination effects on $CeZrO_x$ geometry and styrene production from ethylbenzene 29

2.1 Introduction 30

2.2 Experimental part 31

  2.2.1 Materials 31

  2.2.2 Catalyst preparation 31

  2.2.3 Catalyst characterization 31

  2.2.4 Catalytic testing 32

2.3 Results 32

  2.3.1 Catalysts characterization 32

  2.3.2 Catalytic testing 35

2.4 Discussion 37

  2.4.1 The effect of calcination temperature on ceria structure 37

  2.4.2 The effect of calcination temperature on ethylbenzene dehydrogenation with CO_2 38

2.5 Conclusion 40

Appendix 2 41

Bibliography 42

3 The effects of morphology of cerium oxide catalysts for dehydrogenation of ethylbenzene to styrene 45

3.1 Introduction 46

3.2 Experimental 47

  3.2.1 Materials 47

  3.2.2 Catalyst preparation 47

3.2.3 Catalyst characterization 47
3.2.4 Catalytic testing 48
3.3 Results 48
3.3.1 Characterization of fresh catalysts 48
3.3.2 Catalytic testing 50
3.3.3 Characterization of spent ceria catalysts 52
3.4 Discussion 53
3.4.1 Effect of shape on performance after deactivation 53
3.4.2 Changes in performance with time on stream 56
3.4.3 Characterization of the spent ceria catalysts with Raman spectroscopy 59
3.5 Conclusion 61
Appendix 3 62
Bibliography 66

4 Effects of morphology of cerium oxide catalysts for reverse water gas shift reaction 69
4.1 Introduction 70
4.2 Experimental part 71
4.2.1 Materials 71
4.2.2 Catalyst preparation 71
4.2.3 Catalyst characterization 71
4.2.4 Catalytic testing 72
4.3 Results and discussion 72
4.3.1 Catalysts synthesis and characterization 72
4.3.2 Catalytic testing results in RWGS reaction 75
4.3.3 Discussion 76
4.4 Conclusion 78
Appendix 4 79
Bibliography 80

5 Conclusions and outlook 83
5.1 Conclusions 84
5.2 General recommendations 87
5.2.1 High surface area cubes 87
5.2.2 Ceria nanotubes 87
5.2.3 Cerium nanocubes with enhanced defect sites abundancies 88
5.2.4 More detailed characterization of low-coordinated sites 88
5.2.5 Swing experiments. Oxidation role of CO_2 88
Appendix 5 90
Bibliography 92

Scientific contributions 95
Acknowledgments 97

SUMMARY

In this thesis we investigated CO_2 mediated ethylbenzene dehydrogenation (EBDH) as a model reaction in order to probe intrinsic surface reactivity of tailored cerium oxide nanoparticles.

Ethylbenzene dehydrogenation is one of the ten most important petrochemical processes at present. It is commercially employed for styrene synthesis, the fourth utmost essential bulk monomers nowadays. Styrene monomer gained particular attention in modern petrochemical/ polymer industry owning to its highly reactive double bond which facilitates it's self-polymerization and polymerization with other monomers.

Current commercial styrene synthesis proceeding via the EBDH is however a highly energy demanding process. Being highly endothermic, hence energy intensive reaction is favored at higher temperature in presence of super-heated steam. Several alternatives to steam, conventionally used to supply heat have been widely investigated. It has been suggested that CO_2 can in principle replace stream as long as the catalyst is able to active it. Concept of using CO_2 as a mild oxidant is based on the thermodynamics , revealing that styrene yield at equilibrium can be clearly enhanced when EBDH is coupled with a reverse water gas shift reaction (RWGS).

Cerium oxide apparently is able to active CO_2 and EBDH has been proposed in literature to proceed via Mars Van Krevelen (MvK) mechanism over cerium oxide nanoparticles. Reactions proceeding via a MvK mechanism were exhibit morphology dependant behaviour over ceria catalysts, which has been further related with the ease of an oxygen species abstraction following the trend: (110) < (100) < (111) and corresponding stability of these surfaces decreasing as follows (111) > (110) > (100). The working hypothesis of this thesis was that EBDH would exhibit similar structure-performance behaviour.

The contribution of this thesis to understanding the structure-performance in catalysis, is particularly in extending the scope of the reactions investigated so far over cerium oxide nanoshapes from small model compounds (CO, H_2, CH_4 investigated so far in literature) towards more industrially relevant applications/ more complex reactants (such as ethylbenzene, EB). Furthermore, the effects of the CO_2 addition as a mild oxidant for the catalytic activity/ selectivity/ stability of ceria nanoparticles for EBDH are reported.

In chapter 2 we report on the effects of increasing calcination temperature on $CeZrO_x$ activity/selectivity/stability in CO_2 mediated EBDH. A series of $CeZrO_x$ catalysts were prepared by calcination of hydrothermally obtained metal oxide precipitate at increasing temperatures in air. All the investigated nanoshapes exhibited a sharp conversion decline within the initial 2 h time on stream. This has been attributed to the initial active oxygen species depletion resulting in an enhanced by-products formation. Differential catalytic testing results in semi-steady state clearly revealed that the catalytic activity of these ceria nanoshapes steadily decreases at increasing calcination temperatures. High resolution scanning electron microscopy (HRSEM), X-ray diffraction (XRD) and Raman spectroscopy respectively revealed a particle morphology alteration from cubic to spherical, an average crystallite diameter increase and an oxygen vacancy annihilation with increasing calcination temperature. These results suggested that (100) crystal planes enclosing $CeZrO_x$ cubes

exhibit higher inherent abundancy and greater intrinsic reactivity of oxygen vacancies in CO_2 mediated EBDH as compared to (111) facets exposed at $CeZrO_x$ spheres.

In chapter 3 EBDH in presence and absence of CO_2 was investigated over CeO_2 catalysts of distinct morphologies: cubes, rods, and particles. Differential catalytic testing results revealed that presence of CO_2 apparently enhances the amount of oxygen species available via a Mars Van Krevelen mechanism, prolonging the time window in which by-products are formed initially. CO_2 addition however exhibited no effects on the catalytic activity/ selectivity/ stability once these ceria nanoshapes attained the stable operation. After oxygen species have been depleted and stabile oxidation state of the catalyst is attained, reaction was found to proceed via a two-step pathway: a direct EBDH followed by a consecutive RWGS reaction.

We further used Raman spectroscopy as a finger print technique to characterize the degree of lattice distortion/ reduction of the spent ceria catalysts. Removal of surface oxygen species at various low index ceria surfaces was qualitatively in agreement with the formation of oxygen vacancies and lattice distortion as reveled by Raman spectroscopy. Results presented suggested that ceria cubes having specifically exposed (100) crystal planes of low intrinsic stability apparently provide more oxygen species during initial formation of CO, benzene and toluene. In semi-steady operation these ceria nanoshapes exhibited a remarkable higher activity per m^2 for EBDH as compared to rods and particles suggesting that stable styrene formation proceeds at partially reduced surface sites.

Finally, in Chapter 4, CeO_2 catalysts of distinct morphologies: cubes, rods, and particles have been probed for a reverse water gas shift reaction (RWGS). Catalytic testing under differential conversion of CO_2 revealed similar trends of the catalytic activity: cubes >> rods ~ particles as observed in EBDH. WGS is well known in literature to proceed *via* active hydroxyl species (–OH) on the ceria surfaces. Ceria cubes, exposing (100) facets as previously found in our group exhibit discrete interaction with CO, compared to rods and octahedra, resulting in enhanced reactivity in WGS. Catalytic testing results in RWGS suggested that superior catalytic activity of ceria cubes in RWGS is caused by highly inherently reactive (100) facets exposed at ceria cubes contrary to relatively inert (111) crystal planes enclosing rods and particles.

Results presented in this thesis clearly demonstrated that cerium oxide cubes enclosed by highly reactive (100) crystal planes exhibit twice higher intrinsic reactivity as compared to rods and particles for the model reactions investigated: EBDH, CO_2 mediated EBDH and a RWGS reaction.

SAMENVATTING

In dit proefschrift is onderzoek beschreven aan CO_2-gemediëerde ethylbenzenedehydrogenatie (EBDH) als modelreactie ten behoeve van het bepalen van de intrinsieke oppervlakte reactiviteit van specifieke ceriumoxide (ceria) nanodeeltjes.

Ethylbenzeendehydrogenatie is momenteel één van de tien belangrijkste petrochemische processen en wordt commercieel toegepast voor styreen synthese, wat tegenwoordig gezien wordt als de vierde essentiële bulk monomeer. Styreenmonomeer is zo belangrijk geworden in de petrochemische/polymeer industrie vanwege de hoog-reactieve dubbele binding die zelfpolymerisatie en polymerisatie met andere monomeren mogelijk maakt.

De huidige commerciële methode voor styreensynthese, middels EBDH, kost echter veel energie. Dit is vanwege de zeer endotherme reactie condities, d.w.z. een hoge temperatuur in combinatie met zeer heet stoom. Derhalve zijn een aantal alternatieven voor stoom, dat in genoemde conventionele methode gebruikt wordt om de warmte te voorzien, op grote schaal onderzocht. Er is gesuggereerd dat CO_2 in principe stoom kan vervangen, mits de katalysator het kan activeren. Het concept van het gebruik van CO_2 als milde oxidator is gebaseerd op thermodynamica, die stelt dat evenwichtsopbrengst van styreen aanmerkelijk verhoogd kan worden als EBDH gepaard gaat met een omgekeerde *water gas shift* reactie (RWGS).

In de literatuur is gesuggereerd dat ceriumoxide actief is met CO_2 en EBDH volgens het Mars Van Krevelen (MvK) mechanisme op ceriumoxide nanodeeltjes. Tevens lijken reacties die volgens een MvK-mechanisme verlopen een morfologie-afhankelijk gedrag te vertonen voor ceria katalysatoren. Dit kan verder gerelateerd worden aan de mate van opname van zuurstof volgens de trend: (110) < (100) < 111) en bijbehorende stabiliteit van deze vlakken, welke als volgt afneemt: (111) > (110) > (100). De werkhypothese voor het onderzoek zoals beschreven in dit proefschrift is dan ook dat EBDH hetzelfde gedrag zou vertonen als functie van de structuur van de deeltjes.

De bijdrage van dit proefschrift was het creëren van meer katalytisch begrip/inzicht met betrekking tot de invloed van de structuur van deeltjes, en specifiek het uitbreiden van het aantal onderzochte reacties op ceriumoxide nanodeeltjes, van kleine moleculen (CO, H_2 en CH_4) tot meer industrieel relevante toepassingen en meer complexe reactanten (zoals EB). Tevens zijn, als een van de eersten in literatuur, de effecten van het toevoegen van CO_2 op de katalytische activiteit van ceria nanodeeltjes in EBDH gerapporteerd.

Verhoogde calcinatietemperaturen in lucht van hydrothermaal metaaloxide precipitaat zijn gebruikt om de vorm en morfologie van $CeZrO_x$ katalysedeeltjes aan te passen, wat beschreven is in hoofdstuk 2. Van de op deze wijze verkregen ceria nanodeeltjes verandert de morfologie van kubusvormig naar bolvormig, en deze deeltjes zijn onderzocht op geschiktheid voor CO_2-gemediëerde EBDH. Alle onderzochte nanodeeltjes vertoonden een drastische afname in conversie gedurende de eerste 2 uur. Dit kan worden toegeschreven aan een vermindering van de initieel actieve zuurstofverbindingen, wat leidt tot een toename in vorming van bijproducten. Differentiële katalytische semi-stabiele testresultaten tonen duidelijk aan dat de katalytische activiteit van deze ceria nanodeeltjes gestaag afneemt voor hogere calcinatietemperaturen. Hoge resolutie *scanning* elektronen microscopie (HRSEM), röntgenstralen diffractie (XRD) en Ramanspectroscopie toonden een verandering van de deeltjesmorfologie van kubusvormig naar bolvormig voor hogere calcinatietemperaturen, een toename van de gemiddelde kristalgrootte en een vernietiging van zuurstofvacatures. Deze resultaten tonen aan dat (100)-kristalvlakken die $CeZrO_x$ kubussen begrenzen meer zuurstofvacatures met een hogere intrinsieke reactiviteit voor CO_2-gemediëerde EBDH hebben in vergelijking met (111)-vlakken die $CrZrO_x$ bollen omhullen.

In hoofdstuk 3 is onderzoek gedaan naar EBDH met/zonder CO_2 voor CeO_2 katalysedeeltjes met duidelijk waarneembare verschillende vormen: staafjes, kubussen en nanodeeltjes. Differentiële katalytische test-resultaten geven aan dat de aanwezigheid van CO_2 blijkbaar de hoeveelheid zuurstofsoorten vergroot via een MvK-mechanisme, welke leidt tot een vergroting van het tijdsbestek waarin bijproducten gevormd worden. Echter, de aanwezigheid van CO_2 leek geen effect te hebben op de katalytische activiteit/ selectiviteit/ stabiliteit van deze ceria nanovormen tijdens stabiele werking. Nadat zuurstofsoorten zijn uitgeput en een stabiele oxidatietoestand van de katalysator is bereikt, vindt de reactie plaats via een 2-staps pad: directe EBDH gevolgd door een RWGS reactie.

Ramanspectroscopie is toegepast om de mate van roostervervorming te bepalen dan wel reduktie van de ceria katalysatoren. De afname van oppervlakte zuurstofsoorten op lage index vlakken was kwalitatief gelijk aan de vorming van zuurstofvacatures en roostervervorming zoals voorkwam uit Ramanspectroscopie.

Deze resultaten suggeren dat ceria kubussen, met haar specifieke (100)-kristalvlakken met lage intrinsiek stabiliteit, blijkbaar meer zuurstofsoorten aanleveren tijdens de initiële vorming van CO, benzeen en tolueen. In semi-stabiele werking heeft deze ceria nanovorm voor EBDH een opmerkelijk veel hogere activiteit per m^2 in vergelijking met staafjes en nanodeeltjes, wat erop duidt dat stabiele styreenformatie plaatsvindt op gedeeltelijk gereduceerde oppervlakte plaatsen.

Tenslotte zijn deze ceria nanovormen (kubussen, staafjes en nanodeeltjes) toegepast voor RWGS reactie, zoals beschreven in hoofdstuk 4. Katalytische testen voor differentiële conversie van CO_2 gaf gelijke trends voor de katalytische activiteit als gevonden voor EBDH: kubussen zijn beter dan staafjes en nanodeeltjes. Eerder is in de literatuur gesteld dat WGS zich voortzet via actieve hydroxylsoorten (–OH) op de ceria-oppervlaktes. Kubussen van ceria, met aan het oppervlak (100)-vlakken, vertonen een discrete interactie met CO in vergelijking met staafjes en octahedrische nanodeeltjes, wat een versterkte reactiviteit gedurende WGS tot gevolg heeft. Katalytische testen voor RWGS suggereren dat de superieure katalytische activiteit van ceria kubussen het gevolg is van de hoge, inherent reactieve, (100)-vlakken die de ceria kubussen omhullen, dit in tegenstelling tot de relatief inert (111)-vlakken die staafjes en nanodeeltjes begrenzen.

De resultaten in dit proefschrift tonen duidelijk aan dat ceriumoxide kubussen, welke begrensd worden door (100)-kristalvlakken, een tweemaal hogere intrinsieke reactiviteit hebben (in vergelijking met staafjes en andere nanodeeltjes) voor de onderzochte modelreacties: EBDH, CO_2-gemediëerde EBDH en een RWGS reactie.

1

GENERAL INTRODUCTION

ABSTRACT

In this thesis we investigate the structure-activity relationship for CO_2 mediated ethylbenzene dehydrogenation over tailored cerium oxide nanoparticles. This introduction chapter discusses the structure, properties, and reactivity of these ceria nanoshapes, providing a state-of-the-art overview of direct and the soft oxidative ethylbenzene dehydrogenation. The introduction provides research goals and a short description of the content of each chapter.

1.1 INTRODUCTION

More than 90% of chemical manufacturing processes involve catalysis [1,2,3]. Catalysts accelerate a chemical reaction rate by decreasing its activation energy barrier. By facilitating the cleavage and formation of chemical bonds in reactant and product molecules, catalysts provide alternative reaction paths which are less energetic with a higher selectivity [4]. Heterogeneous catalysis is a surface phenomenon by which one or more reagents adsorb reversibly on a surface – typically a supported transition metal – on which subsequent reactions occur. By reducing at least one dimension of a catalytic particle to the nano scale (1-100 nm) several advantages are gained; surface to volume ratio increases and number of atoms exposed at the surface increases – this more efficiently utilizes potentially expensive metals. Additionally, band gap, intrinsic reactivity, and catalytic potential greatly alter [5,6].

By tailoring catalyst particle size and shape, surface reactivity at the nanoscale can be manipulated [7]. This is essential for improving fundamental understanding of the structure-performance relationships in catalysis and further a key in tailoring new and improving existent chemical processes.

1.2 CERIUM OXIDE, CERIA

Rare earth oxides are used in catalysis as electronic and structural promotors to enhance the activity, selectivity, and stability of catalysts [8]. Cerium is the most abundant rare earth metal in the Earth's crust (66,5 ppm), more abundant than common metals like copper, lithium, and tin [9]. Cerium belongs to the lanthanide group of the elements having an atomic number of 58 and electron configuration: [Xe] $4f^1 5d^1 6s^2$. It is present in III and IV oxidation states. Cerium (III) oxide Ce_2O_3 is unstable towards oxidation; at pressures above 10^{-40} atm of oxygen CeO_2 formation already occurs [10].

Cerium (IV) oxide, ceria (CeO_{2-x}, x=0-0.5) is commonly produced from cerium salts via precipitation, milling, hydrothermal synthesis, sol-gel, surfactant assisted and spray pyrolysis methods [11,12,13,14,15]. Ceria gained particular attention as a catalyst and active species support in catalysis due to its ability to switch reversibly between Ce^{3+} and Ce^{4+} under repetitive redox cycles while attaining stability in the fluorite lattice (CeO_{2-x}, x=0-0.5) [8,10,16]. Due to its availability and striking redox and acid-base properties ceria has been extensively investigated in academic and industrial research programs.

1.2.1 Ceria defects and Mars Van Krevelen mechanism

CeO_2 exhibits a fluorite crystal structure with a face-centered cubic unit cell, space group of Fm-3m and a lattice parameter of $a=5.41$ Å at room temperature [17]. Each cerium ion (gray sphere) is surrounded by eight equivalent oxygen anions (red sphere), and each anion is tetrahedrally coordinated by four cerium cations (Figure 1.1, right).

Crystal defects of ceria play an essential role in ceria surface chemistry. Primary atomic defects include vacant lattice sites, interstitials and foreign atoms. Foreign atoms may be present interstitially or substitutionary. Equal numbers of vacancies on anion sub-lattice and the anion interstitial atoms, when the cation lattice remains unperturbed is called

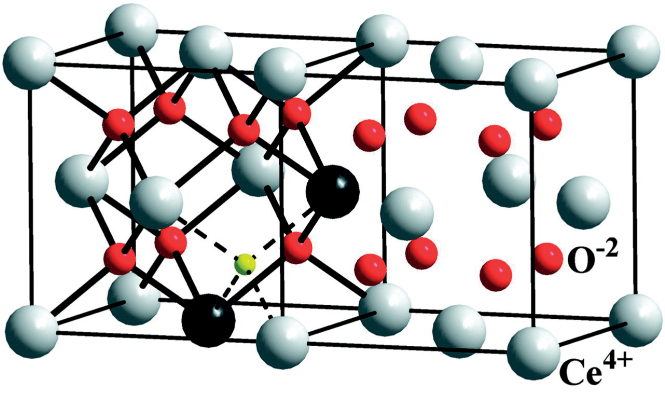

Figure 1.1 The crystal structure of doped ceria. In the right cube, the undoped CeO_2 is shown, whereas in the left cube, two of the cerium ions are replaced by trivalent ions from the lanthanide series (dark spheres) between which an oxygen vacancy appears (small sphere) [18].

Frenkel disorder. *Schottky* disorder stands for equal number of vacant sites on cation and anion sub-lattice [19].

The degree of the oxygen mobility in the ceria lattice is related to the size, type, dispersion, and abundance of oxygen (anion) vacancies [20,21,22]. Enhanced redox properties of ceria originate from its unique oxygen storage capacity (OSC), *i.e.* the ability to undergo repeated redox cycles formally switching between Ce^{3+} and Ce^{4+} in the stable fluorite lattice [18]. Vacancy formation can be described in *Kröger-Vink* notation (eq. 1.1) where $O^{\times}_{O}$ and $V^{\bullet\bullet}_{O}$ denote oxygen and vacancy at the normal lattice oxygen positions, respectively, while $Ce^{\times}_{Ce}$ and Ce'_{Ce} represent Ce^{4+} and Ce^{3+} at the positions normally occupied by the Ce^{4+} cations, respectively.

$$O^{\times}_{O} + 2Ce^{\times}_{Ce} \rightarrow V^{\bullet\bullet}_{O} + 2Ce'_{Ce} + 1/2O_2(g) \qquad \text{(eq. 1.1)}$$

By decreasing particle size of a ceria nanoparticle from 60 to 4 nm oxygen vacancy abundancy is reported to increase by even two orders of magnitude [23]. Another way of manipulating the oxygen vacancy content in the ceria lattice is by adding lower valence dopants. Figure 1.1. (left) illustrates oxygen vacancy formation (small sphere) when two ceria ions are replaced by trivalent ions from the lanthanide series (dark spheres). Addition of iso-valent zirconia (*Zr*) to ceria is reported to greatly enhance O ion mobility in the (distorted) fluorite lattice significantly increasing ceria reducibility [24]. Substitution of Ce^{4+} by Zr^{4+} can be described in *Kröger-Vink* notation, where $Zr_{Ce}{}^{x}$ denotes Zr^{4+} present at the site normally occupied by a Ce^{4+}.

$$ZrO_2 \rightarrow Zr_{Ce}{}^{x} + 2O^{x}_{O} \qquad \text{(eq. 1.2)}$$

Activation energy of O ion migration was found to uniformly decrease with the amount of zirconia added [25]. Isotopic transient studies further revealed a clearly higher OSC in $Ce_xZr_{(1-x)}O_2$ compared to pure ceria samples, which has been attributed to bulk phase contribution

[26]. *Memontov et al*. interestingly observed a relation between the OSC of these samples and the amount of interstitial oxygen species in the lattices [27]. Formation of interstitial O species (*$O''i$*) can be described in *Kröger-Vink* notation:

$$O^{\times}_{O} \rightarrow V^{\bullet\bullet}_{O} + O''i \qquad \text{(eq. 1.3)}$$

Participation of lattice oxygen species in hydrocarbon partial oxidation was discovered in 1950s simultaneously by Mars Van Krevelen and researchers of SOHIO/ BP [28,29,30]. Equilibrium lattice-gas phase oxygen exchange constants were found to decrease with experiment time closely approaching theoretical values after an initial time [31,32]. This clearly indicated that lattice O species participate in the gas-solid exchange. Isotopically labeled oxygen exchange studies further demonstrated a strong relation between the O lattice exchangeability, metal-oxygen bond strength in these oxide lattices and corresponding selectivities (the ration of deep *vs.* selective oxidation) for partial oxidation of hydrocarbon reactions [31]. Most of ceria surface reactions proceed via a *Mars Van Krevelen* (*MvK*) mechanism involving: *(i)* oxygen atom transfer from the ceria surface/ lattice to a substrate, *(ii)* creation of a void (anion vacancy) at the surface, *(ii)* the vacancy diffusion across the surface and eventual adsorption of an oxygen atom from another molecule, and *(iv)* vacancy healing/ annihilation. The first step is often the rate determining step, oxygen lattice diffusion is assumed to proceed quickly.

On an industrial scale, the most important applications of ceria include: *Three Way Catalysts (TWC)*, *Fluid Catalytic Cracking (FCC)*, *Catalytic Wet Oxidation (CWO), and styrene synthesis* via *ethylbenzene dehydrogenation* [8,16]. *TWC* are highly efficient in reducing emission of NO_x, *CO* and hydrocarbons (C_xH_y) from gasoline engines. Catalysts consisting of a ceramic or metallic substrate coated with metal oxides and precious metals (platinum, palladium, rhodium) operate under oxygen rich and lean engine conditions. Unique ceria efficiency originates from the ability to reversible switch from stoichiometric to nonstoichiometric structure under repetitive oxygen lean and rich engine cycle, while attaining overall charge neutrality and stability in the lattice. By donating oxygen for oxidation of CO and hydrocarbons (C_xH_y) ceria undergoes reduction to sub-stoichiometric structure (*eq. 1.4 and 1.5*) re-establishing its stoichiometry (*eq. 1.6*) in the next engine cycle.

$$CeO_2 + x\,CO \rightarrow CeO_{2-x} + x\,CO_2 \qquad \text{(eq. 1.4)}$$

$$CeO_2 + C_xH_y \rightarrow CeO_{2-(2x+0,5y)} + x\,CO_2 + 0.5y\,H_2O \qquad \text{(eq. 1.5)}$$

$$CeO_{2-x} + x\,NO \rightarrow CeO_2 + 0.5x\,N_2 \qquad \text{(eq. 1.6)}$$

As a catalyst for diesel engines, cerium oxide precursors (cerium naphthenate and octoate solely or in combination with other metal additives) are added (typically 500 – 10 000 ppm) directly to the fuel promoting the low temperature combustion of solid impurities (*diesel soot*) [8,33]. In other words, during combustion, the metal oxide is formed and deposited in the filter of the engine. Direct contact of the catalyst with the soot (ceria is included in soot during its formation) ensures high catalysts efficiency [8]. As a compound of *FCC catalysts* ceria reduces harmful sulfur emission from *FCC* units by converting produced SO_2 initially to SO_3 which has been finally reduced to H_2S (*de-SOx*) [8,16,34]. Being a key compound for catalytic wet oxidation (*CWO*) which under a high oxygen pressure and elevated temperatures converts organic contaminants of waste water streams to less toxic compounds further suitable for biological degradation, ceria is particularly used in oxidation of lower carboxyl acids (acetic acid) and ammonia [8,35]. Moreover, ceria is a key dopant of commercial *K-Fe* catalyst for styrene monomer synthesis via ethylbenzene dehydrogenation [36,37]. *Ethylbenzene dehydrogenation (EBDH)* is a model reaction investigated in this thesis. For more details we refer to the section 1.3. In addition to these applications, as a support for active metal species ceria shows a noticeable activity for the low temperature WGS reaction [38,39], Preferential Oxidation of CO in access of H_2 (PROX) [40], steam reforming of biomass derived alcohols for producing hydrogen [41,42] and CO_2 hydrogenation [43]. Other applications of ceria include solid oxide fuel cells (SOFC) [44,45], solar fuel systems [46], oxygen sensors [47], oxygen permeation membranes [48], and biomedicine [49].

1.2.2 Low index ceria facets: structure and reactivity

Owning to the recent advancement in ceria preparation [50], nano crystallites of various morphology and size have been obtained exposing distinct coordinative unsaturation of oxygen and cerium at the surface and hence unique reactivity [51,52,53]. In other words, by tailoring crystallite morphology and size, predominant exposure of low index crystal terminations can be accomplished [7].

This is becoming a strategy in designing materials with desired catalytic activity. Among various morphologies obtained (tubes, wires, spindles, flowers, flakes, belts, stars) the most studied ceria morphologies include cubes and rods [55] next to ceria nanoparticles of irregular shape, octahedra [56], and polyhedra used as a reference (Figure 1.2).

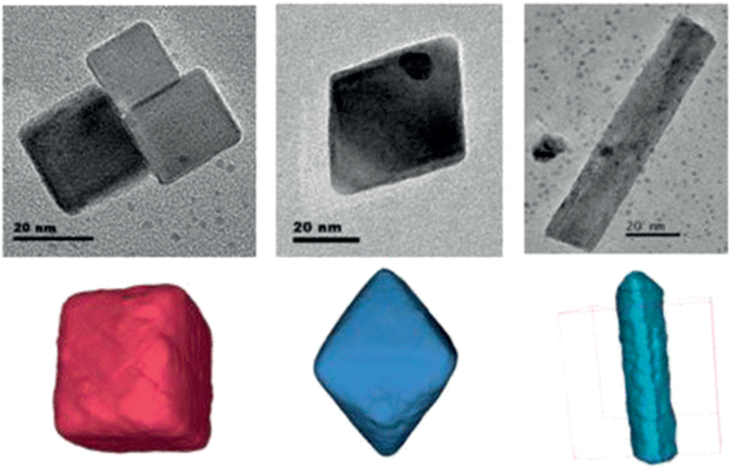

Figure 1.2. Representative transmission electron microscopy (TEM) images of the corresponding 3D models illustrating the three typical morphologies of CeO_2 nanoparticles prepared by the solvothermal method: (a) cubes, (b) octahedrons, and (c) rods [54].

Ceria nanoparticles are enclosed by mainly (111) crystal planes [57]. Contributions of other crystal facets become more prominent with decreasing particle size and with altering crystallite shape [52,53,58]. Ceria rods have been claimed previously to expose mainly (110) and (100) facets [59,60]. A recent aberration-corrected high-resolution transmission electron microscopy (AC-HRTEM) studies by our group at resolution below 1Å clearly revealed almost exclusive (111) facets exposed at this ceria morphology [58,61] in agreement with the findings of others [62,63,64,65]. Scanning transmission electron microscopy (STEM) images of these ceria rods are presented in Figure 1.3, where BF and HAADF denote bright field and (high angle annular) dark field imaging modes, respectively. FFT denotes the fast Fourier transforms.

Ceria rods possess a high degree of surface roughness, defects and pits complicating crystal plane assignments [54]. Ceria cubes are mainly enclosed by the (100) crystal planes [61,66]. A small portion of (110) facets are present at the edges, while (111) facets exist at the truncated corners of the cubes as recently revealed by AC-HRTEM [66,67].

Experimental observations indicate that O ions (red spheres) exclusively terminate (111) crystal planes of ceria; Ce layer (blue spheres) underneath is fully accessible (Figure 1.4a) [68].

The (110) surfaces are reported as terminated by both O and Ce ions (Figure 1.4b) [68,69]. Ideal (100) ceria crystal planes are terminated by solely O or Ce ions in such a way

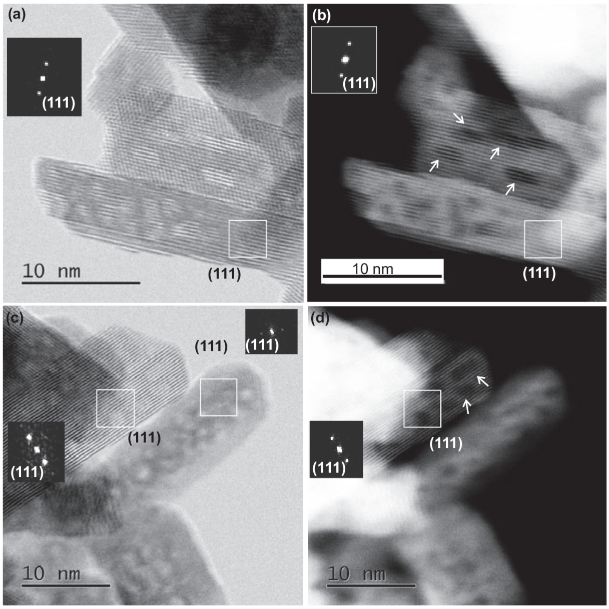

Figure 1.3. STEM images of CeO_2 rods. (a, c) BF images, (b, d) HAADF images. The inset in the figures is the FFT that allows indexing of the lattice planes. The rods expose (111) surfaces and have surface steps along the length. Areas of light contrast can be seen in the BF image and these same areas look dark in the HAADF image. The HAADF images confirm that these low-contrast features are voids in the CeO_2 rods that are bounded by (111) surfaces. The contrast variation in the HAADF image suggests a rectangular profile in the cross-section [58,61].

that the layer underneath in not accessible (Figure 1.4c) [68,69]. This induces a strong polarity perpendicular to the surface and instability of these lattices [70]. The (100) ceria facets hence undergo significant surface reconstruction to attain stability [66,68,69,71] (Figure 1.4d).

Low index ceria crystal planes further exhibit a distinct intrinsic coordination of both Ce and O ions in the lattice [68,69]. Cerium is 7-, 6- and 6-fold coordinated, while oxygen is 3-, 3- and 2-fold coordinated at (111), (110), and (100) facets, respectively [68]. Relative stability of these surfaces clearly resample the order of these coordinations decreasing in the order: (111) > (110) > (100) [72]. Theoretical studies predicted that the energy required for oxygen vacancy formation/ oxygen extraction at these facets, increases in the order: (110) < (100) < (111) [73]. It is expected that reactivity of these low index surfaces for reactions involving lattice oxygen abstraction/ oxygen vacancy formation (*i.e.* oxidation/ oxidative dehydrogenation) would follow a reverse sequence (110) > (100) > (111).

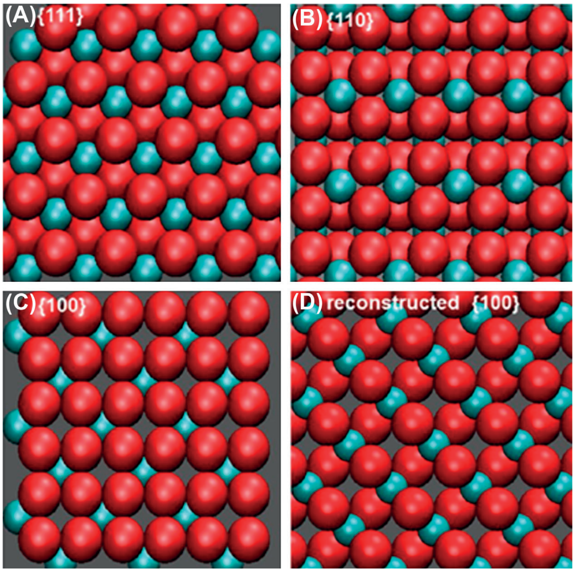

Figure 1.4. Top down view of the structural models for a fully oxidized CeO_2 (111), fully oxidized CeO_2 (110), fully oxidized CeO_2 (100), and fully oxidized reconstructed CeO_2 (100) surfaces. Red and light blue balls represent oxygen and cerium atom, respectively [69].

Density functional theory studies (DFT) elucidated the oxidation reactivity of: hydrogen [74,75], CO [76,77,78], methane [79] and soot over low index (111) and (110) surfaces, however, experimental validation of these studies is still pending. Oriented thin films are used to probe the surface reactivity of well-defined crystal planes in ultra-high vacuum (UHV). Though limited by a pressure and materials gap, compared to the real catalytic conditions, these studies are crucial in obtaining insights on the reactivity of specific crystal planes [80]. Materials gap refers to the fact that thin films possess very low surface area and usually complete absence of the surface defects hence deviating significantly from real catalytic structures.

Theoretical and experimental findings indicate that reactivity of low index ceria surfaces the oxidation of CO decreases in the order: (111) > (100) >(110) clearly resembling the order of the energy required for an oxygen vacancy formation at these crystal planes [81]. CO_2 adsorption and activation have been studied over ceria and magnesia/ ceria oriented thin films [82,83]. It has been revealed that stoichiometric CeO_2 (111) and (110) surfaces do not activate CO_2. Formation of carbonates/ carboxylates was, however, observed on the partially reduced CeO_{2-x} (111) facets at room temperature. Interestingly, both stoichiometric and reduced (100) ceria facets activate the CO_2 at room temperature, resulting in a carbonate formation. CO_2 is, however, reported not to be able to re-oxidize reduced (100) surfaces (at 180K, upon θ= 5 *L*) [84]. Oxidizing ability of CO_2 was interestingly reported for partially reduced CeO_{2-x} (111) facets (at 300K and θ > 4000 *L*) [85]. Similarly, 2-propanol was reported to oxidize reduced CeO_{2-x} (111), showing apparently no effects on the oxidation state of CeO_{2-x} (100) crystal planes [86]. Fundamental studies revealed higher inherent reactivity of (100) surfaces with methanol [87], water [88], acetaldehyde [89], and acetic acid [86] compared to the (111) crystal planes.

1.2.3 Effects of morphology in ceria catalysis

Despite the rapid progress in catalyst characterization techniques during the past decade, structure performances relationships in (ceria) catalysis remained insufficiently comprehended. This has been largely attributed to the "ill-defined" structures of the catalysts (nano-powders) previously investigated [80].

The most studied model reaction on ceria is the oxidation of CO [90]. The reaction proceeds via a *MvK* mechanism, where often the rate limiting step is a lattice oxygen abstraction and oxygen vacancy creation at the ceria surface [7,90]. Theoretical studies, to recall, predicted easier oxygen specie extraction from (110) and (100) surfaces of rods and cubes, respectively, as compared to (111) facets exposed at nanoparticles (nano-octahedra, nano-polyhedra). This is further related to a lesser stability and lower coordination of O species at these low index ceria crystal planes (Figure 1.4) [80].

Ceria nanoshapes have been investigated in NO reduction [91], WGS reaction [92], methanol and ethanol reforming [7,93]. Ceria rods a showed superior activity in the oxidation of CO, 1,2-dichlorethane, ethyl acetate, naphthalene, ethanol [7,94,95,96,97,98], and catalytic conversion of CO_2 with methanol compared to other studied morphologies [64]. *Zhou et al*. revealed that ceria nanorods possess a greater reducibility and hence superior activity for the oxidation of CO compared to nanoparticles of irregular morphology [60]. *Mai et al*. demonstrated that both ceria cubes and rods possess higher OSC compared to octahedra [59] originating from both surface and bulk structure, while in case of octahedra it is solely bulk restricted. Ceria nanorods, possessing higher degree of oxygen vacancy clustering at exposed (111) facets [62], further showed higher activity for CO oxidation [94] in agreement with the previously suggested mechanism of oxygen ion diffusion at ceria surface/ lattice *i.e.* via diffusion of oxygen vacancies by hopping of lattice oxygen at temperatures higher than 400°C [99]. Temperature programmed desorption studies (TPD) using isotopically labelled oxygen clearly revealed that lattice oxygen exchangeability decreasing from rods to cubes and finally octahedra apparently resemble the activity trends of these nanoshapes in oxidation of the CO [94].

Wu et al. and *Mann et al.* revealed distinct reactivity of low index ceria surfaces for the methanol and acetaldehyde decomposition [69,100]. Distinct surface coordination of *Ce* and *O* at low index ceria crystal planes exposed at various morphologies are apparently directly linked to the acidity and basicity of exposed crystal planes [80]. Lower O and Ce coordinations induce higher basicity and acidity at these surfaces.

Supported and pure ceria cubes interestingly displayed twice higher activity in the oxidation of hydrogen and ethanol as well as in WGS reaction compared to rods and particles [57,58,61,101]. In addition, ceria cubes gained particular attention as a promising catalyst for the selective oxidation of toluene [102]. Superior reactivity of cubes for the oxidation reactions have been related to the enhanced low temperature reducibility of this morphology compared to rods and octahedra [59,103]. Enhanced reactivity for WGS has been attributed to the distinct –OH groups existing at exposed (100) crystal planes of cubes displaying discrete interaction with CO as compared to –OH groups at (111) crystal facets of rods and particles [58,61].

As indicated, enhanced OSC of ceria cubes positively affects the corresponding catalytic activity in oxidation reactions. Ageing effects at increasing temperatures were reported to lead to an increased OSC at both particles and cubes diminishing the reactivity of ceria nanoparticles for the hydrogenation of C_2H_2 and enhancing the reactivity of cubes in the oxidation of *CO* (Figure 1.5) [104].

Recently, ceria nanoshapes have been investigated in soot oxidation [105]. Ceria fibres/ nano-stars exhibited prominent activity for soot oxidation compared to ceria particles of irregular morphology. This has been attributed to enhanced reducibility induced by specific geometry favouring higher amount of low coordination sites [106,107,108].

Ceria cubes exhibited striking activity for total soot oxidation compared to rods further attributed to the enhanced abundancy of coordinative unsaturated atomic sites at exposed (100) facets as compared to (111) facets enclosing rods [105]. Thermal aging was interestingly reported to alter ceria morphology in such a way that staring either from ceria nanoparticles or cubes, alike crystallite geometry is accomplished characterized with optimal (111) and (100) crystal planes exposed ratio that further imply optimal reactivity of these ceria nanoshapes in both oxidation of CO and soot [109,110].

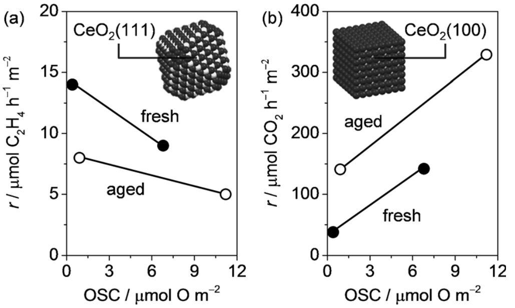

Figure 1.5 Reaction rate in C_2H_2 hydrogenation (a) and CO oxidation (b) as a function of the oxygen storage capacity (OSC) of the fresh and aged ceria catalysts. Both reactions were investigated at T= 473K.Conditions for the hydrogenation of acetylene: W_{cat}= 0.25 g (particle size= 0.2–0.4 mm), contact time t= 1 s, H_2/C_2H_2= 30 (acetylene concentration=2.5 vol%, He as balance gas), and total pressure P=1 bar. Conditions for CO oxidation: W_{cat}= 0.03 g (heating rate=10 K·min^{-1}), O_2/CO= 2.5 (CO concentration= 2 vol%, He as balancegas), F= 50 cm^{3}min^{-1}, and P=1 bar. Insets: the most active morphology in C_2H_2 hydrogenation (octahedron-like nanoparticles enclosed by (111) facets and CO oxidation (nanocubes enclosed by (100) facets. O dark grey, Ce light grey [104].

1.3 COMMERCIAL STYRENE SYNTHESIS

Styrene is a main building block for various polymers: polystyrene, styrene-butadiene, latex, styrene-acrylonitrile, and acrylonitrile-butadiene-styrene [111,112,113]. It is produced mainly (more than 90% worldwide) via ethylbenzene dehydrogenation (selectivity > 96.5%) (EBDH) (*eq. 1.7*); minor amounts are obtained from epoxidation of propene [8,112]. EBDH is one of the ten most important industrial processes [114].

Non-oxidative dehydrogenation:

$$C_6H_5\text{-}CH_2CH_3 \leftrightarrow C_6H_5\text{-}CH{=}CH_2 + H_2 \qquad \text{(eq. 1.7)}$$

$$\Delta H^{0}_{298} = 123.6\ \text{KJ·mol}^{-1}$$

Strongly endothermic [115] and a volume increasing, reaction is favoured at higher temperatures (typically 550-650˚C) and reduced pressures (0.4 bar) [112,116]. Steam is added as a diluent as conversion is thermodynamically limited. Steam also acts as a heat supplier and a coke gasifier as well as oxidant keeping active iron species in a higher oxidation state. The catalyst employed commercially is potassium promoted iron oxide based [112]. The process is, however, highly energy consuming, condensation and re-evaporation of steam is needed prior to its recycle resulting in significant energy (latent enthalpy) losses, hence alternative solutions to steam have been investigated [112,117,118]. Simultaneously, useful by-products i.e. benzene, toluene and hydrogen (high value energy carrier) are obtained.

Ethybenzene dehydrogenation in presence of oxygen (EBODH) (*eq. 1.8*) is suggested as a promising route to styrene. Being an exothermic reaction it proceeds at lower reaction temperatures (350-550°C) compared to conventional (550-650°C) dehydrogenation

[119,120,121,122]. Moreover, it is free of thermodynamic limitations implying significant conversion enhancement compared to non-oxidative dehydrogenation (*eq. 1.7*) [122]. However styrene selectivity remains rather moderate, products of over-oxidation are favoured in presence of such a strong oxidant.

Oxidative dehydrogenation [123]:

$$C_6H_5\text{-}CH_2CH_3 + \tfrac{1}{2}\,O_2 \rightarrow C_6H_5\text{-}CH{=}CH_2 + H_2O \qquad \text{(eq. 1.8)}$$

$$\Delta H^0_{298} = -116\ \mathrm{KJ \cdot mol^{-1}}$$

Carbonaceous deposits generated in the course of the reaction were suggested to act as active site precursors in EBODH [124,125,126]. Menon classified coke as: harmful, harmless, beneficial and invisible. EBODH is a typical reaction in which coke has been considered as beneficial [127]. Although low stability hinders potential application of carbon-based catalysts on a larger scale research interests in the past decades focused on: multi-walled nanotubes (MWNT´s), carbon nanofilaments (CNF´s), onion-like carbon (OLC), ultra-dispersed diamonds (UDD) [123,128]. Particularly high styrene selectivity (90-97%) have been reported in only few cases [122]. Mesostructured ceria shows a comparable activity with these catalysts in the presence of oxygen [129,130] operating, however, at lower selectivity (84%). High activity has been attributed to the enhanced reducibility of small ceria crystallites. *Nederlof et al*. recently reported that staged oxygen feeding clearly enhances styrene selectivity ~ 90-95% and yield in EBODH over P_2O_5/SiO_2 and Al_2O_3 [131]. However, commercial iron-oxide based catalysts still shows superior long time stability operating at styrene selectivity above 97%.

EBDH in the presence of oxygen is in general characterized by moderate selectivity to styrene due to extensive CO_x formation. This is further accompanied by the inability to control the process temperature (exothermic side reaction); particularly relevant in case of fixed bed operations. The amount of oxygen further is limited to only 10% in order to avoid flammable mixture of hydrogen and oxygen formation [122]. In addition, oxidation products are difficult to separate. Hence, alternative oxidants such as N_2O [132,133] and SO_2 have been proposed. Although affirmative results have been obtained at the laboratory scale, safety aspects [134] and toxic/corrosive by-products formation respectively, limit the potential usage of these oxidants at the industrial scale [135].

CO_2 has been suggested as a promising soft oxidant for EBDH [136]. In the gasification of coke, Bartholomew reported the following order of reactivity: $O_2(105) > H_2O(3) > CO_2(1) > H_2(0.003)$ [137], clearly indicating that, though less reactive than molecular oxygen and steam, CO_2 possess a considerable oxidizing ability.

1.4 RWGS REACTION

Utilization of carbon-rich fossil fuels including coal, oil, and natural gas in the past decades resulted in continuous increase of atmospheric CO_2 emission at present reaching to 400 ppm and further predicted to hit 570 ppm by the end of the century, hence truly affecting a global temperature increase [138,139]. Mitigation and utilization of CO_2 present a global need and challenge [140]. Despite its high thermodynamic stability, high oxidation state and low reactivity [141,142], CO_2 has been utilized in several cases such as synthesis of urea, formic acid, methanol [143], cyclic carbonates, lactone [144] and salicylic acid [145]. However, utilization of CO_2 is reported to be only ~115 Mt worldwide, while its emission is ~30 Gt (both expressed per annum) [141,146,147].

All these process are, however, highly energy intensive, *i.e.* external energy inputs are required and/or the presence of high free energy content substances (such as H_2, NH_3, amines) [148]. RWGS likewise is a promising path for CO_2 utilization (catalytic conversion) [138,148,149] providing that hydrogen is obtained from sustainable sources [138] and/or generated *in-situ* as in dehydrogenation processes. Benefits of reaction coupling for CO_2 utilization are extensively discussed by *Towler* and *Lynn* [150].

$$CO_2 + H_2 \leftrightarrow CO + H_2O \quad \Delta H^{0}_{298} = 41.6\ \mathrm{KJ{\cdot}mol^{-1}} \qquad \text{(eq. 1.9)}$$

The design and characterization of RWGS catalysts hence attracted particular attention in the last decade [138]. Catalyst employed in WGS are generally active in a reverse reaction RWGS, as expected from the principle of micro-reversibility. RWGS is an endothermic reaction [115] facilitated at elevated temperatures. Conventionally used copper based catalysts for WGS show prominent activity in RWGS. Reduced Cu species are apparently able to dissociate CO_2, however increasing temperature demand for the reaction results in sintering and activity decline of the copper based catalysts [138]. Addition of Fe in that respect, led to stability enhancement, preventing copper particle agglomeration [151]. Alternative catalysts, namely Ni and noble metals supported on alumina, silica, ceria, zeolite Y showed promising activity [138], however, stability due to coking remains unresolved.

Two extensively discussed mechanisms in literature for (R)WGS reaction are red-ox [152,153] and associative/formate decomposition [154,155,156]. The reaction proceeds via a bifunctional mechanism; CO is adsorbed/activated on the metal species whereas ceria support plays a role in H_2O activation. It has been suggested that oxygen deficient sites on ceria dissociatively activate water resulting in active –OH species regeneration and catalytic activity enhancement. In addition to the associative formate mechanism proposed over Pt/CeO_2 for WGS, associative formate mechanism with red-ox regeneration over Pt/ZrO_2 and both pathways occurring at Pt/TiO_2 at 300^0C have been suggested by our group the group of Lefferts [157,158]. Using DRIFT-MS studies and steady - state isotopic transient kinetic analysis (SSTKA) *Goguet et al.* clearly demonstrated carbonate formation at oxygen deficient ceria sites at 225^0C, as a key intermediate in RWGS over Pt/CeO_2 [159].

1.5 EB DEHYDROGENATION IN THE PRESENCE OF CO_2

CO_2 has been utilized for the oxidative conversions of alkanes, alkenes and alcohols, oxidative coupling of methane, and oxidative dehydrogenation of alkyl aromatics [117]. In the early 1940s *Balandin* [160] and *Zelinskii* [161] observed higher activity of iron, vanadium and chromium oxide towards *EBDH* in the presence of CO_2 compared to in its absence. In 1968, *Olson* [162] suggested that CO_2 consumes hydrogen produced in the dehydrogenation reaction via a RWGS hence shifting the reaction equilibrium towards the product side and elevating the styrene yield. Moreover, thermodynamic calculations clearly demonstrated that styrene yield increases from 76 to 85%, when steam is replaced by CO_2 (H_2O:EB=9:1) at 600^0C [163]. Besides, CO_2 was claimed to act as a coke gasifier via a reverse *Boudart* reaction [164] preventing the catalyst deactivation:

$$C + CO_2 \leftrightarrow 2CO \qquad \text{(eq. 1.10)}$$

Due to its high heat capacity CO_2 minimizes the hot spot phenomenon preventing reaction runaway [136]. CO_2 can be easily separated from the product stream requiring only heating before reuse. Hence, the overall process is much less energy demanding (estimated energy savings are about 60%) [165].

Considering that CO_2 is activated via either basic or redox sites [166] and that adsorption of EB as a soft base is favored on acid sites [167] design of an efficient catalyst shall consider the following functions: acid, basic and red-ox. Considerable research efforts have been made in designing the suitable (active, stable and selective) catalysts for EBDH in the past decades [168] including: unsupported mixed oxides [114,169], supported transition metal oxides lanthanides and alkali metals/ metal oxides and hydrotalcites. Nevertheless, all the catalysts displayed the (similar) deactivation patterns due to a coke deposition. Sb/V_2O_5 [169,170] and Fe_2O_3 on alumina [171] were the only catalytic systems accomplishing stable performances within 6 h time on stream (TOS).

EBDH in the presence of CO_2 proceeds either mainly via one step pathway where CO_2 directly interact with ethylbenzene (formally described as eq. 1.11) or via a two-step pathway, where CO_2 consumes hydrogen molecule via RWGS (eq. 1.9) following dehydrogenation step (eq. 1.7). *Mimura et al.* proposed a method to distinguish, which pathway is prevailing [171].

$$C_6H_5\text{-}CH_2CH_3 + CO_2 \leftrightarrow C_6H_5\text{-}CH{=}CH_2 + CO + H_2O \qquad \text{(eq. 1.11)}$$

Interestingly, in case of bare alumina CO_2 conversion was found to be similar in the presence and absence of dehydroenation, while with the addition of Na_2O it clearly increased in presence of EBDH [172]. This suggested different mechanism for CO_2 conversion over these two catalysts, *i.e.* a two-step pathway over alumina and one step pathway over Na_2O/ alumina. Similar observations have been reported by *Sun et al.*, *i.e.* over vanadia based catalysts the reaction was claimed to proceed mainly as a one-step pathway, whereas over chromium and iron based catalysts two step path was dominating [166]. Similarly, both reaction pathways have been suggested over vanadium, chromium and cerium catalysts supported on MCM-41 zeolite and activated carbon [173,174].

Higher RWGS activity in presence of dehydrogenation as demonstrated by *Nederlof et al.* might be ascribed to the enhanced H_2 activation due to its spillover at the coke layer(s) generated in the course of the dehydrogenation reaction [175].

1.5.1 The role of acid-base properties for EBDH

Acid–base properties play a vital role both in non-oxidative [176] and oxidative EBDH [177,178]. As proposed by *Sato et al.* [172], EB is activated on the acid sites, while basic sites participate in hydrogen abstraction from EB and CO_2 activation [136]. The extent of CO_2 activation depends on the metal ion ionization potential and its radii [136,179]. Common CO_2 activators are alkali and alkaline earth metals/metal oxides. K_2O was reported to possess a considerable coke gasification activity in the presence of CO_2 [180].

Zirconia based oxides have been extensively investigated in *EBDH* in the presence of *CO_2* [114]. Tetragonal zirconia exhibited prominent activity compared to that of monoclinic [181]. Optimal MnO_2 or TiO_2 addition enhances catalytic activity due to an amorphous phase stabilization [182]. Titania addition increases the number and strength of acid sites due to a new phase $TiZrO_2$ formation. K_2O was found to interact with strong acid sites tuning the catalytic activity [183]. TPO results clearly revealed dissociative chemisorption of CO_2 on ceria promoted zirconia-titania [184].

1.5.2 The role of redox properties in EBDH

Surface/lattice oxygen species play an essential role in oxidative dehydrogenation of hydrocarbons. The transfer of lattice oxygen species from the catalyst (metal oxide, MO_x) to the substrate results in metal oxide reduction to a lower valence state followed by water formation (eq. 1.12). CO_2 has been suggested to re-oxidize the consumed surface/lattice oxygen species (eq. 1.13) [115,136]:

$$\text{R-CH}_2\text{CH}_3 + MO_x \rightarrow \text{R-CH=CH}_2 + H_2O + MO_{x\text{-}1} \qquad \text{(eq. 1.12)}$$

$$MO_{x\text{-}1} + CO_2 \rightarrow MO_x + CO \qquad \text{(eq. 1.13)}$$

The ratio of water *vs*. hydrogen formed can be used to estimate to which extent the reaction proceeds via oxidative (eq. 1.11) *vs*. non-oxidative path (*eq. 1.7*). In early 1990s *Park et al*. suggested that EBDH proceeds via a (soft) oxidative pathway over iron oxide supported on ZSM-5 zeolite [185]. Highly defective Fe_3O_4 was claimed to dissociatively activate CO_2 resulting in CO and an active oxygen formation (*eq. 1.14)*. These oxygen species were further suggested to abstract hydrogen from ethylbenzene leading to styrene and water formation, integrally presented by *eq. 1.11*.

$$CO_2 \rightarrow CO + O \qquad \text{(eq. 1.14)}$$

Transient studies by *Saito et al.* clearly revealed that CO_2 is able to replenish consumed lattice oxygen species in Cr, V, and Fe based catalysts (*eq. 1.13*) [115]. Water formation in the absence of CO_2 has been observed only initially, after surface/ sub-surface oxygen species have been depleted the reaction proceeded as a non-oxidative dehydrogenation (*eq. 1.7*). In presence of CO_2, continuous water formation has been observed resulting in an enhanced styrene yield. The reaction has been suggested to proceed via a soft oxidative (one step) pathway (*eq. 1.11)* in addition to non-oxidative (*eq. 1.7)* after the initial stabilization.

Transient studies by others indicated that CO_2 re-oxidizes up to 25% of the consumed lattice oxygen species in EBDH over MnO_2-ZrO_2 [186], resulting in excellent catalyst stability. The most stable catalyst for EBDH in the presence of CO_2 reported in literature to date is a Sb promoted vanadium based catalyst [169,170]. Antimony addition enhances CO_2 dissociation (*eq. 14*) facilitating the redox cycle between the fully oxidized and reduced vanadium species. Hence generated active oxygen species further minimize coke accumulation at the catalyst surface via a coke gasification and prevent catalyst deactivation.

Watanabe et al. suggested that EBDH proceeds via a MvK mechanism over perovskite based catalysts in the presence of steam [187]. In presence of N_2O, EBODH has been suggested to occur via a MvK over ceria nanocrystallites (Scheme 1.1) [133]. Fundamental studies revealed that reaction proceeds at remarkably lower temperatures (598K) compared to non-oxidative dehydrogenation (873K). It should be noted that time on stream effects in this study have not been reported. Nevertheless, *a*uthors interestingly revealed a clear relation between the abundancy of surface Ce^{3+}-O^{-}-Ce^{4+}- defect type sites and the EB conversion rate clearly indicating that the activation of EB on these oxygen deficient ceria sites presents a rate-determining step [133]. These sites are replenished by oxygen species generated via N_2O dissociative adsorption (Scheme 1.1).

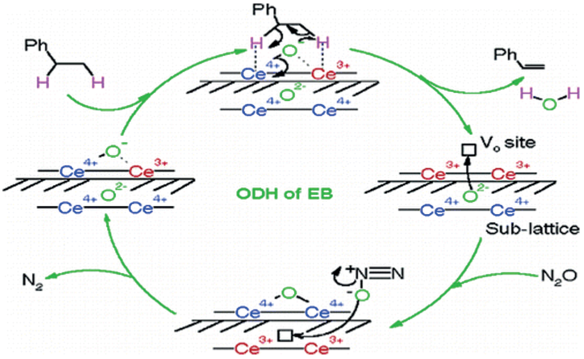

Scheme 1.1. Catalytic pathway for the EBODH using N_2O [133]

1.6 SCOPE AND OUTLINE OF THESIS

In general catalytic reactions can be facile or structure insensitive and structure sensitive - demanding [188]. In other words, the reaction rate can increase, decrease or show no relation with the catalyst particle size and morphology [189,190]. As discussed in Section 1.2.3. reactions proceeding via a MvK mechanism apparently show morphology dependant behaviour over ceria catalysts. The working hypothesis of this thesis was that ethylbenzene dehydrogenation (EBDH) would show similar structure-performance behaviour.

The aim of the thesis was moreover to investigate the effects of CO_2 addition as a soft oxidant for EBDH. CO_2 has been suggested to be able to re-oxidize ceria [191]. Isotopic exchange studies revealed that reduced ceria can be re-oxidized with $C^{18}O_2$ at temperatures above 200^0C [192].

The contribution of this thesis to understand the structure-performance in catalysis, is particularly in extending the scope of the reactions investigated so far over cerium oxide nanoshapes from small model compounds such as: CO, H_2, CH_4 towards more industrially relevant applications and more complex reactants (such as ethylbenzene, EB).

Chapter one of this thesis describes cerium oxide structure, properties and reactivity of low index ceria crystal planes, *i.e.* the effects of ceria morphology in catalysis. Conventional and alternative (oxidative) reaction pathways for styrene synthesis via ethylbenzene dehydrogenation are discussed. Two generally discussed mechanisms in literature *i.e.* acid-base and redox/ *Mars Van Krevelen,* for ethylbenzene dehydrogenation in the presence of CO_2 are shortly presented. Finally, at the end of the chapter the scope of the thesis is outlined.

In chapter two a series of $CeZrO_x$ catalysts are obtained by a gradually increasing calcination temperature of as prepared $CeZrO_x$ nanocubes. Catalysts were investigated in EBDH in the presence of CO_2. *Raman* spectroscopy characterization revealed that increasing calcination temperatures results in decreasing oxygen vacancy abundancies at these nanoshapes and their specific reactivity in EBDH due to the altered samples morphology from cubic to spherical at increasing calcination temperatures.

In chapter three the effects of ceria morphology (rods, cubes, particles of irregular morphology) were investigated in EBDH in the presence and absence of CO_2. The presence of CO_2 resulted in an increased byproducts formation, enhanced catalysts stability, showing, however, no effects after the initial stabilization. Ceria cubes exhibited twice higher activity per surface area as compared to rods and particles of irregular morphology. This has been attributed to the higher abundancy of active lattice oxygen species at (100) crystal planes at cubes as compared to (111) facets enclosing rods and particles. We suggest that these O species, consumed in nonselective EB conversion pathways generate the partly-reduced surface sites, which are active for the selective styrene formation.

In chapter four ceria nanoshapes (cubes, rods, and particles of irregular morphology) were investigated for the reverse water gas shift reaction (RWGS). Cerium oxide cubes exhibited twice higher activity per surface area as compared to rods and particles of irregular morphology. This has been ascribed to the greater inherent reactivity of (100) facets exposed at ceria cubes, contrary to the less inherently reactive (111) crystal planes of rods and particles.

Chapter five summarizes the results of the thesis and provides suggestions and recommendations for future research.

BIBLIOGRAPHY

1. J.N. Armor, Catal. Today 163 (2011) 3-9.
2. I. Fechete, Y. Wang, J.C. Vedrine, Catal. Today 189 (2012) 2-27.
3. F. Zaera, Chem. Soc. Rev 42 (2013) 2746-2762.
4. G. Boskovic, Heterogena kataliza u teoriji i praksi, Tehnoloski fakultet u Novom Sadu, Novi Sad, 2007.
5. R. Feynman, Eng. Sci. 23 (1960) 22-36.
6. A.I. Frenkel, C.W. Hils, R.G. Nuzzo, J. Phys. Chem. 105 (2001) 12689-12703.
7. Catalysis by materials with well-defined structures, (Ed: Z. Wu, S.H. Overbury) Elsevier, Amsterdam, 2015.
8. A. Trovarelli, C. de Leitenburg, M. Boaro, G. Dolcetti, Catal. Today 50 (1999) 353-367.
9. T.J. Ahrens, Global Earth Physics: A Handbook of Physical Constants. American Geophysical Union, Washington D.C., 1995.
10. A. Trovarelli, Catalysis by Ceria and Related Materials, vol. 12, pp.1-188 London, 2013.
11. C. Pan, D. Zhang, L. Shi, J. Fang, Eur. J. Inorg. Chem. 15 (2008) 2429-2436.
12. L.-S. Zhong, J.-S. Hu, A.-M. Cao, Q. Liu, W.-G. Song, L.-J. Wan, Chem. Mater. 19 (2007) 1648-1655.
13. G.Z. Chen, C.X. Xu. X.Y. Song, S.L. Xu, Y. Ding, S.X. Sun, Cryst. Growth. Des. 8 (12) (2008) 4449-4453.
14. C.C. Tang, Y.Bando, B.D.Liu, D.Golberg, Adv. Mater. 17 (2005) 3005-3009.
15. V.N. Satyanarayana, T.Kuchibhatla, Nanotechnology 18 (2007) 075303.
16. A. Trovarelli, Catal. Rev. -Sci. Eng. 38 (1996) 439.
17. L. Eyring, in: K.A.Gschneider, L.Eyring, M.B.Maple (Eds.), Handbook on the Physics and Chemistry of Rare Earths, vol. 3, Amsterdam, 1979.
18. K. Schwarz, Proc. Natl. Acad. Sci. U.S.A. 103 (2006) 3497.
19. R.A. Swalin, Thermodynamics of solids, Classification of defects in crystals, pp. 251-266, Willey, New York, 1961.
20. C.J. Zhang, A. Michaelides, D.A. King, S.J. Jenkins, Phys Rev B 79 (2009) 75433.
21. S. Babu, R. Thanneeru, T. Inerbaev, R. Day, A.E. Masunov, A. Schulte, S. Seal, Nanotechnology 20 (2009) 85713.
22. M.V. Ganduglia-Pirovano, A.Hofmann, J.Sauer, Surf. Sci. Rep. 62 (6) (2007) 219-270.
23. X.-D. Zhou, W. Huebner, Appl. Phys. Lett. 79 (2001) 3512-3514.
24. F. Zamar, A. Trovarelli, C. de Leitenburg, G. Dolcetti, J. Chem. Soc., Chem. Commun., 9 (1995) 965-966.
25. G. Balducci, J. Kašpar, P. Fornsiero, M. Graziani, M.S. Islam, J.D. Gale, J. Phys. Chem. B 101 (1997) 1750-1753.
26. Y. Madier, C. Descorme, A.M. Le Govic, D. Duprez, J. Phys. Chem. B 103 (1999) 10999-11006.
27. E. Mamontov, T. Egami, R. Brezny, M. Koranne, S. Tyagi, J. Phys. Chem. B 104 (2000) 11110-11116.
28. P. Mars, D.W. van Krevelen, Spec. Suppl. Chem. Eng. Sci. 3 (1954) 41–57.
29. R.K. Grasselli, Top. Catal. 21 (2002) 79-88.
30. R.K. Grasselli, SOHIO laboratory book assigned to the author in June 1952 and internal company reports (details are available in [29]).
31. C. Doornkamp, V. Ponec, J. Mol. Catal. A: Chemical 162 (2000) 19-32.
32. K. Klier, J. Novakova, P. Jiru, J. Catal. 2 (1963) 479-484.
33. E.S. Lox, B.H. Engler, E. Koberstain, Stud. Surf. Sci. Catal. 71 (1991) 291-321.
34. A.K. Bhattacharyya, G.M. Woltermann, J.S. Yoo, J.A. Karch, W.E. Cormier, Ind. Eng. Chem. Res. 27 (1988) 1356-1360.
35. Y.I. Matatov-Meytal, M. Sheintuch, Ind. Eng. Chem. Res. 37 (1998) 309-326.
36. T. Hirano, Appl. Catal. 28 (1986) 119-132.
37. A. Murakamy, H. Unei, M. Teranishi, M. Ohta, US Patent 5 190 906 (1993).
38. Q. Fu, A. Weber, M. Flytzani-Stephanopoulos, Catal. Lett. 77 (2001) 87-95.
39. Q. Fu, H. Saltsburg, M. Flytzani-Stephanopoulos, Science 301 (2003) 935-938.
40. M. Manzoli, G. Avgouropoulos, T. Tabakova, J. Papavasilova, T. Ionnides, F. Boccuzzi, Catal. Today 138 (2008) 239-243.
41. D.K. Liguras, D.I. Kondarides, X.E. Verykios, Appl. Catal. B: Environmental, 43 (2003) 345-354.
42. G.A. Deluga, J.R. Salge, L.D. Schmidt, X.E. Verykios, Science 303 (2004) 993-997.

43. A. Trovarelli, C. de Leitenburg, G. Dolcetti , J. Chem.Soc., Chem. Commun., 7 (1991) 472-473.
44. Z. Zhan, S.A. Barnett, Science 308 (2005) 844-847.
45. C.W. Sun, Z. Xie, C.R. Xia, H. Li, L.Q. Chen, Electrochem. Commun. 8 (2006) 833-838.
46. P. Furler, J.R. Scheffe, A. Steinfeld, Energy Environ. Sci. 5 (2012) 6098– 6103.
47. P. Jasinski, T. Suzuki, H.U. Anderson, Sens. Actuators B 4 (1991) 393-399.
48. K.S. Brinkman, H. Takamura, H.L. Tuller, T. Iijima, J. Electrochem. Soc, 157 (2010) 1852-1857.
49. A. Asati, S. Santra, C. Kaittanis, S. Nath, J.M. Perez, Angew. Chem. Int. Ed 48 (2009) 2308-2312.
50. Q. Yuan, H.-H. Duan, L.-L. Li, L.-D. Sun, Y.-W. Zhang, C.-H. Yan, J. Colloid Interface. Sci. 335 (2009) 151-167.
51. K. Zhou, Y. Li, Angew. Chem. Int. Ed. 51 (2012) 602-613.
52. D. Zhang, X. Du, L. Shi, R. Gao, Dalton Trans. 41 (2012) 14455-14475.
53. C. Sun, H. Li, l. Chen, Energy Environ. Sci. 5 (2012) 8475-8505.
54. I. Florea, C. Feral-Martin, J. Majimel, D. Ihiawakrim, C. Hirlimann, O. Ersen, Cryst. Growth Des. 13 (2013) 1110-1121.
55. Y. Li, W. Shen, Chem. Soc. Rev. 43 (2014) 1543-1574.
56. S. Agarwal, L. Lefferts, B.L. Mojet, ChemCatChem 5 (2) (2013) 479-489.
57. T. Dasaunay, G. Bonura, V. Chiodo, S. Freni, J.-P. Couzinie, J. Bourgon, A. Ringuede, F. Labat, C. Adamo, M. Cassir, J. Catal. 297 (2013) 193-201.
58. S. Agarwal, Surface chemistry of tailored ceria nanoparticles: Interaction with CO and H_2O, PhD Thesis, University of Twente, Enschede, 2015.
59. H.-X. Mai, L.-D. Sun, Y.-W. Zhang, R. Si, W. Feng, H.-P. Zhang, H.-C. Liu, C.-H. Yan, J. Phys. Chem. B 109 (2005) 24380 – 24385.
60. K. Zhou, X. Wang, X. Sun, Q. Peng, Y. Li, J. Catal. 229 (2005) 206-212.
61. S. Agarwal, L. Lefferts, B.L. Mojet, D.A.E. Ligthart, E.J.M. Hensen, D.R.G. Mitchell, W.J. Erasmus, B.G. Anderson, E.J. Olivier, J.H. Neethling, A.K. Datye ChemSusChem 6 (2013) 1898-1906.
62. X. Liu, K. Zhou, L. Wang, B.Wang, Y. Li, J. Am. Chem. Soc. 131 (2009) 3140-3141.
63. N. Ta, J.J. Liu, S. Chenna, P.A. Grozier, Y. Li, A. Chen, W. Shen J. Am. Chem. Soc. 134 (2012) 20585-20588.
64. S. Wang, L. Zhao, W. Wang, Y. Zhao, G. Zhang, X. Ma, J. Gong, Nanoscale 5 (2013) 5582-5588.
65. N.J. Lawrence, J.R. Brewer, L. Wang, T.-S. Wu, J. Wells-Kingsbury, M.M. Ihrig, G. Wang, Y.-L. Soo, W.-N. Mei, C.L .Cheung, Nano. Lett. 11 (2011) 2666-2671.
66. Y. Lin, Z. Wu, J. Wen, K.R. Poeppelmeier, L.D. Marks, Nano Lett. 14 (2013) 191-196.
67. S. Agarwal, B.L. Mojet, L. Lefferts, A.K. Datye in: Catalysis by Materials with Well-Defined Structures, (Ed: Z.Wu, S.H.Overbury), pp. 31-70, Elsevier, Amsterdam, 2015.
68. M.V. Ganduglia-Pirovano, A. Hofmann, J. Sauer, Surf. Sci. Rep. 62(6) (2007) 219–270.
69. Z. Wu, M. Li, D.R. Mullins, S.H. Overbury, ACS Catal. 2(11) (2012) 2224–2234.
70. P.W. Tasker, J. Phys. C: Solid State Phys. 12 (1979) 4977-4984
71. H. Norenberg, J.H. Harding, Surf. Sci. 477 (2001) 17-24.
72. M. Nolan, S. Grigoleit, D.C. Sayle, S.C. Parker, G.W. Watson, Surf. Sci. 576 (2005) 217-229.
73. T.X.T. Sayle, S.C. Parker, D.C. Sayle, Phys. Chem. Chem. Phys 7 (2005) 2936-2941.
74. H.-T. Chen, Y.M. Choi, M.Liu, M.C. Lin, ChemPhysChem 8 (2007) 849–855.
75. D. Marrocchelli, B. Yildiz, J. Phys. Chem. C 116 (2011) 2411–2424.
76. D.O. Scanlon, N.M. Galea, B.J. Morgan, G.W. Watson, J. Phys. Chem. C 113 (2009) 11095–11103.
77. M. Nolan, G.W. Watson, J. Phys. Chem. B 110 (2006) 16600–16606.
78. M. Huang, S. Fabris, J. Phys. Chem. C 112 (2008) 8643–8648.
79. D. Knapp, T. Ziegler, J. Phys. Chem. C 112 (2008) 17311–17318.
80. A.K.P. Mann, Z. Wu, S.H. Overbury in: Catalysis by Materials with Well-Defined Structures, (Ed: Z.Wu, S.H.Overbury), pp. 71-97, Elsevier, Amsterdam, 2015.
81. M. Nolan in: Catalysis by Materials with Well-Defined Structures, (Ed: Z.Wu, S.H.Overbury), pp. 159-192, Elsevier, Amsterdam, 2015.

82. Y. Lykhach, T. Staudt, R. Streber, M.P. Lorenz, A. Bayer, H.P. Steinruck, J. Libuda, Eur. Phys. J. B 75 (2010) 89–100.
83. T. Staudt, Y. Lykhach, N. Tsud, T. Skala, K.C. Prince, V. Matolin, J. Libuda, J. Phys. Chem. C 115 (2011) 8716–8724.
84. P.M. Albrecht, D. Jiang, D.R. Mullins, J. Phys. Chem. C 118 (2014) 9042–9050.
85. T. Staudt, Y. Lykhach, N. Tsud, T. Skala, K.C. Prince, V. Matolin, J. Libuda, J.Catal. 275 (2010) 181–185.
86. D.R. Mullins, P.M. Albrecht, F. Calaza, Top. Catal. 56 (2013)1345-1362.
87. D.R. Mullins, P.M. Albrecht, Langmuir 29 (2013) 4559-4567.
88. M. Molinari, S.C. Parker, D.C. Sayle, M.S. Islam, J. Phys. Chem. C 116 (2012) 7073–7082.
89. D.R. Mullins, P.M. Albrecht, J. Phys. Chem. C 117 (2013) 14692-14700.
90. S. Royer, D. Duprez, ChemCatChem 3 (2011) 24-65.
91. L. Liu, Y. Cao, W. Sun, Z. Yao, B. Liu, F. Gao, L. Dong, Catal. Today 175 (2011) 48-54.
92. R. Si, M. Flytzani-Stephanopoulos, Angew. Chem. Int. Ed. 47 (2008) 2884-2997.
93. N. Yi, R. Si, H. Saltsburg, M. Flytzani-Stephanopoulos, Energy Environ. Sci. 3 (2010) 831-827.
94. Z. Wu, M. Li, S.H. Overbury, J.Catal. 285 (2012) 61–73.
95. Q. Dai, H. Huang, Y. Zhu, W. Deng, S. Bai, X. Wang, G. Lu, Appl. Catal. B: Environ. 117-118 (2012) 360-368.
96. L. Torrente-Murciano, A. Gilbank, B. Puertolas, T. Garcia, B. Solsona, D. Chadwick Appl. Catal. B: Environ. 132-133 (2013) 116-122.
97. G. Zhou, B. Gui, H. Xie, F. Yan, Y. Chen, S. Chen, X. Zheng J. Ind. Eng. Chem. 20 (2014) 160-165.
98. M. Li, Z. Wu, S.H. Overbury, J.Catal 306 (2013) 164–176.
99. F. Esch, S. Fabris, L. Zhou, T. Montini, C. Africh, P. Fornasiero, G. Gomelli, R. Rosei, Science 309 (2005) 752-755.
100. A.K.P. Mann, Z. Wu, F.C. Calaza, S.H. Overbury, ACS Catal. 4 (2014) 2437-2448.
101. H. Li, G. Qi, Tana, X.Zhang, W.Li, W.Shen, Catal.Sci.Technol. 1 (2011) 1677-1682.
102. J. Lv, Y. Shen, L. Peng, X. Guo, W. Ding, Chem. Commun. 46 (2010) 5909-5911.
103. J. Zhang, H. Kumagai, K. Yamamura, S. Ohara, S. Takami, A. Morikawa, H. Shinjoh, K. Kaneko, T. Adschiri, A. Suda, Nano Lett. 11 (2011) 361-364.
104. G. Vil, S. Colussi, F. Krumeich, A. Trovarelli, J. Perez-Ramirez, Angew. Chem. Int. Ed. 53 (2014) 12069–12072.
105. M. Piumetti, S. Bensaid, N. Russo, D. Fino, Appl. Catal. B: Environ. 165 (2015) 742–751.
106. P.A. Kumar, M.D. Tanwar, S. Bensaid, N. Russo, D. Fino, Chem. Eng. J. 207-208 (2012) 258-266.
107. S. Bensaid, N. Russo, D. Fino, Catal. Today 216 (2013) 57-63.
108. P. Miceli, S. Bensaid, N. Russo, D. Fino, Nanoscale Res.Lett 9 (2014) 254-264.
109. E. Aneggi, J. Llorca, M. Boaro, A. Trovarelli, J. Catal. 234 (2005) 88-95.
110. E. Aneggi, D. Wiater, C. de Leitenburg, J. Llorca, A. Trovarelli, ACS Catal 4 (2014) 172-181.
111. E.H. Lee, Cat. Rev. -Sci. Eng. 8 (1973) 285-305.
112. F. Cavani, F. Trifiro, Appl. Catal A: Gen. 133 (1995) 219-239.
113. G.R. Meima, P.G. Menon, Appl. Catal. A: Gen. 121 (2001) 239-245.
114. B.M. Reddy, D.S. Han, N. Jiang, S.E. Park, Catal. Surv. Asia 12 (2008) 56-69.
115. K. Saito, K. Okuda, N.O. Ikenaga, T. Miyake, T. Suzuki, J. Phys. Chem. A 114 (2010) 3845-3854.
116. D.H. James, W.M. Castor in: Ullmann's Encyclopedia of Industrial Chemistry, Willey-VCH, 2002.
117. S.-E. Park, S.-C. Han, J. Ind. Eng. Chem. 10 (2004) 1257-1269.
118. C. Nederlof, Catalytic dehydrogenations of ethylbenzene to styrene, PhD Thesis, TU Delft, Delft, 2012.
119. D.B. Tagiyev, G.O. Gasimov, M.I. Rustamov, Catal. Today 102-103 (2005) 197-202.
120. M.F.R. Pereira, J.J.M. Orfao, J.L. Figueiredo, Appl. Catal. A: Gen. 184 (1999) 153-160.
121. M.F.R. Pereira, J.J.M. Orfao, J.L. Figueiredo, Appl. Catal. A: Gen. 196 (2000) 43-54.
122. V. Zarubina, Oxidative dehydrogenation of ethylbenzene under industrially relevant conditions. On the role of catalyst structure and texture on selectivity and stability, PhD Thesis, pp. 10-29, Reijksuniversiteit Groningen, Groningen, 2015.
123. N. Maximova, Partialdehydrierung von Ethylbenzol zu Styrol an Kohlenstoffmaterialien, PhD Thesis, Technical University Berlin, Berlin, 2002.

124. T.G. Alkhazov, A.E. Lisovskii, M.G. Safarov, V.V. Lapin, N.A. Kurbanov, Kinet. Catal. 14 (1973) 1182–1188.
125. G. Emig, H. Hofmann, J. Catal. 84 (1983)15-26.
126. Y. Iwasawa, H. Nobe, J. Catal. 31 (1973) 444-449.
127. P.G. Menon, J. Mol. Catal. 59 (1990) 207-220.
128. J. Diao, Z. Feng, R. Huang, H. Liu, S.B.A. Hamid, D.S. Su, ChemSusChem 9 (2016) 1-6.
129. J. Xu, L.-C. Wang, Y.-M. Liu, Y. Cao, H.-Y. He, K.-N. Fan, Catal. Lett. 133 (2009) 307-313.
130. D.S. Su, N. Maksimova, G. Mestl, V.L. Kuznetsov, V. Keller, R. Schlögl, N. Keller, Carbon 45 (2007) 2145–2151.
131. C. Nederlof, V. Zarubina, I.V. Melián-Cabrera, E.H.J. Heeres, F. Kapteijn, M. Makkee, Appl. Catal. A: Gen. 476 (2014) 204-214.
132. N.R. Shiju, M. Anilkumar, S.P. Mirajkar, C.S. Gopinath, B.S. Rao, C.V. Satyanarayana, J. Catal. 230 (2005) 484–492.
133. B. Murugan, A.V. Ramaswamy, J. Am. Chem. Soc. 129 (2007) 3062-3063.
134. M.L. Woebkenberg, L.J. Doemeny, Am. Ind. Hyg. Assoc. J. 39 (1978) 598–599.
135. C.R. Adams, T.J. Jennings, J. Catal. 17 (1970) 157–177.
136. M. Bismillah Ansari, S.-E.Park, Energy Environ. Sci. 5 (2012) 9419-9437.
137. C.H. Barthlomew, Chem. Eng. 91 (19984) 96-112.
138. W. Wang, S. Wang, X. Ma, J. Gong, Chem. Soc. Rev. 40 (2011) 3703–3727.
139. U.S. Energy Information Administration, International Energy Outlook 2014 (http://www.eia.gov/forecasts/ieo/index.cfm).
140. V. Havran, M. Dudukovic, C.D. Lo, Ing. Eng. Chem. Res. 50 (2011) 7089-7100.
141. M. Mikkelsen, M. Jorgensen, F.C. Krebs, Energy Environ. Sci. 3 (2010) 43–81.
142. T. Sakakura, J.-C. Choi, H. Yasuda, Chem. Rev. 107 (2007) 2365–2387.
143. W. Leitner, Angew. Chem. Int. Ed., 34 (1995) 2207–2221.
144. A. Behr, G. Henze, Green Chem. 13 (2011) 25–39.
145. S.N. Riduan, Y. Zhang, Dalton Trans. 39 (2010) 3347–3357.
146. International Energy Outlook 2011, U.S. Energy Information Administration, September 2011, pp. 139.
147. The Carbon Dioxide Capture and Conversion (CO_2 CC) Program, The Catalyst Group Resources, May 2011, pp. 7.
148. G. Centi, S. Perathoner, Stud. Surf. Sci. Catal. 153 (2004) 1-8.
149. X. Xiaoding, J.A. Moulijn, Energy Fuels 10 (1996) 305-325.
150. G. Towler, S. Lynn, Chem. Eng. Sci. 49 (1994) 2585-2591.
151. C.S. Chen, W.H. Cheng, S.S. Lin, Appl. Catal. A: General 257 (2004) 97–106.
152. T. Bunluesin, R.J. Grote, G.W. Graham, Appl. Catal. B: Environ. 15 (1998) 107-114.
153. Y. Li, Q. Fu, M. Flytzani-Stephanopoulos, Appl. Catal. B: Environmental 27 (2000) 179-191.
154. C. Rhodes, G.J. Hutchings, A.M. Ward, Catal. Today 23 (1995) 43-58.
155. T. Shido, Y. Iwasawa, J. Catal. 141 (1993) 71-81.
156. G. Jakobs, L. Williams, U. Graham, D. Sparks, B.H. Davis, J. Phys. Chem. B 107 (2003) 10398-10404.
157. K. Azzam, I. Babich, K. Seshan, L. Lefferts, J. Catal. 251 (2007) 153– 162.
158. K. Azzam, I. Babich, K. Seshan, L. Lefferts, J. Catal. 251 (2007) 163– 171.
159. A. Goguet, F.C. Meunier, D. Tibiletti, J.P. Breen, R. Burch, J. Phys. Chem. B 108 (2004) 20240-20246.
160. A.A. Balandin, N.D. Zelinskii, G.M. Marukyan, O.K. Bogdanova, Zhurnal Prikl. Him. 14 (1941) 14.
161. N.D. Zelinskii, A.A. Balandin, G.M. Marukyan, USSR Auth. Certificate, 59055 (1941).
162. D.H. Olson, U.S. Patent 3, 406, 219 (1968)
163. N. Mimura, M. Saito, Catal. Today 55 (2000) 173-173.
164. A.Kh. Mamedov, S.R. Mirzabekova, Ind. Eng. Chem. Res. 34 (1995) 474-482.
165. N. Mimura, I. Takahara, M. Saito, T. Hattori, K. Ohkuma, M Ando, Catal. Today 45 (1998) 61-64.
166. A. Sun, Z. Qin, S. Chen, J. Wang, J. Mol. Catal. A: Chemical 210 (2004) 189-195.
167. Y. Joseph, M. Wühn, A. Niklewski, W. Ranke, W. Weiss, C. Wöll, R. Schlögl, Phys. Chem. Chem. Phys. 2 (2000) 5314-5319.
168. C. Nederlof, Catalytic dehydrogenations of ethylbenzene to styrene, Introduction into styrene production, p. 11-13, PhD Thesis, TU Delft, Delft, 2012.

169. J.-S. Chang, D.-Y. Hong, V.P. Vislovskiy, S.-E. Park, Catal. Surv. Asia 11 (2007) 59-69.
170. V.P. Vislovskiy, J.S. Chang, M.S. Park, S.-E. Park, Catal. Comun. 3 (2002) 227-231.
171. N. Mimura, M. Saito, Catal. Lett. 58 (1999) 59-62.
172. S. Sato, M. Ohhara, T.Sodesawa, F.Nozaki, Appl. Catal. 37 (1998) 207-2015.
173. Y. Qiao, C. Miao, Y. Yue, Z. Xie, W. Yang, W. Hua, Z. Gao, Micropor. Mesopor. Mat. 119 (2009) 150-157.
174. Y. Ohishi, T. Kawabata, T. Shishido, T. Takaki, Q. Zhang, Y. Wang, K. Tekehira, J. Mol. Catal. A: Chem. 230 (2005) 49-58.
175. C. Nederlof, G. Talay, F. Kapteijn, M. Makkee, Appl. Catal A: Gen. 423-424 (2012) 59-68.
176. I. Wang, W.F. Chang, R.J. Shiau, J.C. Wu, C.S. Chung, J. Catal. 83 (1983) 428-436.
177. I. Wang, J.-C. Wu, C.-S. Chung, Appl. Catal. 16 (1985) 89-101.
178. T. Tagawa, T. Hattori, Y. Murakami, J. Catal. 75 (1982) 66-77.
179. Z.H. Kafafi, R.H. Hauge, W.E. Billups, J.L. Margrave, Inorg. Chem. 23 (1984) 177–183.
180. J.A. Moulijn, M.B. Cerfontain, F. Kapteijn, Fuel 63 (1984) 1043–1047.
181. J.N. Park, J. Noh, J.S. Chang, S.E. Park, Catal. Lett. 65 (2000) 75-78.
182. D.R. Burri, K.M. Choi, D.-S. Han, J.-B. Koo, S.-E. Park, Catal. Today 115 (2006) 242-247.
183. D.R. Burri, K.M. Choi, S.C. Han, A. Burri, S.E. Park, J. Mol. Catal. A: Chem. 269 (2007) 58-63.
184. K.N. Rao, B.M. Reddy, S.-E. Park, Appl. Catal. B: Environ. 100 (2010) 472-480.
185. J.-S. Chang, S.-E. Park, M.S. Park, Chem. Lett. 26 (1997) 1123–1124.
186. O. Irun, S.-A. Sadosche, J. Lasobras, J. Soler, J. Herguido, M. Menendez, Catal. Today 203 (2013) 53-59.
187. R. Watanabe, Y. Saito, C. Fukuhar, J. Mol. Catal. A: Chem. 404-405 (2015) 57-64.
188. M. Boudart, Adv. Catal. 20 (1969) 153–166.
189. M. Che, C.O. Bennett, Adv. Catal. 36 (1989) 55-172.
190. R.A. van Santen, Accounts of Chemical Research (2009) 57-66.
191. S. Sharma, S. Hilaire, J.M. Vohs, R.J. Gorte, H.W. Jen, J. Catal 190 (2000) 199-204.
192. A. Bueno-Lopez, K. Krishna, M. Makkee, Appl. Catal. A: Gen. 342 (2008) 144-149.

2

CALCINATION EFFECTS ON CeZrO$_x$ GEOMETRY AND STYRENE PRODUCTION FROM ETHYLBENZENE

ABSTRACT

A series of CeZrO$_x$ catalysts were prepared by calcination of hydrothermally obtained metal oxide precipitate at increasing temperatures. The samples were characterized by HRSEM, XRD and Raman spectroscopy, showing a change in morphology and particle size as a function of calcination temperature. Catalytic testing for ethylbenzene dehydrogenation with CO_2 showed a decreasing activity per gram with increasing calcination temperature due to the increasing particle size. However, ethylbenzene dehydrogenation activity per m^2 also steadily decreased. Correlation of the catalytic results with Raman analysis showed that not only the number of oxygen vacancies decrease with increasing particle size due to a lower surface area, but also their specific reactivity decreased because of a change in the particle morphology.

Keywords: Ethylbenzene dehydrogenation; doped-ceria; morphology change

Published as: M. Kovacevic, R. Brunet Espinosa, L. Lefferts, B.L. Mojet, Appl. Catal. A: Gen. 469 (2014) 1-7

2.1 INTRODUCTION

Cerium oxide is a key compound for various applications, like gas sensors [1,2], solid oxide fuel cells [3,4,5], and solar cells [6,7]. Ceria based catalysts are useful for automobile exhaust treatments [8,9], CO oxidation [10,11], low temperature water-gas-shift reaction [12,13], and CO_2 activation [14].

Recently, cerium oxide was also reported being a promising catalyst for ethylbenzene dehydrogenation (EBDH) in the presence of oxygen [15] or N_2O [16]. EBDH for the production of styrene has attracted lots of attention lately, attempting to minimize energy consumption of the process [17,18]. The route to styrene using carbon dioxide as a soft oxidant, which can replace conventionally used steam, has been initially suggested back in 1990s by various research groups [19,20,21,22]. CO_2 addition requires less dilution compared to steam due to its high heat capacity. CO_2 is proposed to increase ethylbenzene equilibrium conversion due to the reverse water gas shift (RWGS) [23,24] reaction. Moreover, CO_2 has been suggested to turn the reaction pathway to an oxidative route enhancing the reaction rate [18,21]. In addition, CO_2 possibly prolongs catalyst life time by coke gasification via the reverse Boudart reaction. Bulk V/MgO catalyst, for instance, produces 2.5 times higher amount of styrene in the presence of CO_2 compared to Ar atmosphere [25]. Carbon supported vanadia based catalysts are reported as promising candidates for EBDH with CO_2, however strong deactivation due to coke deposition occurred [26]. Coke deposits on the other hand were reported as catalytically active for EBDH in the presence of CO_2 for alumina and zirconia catalysts [27].

The role of acid-base and redox properties together with the activity of surface/ lattice oxygen species in EBDH with CO_2 have been extensively reported by the group of Park for various catalytic systems [18]. An earlier comprehensive study suggested mixed ZrO_2 based oxides as highly suitable for EBDH with CO_2 [28]. An increasing catalytic activity from pure oxides to mixed oxides and finally mixed oxide supported on SBA-15 was also reported [29].

Pure ceria was reported to have an extraordinary oxygen storage capacity (OSC) which was proposed to explain the unique catalytic properties [30]. The OSC of ceria is related to the oxygen vacancy concentration that in turn depends on catalyst morphology, shape, crystallite size, and calcination history of the material [31]. The oxygen vacancy concentration of ceria can be enhanced by the addition of a modifier, such as lower valence metal cations [32]. Doping with iso-valent Zr^{4+} was also reported to increase oxygen deficiency and reducibility of ceria [33,34,35]. Further, it was reported that increasing calcination temperature induces defect annihilation in pure ceria [36], while for zirconia-ceria solid solutions ageing at 850°C hardly affect the oxygen storage capacity [32].

The aim of the present study is to explore the properties of cubic shaped zirconia doped ceria for EBDH with CO_2. Ceria cubes have specifically different surface planes (100) exposed than those of generally applied polycrystalline CeO_2 (111) [37,38] and have a high intrinsic oxygen defect stability. The effect of calcination temperature on the structure and defect concentration of a series of $CeZrO_x$ catalysts is investigated and related to the catalytic activity for EBDH with CO_2.

2.2 EXPERIMENTAL PART

2.2.1 Materials

Commercially available NaOH pellets (Merck, 99%), $Ce(NO_3)_3{\cdot}6H_2O$ (99.99% Aldrich) and monoclinic ZrO_2 (Magnesium Electron Ltd, MEL, BET surface area is 3 $m^2{\cdot}g^{-1}$) were used for catalyst synthesis.

2.2.2 Catalyst preparation

A series of $CeZrO_x$ catalysts were prepared following the hydrothermal synthesis procedure described elsewhere [39]. We used an autoclave of 125 mL volume keeping the rest of the experimental conditions identical to the procedure in the reference [39]. Initially cc. NaOH solution was prepared by diluting 110 g of NaOH in 170 mL of deionized water. In parallel, 1 g of $Ce(NO_3)_3{\cdot}6H_2O$ and 0.025 g of ZrO_2 was dispersed in 17mL of deionized water. Parts of these solutions were mixed keeping the Ce/ OH ratio the same as reported elsewhere [39] resulting in a 70 ml of thus prepared mixture which was afterwards stirred (250 rpm) for 10 min. Finally, 20 mL of deionized water was added to the resulting mixture, transferred to an autoclave and hydrothermally heated at 150°C for 19 h (static conditions). The obtained participate was centrifuged, and washed (until pH=7) several times with deionized water. Further, it was dried at 110°C overnight (static air), divided into four portions and calcined in flowing artificial air (5 h, 50 mL·min^{-1}). The series of $CeZrO_x$ catalysts (molar ratio Ce:Zr=92:8) are denoted as: $CeZrO_x$-580, $CeZrO_x$-625, $CeZrO_x$-730 and $CeZrO_x$-840 with the number indicating the respective calcination temperature. It should be noted that by this preparation procedure cubic shaped particles were obtained, contrary to the rod shaped particles described in the reference [39].

A reference pure ceria sample, CeO_2-625, was prepared following the same preparation route, but without addition of ZrO_2, and subsequently calcined at 625°C. Pure monoclinic ZrO_2 was calcined at 625°C prior to reaction as a second reference sample.

2.2.3 Catalyst characterization

Catalyst surface area (BET) was determined by N_2-adsorption at 77K (Micromeritics Tristar). The samples were out-gassed in vacuum at 200°C for 24 h prior to analysis.

Sample morphology was studied by Scanning Electron Microscopy (LEO 1550 FEG-HRSEM) equipped with an in-lens detector.

X-ray diffraction (XRD) patterns were recorded using a Bruker D2 powder diffractometer equipped with a position sensitive detector over a 2θ-range between 15° and 75° using Cu Kα radiation, λ=0.1544 nm. The average crystallite size was determined based on X-ray line broadening using Scherrer's equation.

Raman spectroscopy measurements were performed with a Senterra Bruker instrument, equipped with a cooled CCD detector. The spectra were recorded at λ_{ex}=532nm, 2s integration time, 20 co-additions, 10mW laser power and 9-15 cm^{-1} resolution. The quantification of species was performed on baseline corrected spectra normalized to the intensity of the peak at 464 cm^{-1} taking the tailing of the main peak into account.

Thermal gravimetric analysis (TG, Mettler Toledo), was conducted in flowing artificial air. Typically 10mg of sample was dried at 125°C for 30 min and cooled to room temperature. Subsequently, temperature increased to 800°C with 10 °C·min^{-1} ramp.

2.2.4 Catalytic testing

Catalytic tests were carried out at atmospheric pressure at 560°C in a fixed-bed quartz tubular reactor (4.0 mm i.d.). The amount of catalyst per run was tuned in such a way that ethylbenzene (EB) conversion reached 6±2% stable differential level after approximately 120 min time-on-stream (exact amounts of the catalysts are given in Appendix 2). Catalyts were diluted by appropriate amount of quartz/ inert keeping the total weight fixed to 60 mg in all cases. EB concentration in the gas phase was controlled at 1 mol% via the vapour pressure using a double saturator. In the first saturator EB was evaporated at 35°C, followed by condensation at 23°C in the second saturator. CO_2 was added as a soft oxidant and CO_2 to EB ratio was adjusted to 7 in a total flow of 30 ml·min^{-1} (balance N_2). Prior to reaction, catalysts were pretreated in pure N_2 at 580°C (30 min) and subsequently in CO_2 at the reaction temperature for 30 min. Carbon dioxide is known to interact with ceria quite strongly to form stable carbonates [40]. For this reason the catalysts were treated with CO_2 prior to exposure to ethylbenzene.

Reaction products were analyzed by on-line GC Varian-450 equipped with TCD and FID detector and four columns: Hayesep T, Hayesep Q, Molsieve 13X and CP-Wax. The experiments were reproducible with a typical overall error of ± 5 %.

Catalyst activity is expressed as the amount of EB or carbon dioxide converted per weight of catalyst or catalyst surface area. Selectivity to styrene (Sel.$_{Sty}$) is defined as the fraction of styrene to the total aromatics' content (eq. 2.1).

$$\text{Sel.}_{Sty}(\%)=[\text{Styrene}]/([\text{Styrene}]+[\text{Toluene}]+[\text{Benzene}])\cdot 100\% \qquad \text{(eq. 2.1)}$$

The carbon balance was calculated as the ratio of the sum of all aromatic compounds in product stream (styrene, toluene, benzene and non-reacted EB) *vs.* the amount of EB being fed to the reactor. CO_2 was not taken into account for the carbon balance because of its low conversion and thus extremely high contribution to the overall carbon-balance. The carbon balance based on aromatics varied between 98.2 and 99.5%.

2.3 RESULTS

2.3.1 Catalysts characterization

Fig. 2.1 shows the HRSEM images of the $CeZrO_x$ samples after calcination at different temperatures. The catalysts' morphology clearly changed with increasing calcination temperature as can be seen from the HRSEM images in Fig. 2.1a-d. After calcination at 580°C (Fig. 2.1a), the $CeZrO_x$ particles had a regular cubic shape. With increasing calcination temperature, the catalyst particles became more rounded and transformed into spherical shapes after calcination at 840°C. In addition, the $CeZrO_x$ particle size increased with increasing calcination temperature.

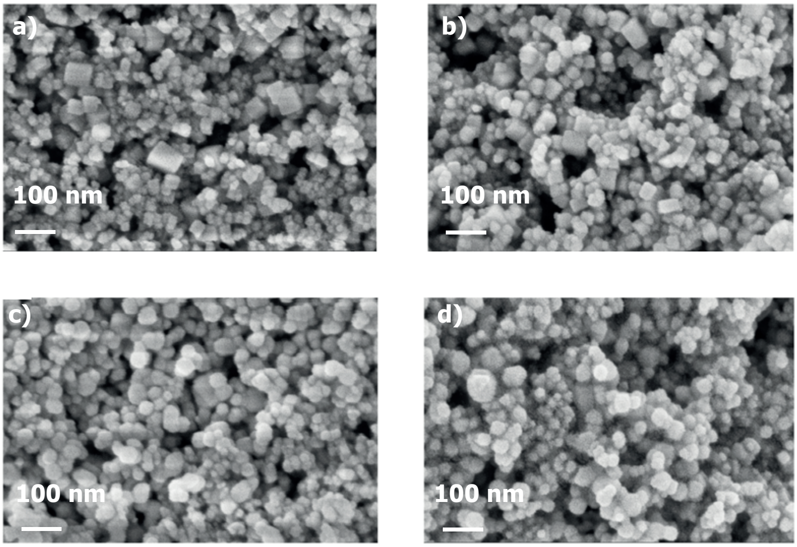

Figure 2.1. HRSEM images: CeZrO$_x$-580 (a), CeZrO$_x$-625 (b), CeZrO$_x$-730 (c), and CeZrO$_x$-840, (d) catalysts.

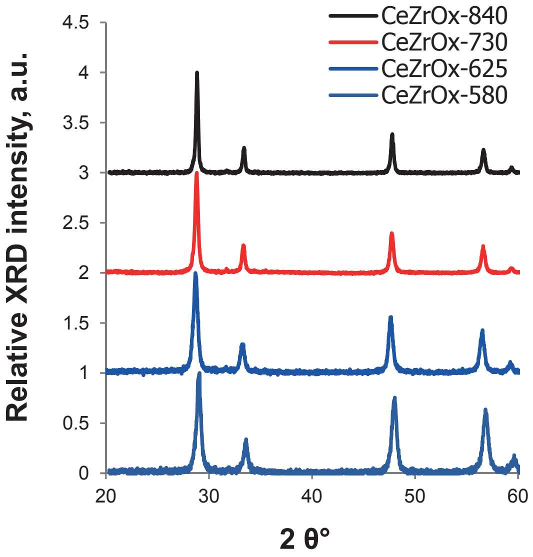

Figure 2.2. XRD patterns of CeZrO*x* catalysts calcined at 580-840°C.

Fig. 2.2 shows the X-ray diffraction (XRD) patterns of CeZrO$_x$ catalysts calcined at 580-840°C. For all investigated samples dominant Bragg diffractions were observed at 28.8°, 47.6°, and 56.7° 2θ, corresponding to respectively (111), (220) and (311) crystal planes of the fluorite fcc structure of CeO$_2$ [41]. Very weak Bragg diffractions at 31.2° and 34.2° correspond to monoclinic zirconia phase [42]. Table 2.1 summarizes the particle size as calculated from the peak widths in the XRD plots.

Table 2.1. Nitrogen physisorption and crystallite size (from XRD)

Catalyst	S_{BET}, m²/g	Crystallite size, nm
ZrO_2	3	n.d.
CeO_2-625	35	n.d.
$CeZrO_x$-580	36	24
$CeZrO_x$-625	34	25
$CeZrO_x$-730	32	32
$CeZrO_x$-840	28	41

Nitrogen physisorption showed a gradual decrease in BET surface area with increasing calcination temperature (Table 2.1).

Raman spectroscopy was used to further investigate the catalyst structure. Fig. 2.3a shows the normalized Raman spectrum of $CeZrO_x$-625 as a typical example for the studied samples together with the spectrum of pure CeO_2-625 and monoclinic ZrO_2 (not normalized). The ceria spectra are dominated by a strong peak at 464 cm^{-1} from the F_{2g} mode of the CeO_2 fluorite lattice [43]. Additionally, three weaker bands were identified, assigned to oxygen displacement (258 cm^{-1}), oxygen vacancies (600 cm^{-1}), and lattice oxygen (1170 cm^{-1}) [44]. For CeO_2-625 an additional band is observed around 900 cm^{-1}, which is absent in $CeZrO_x$-625. For $CeZrO_x$-625, the bands from monoclinic zirconia [45] are superimposed on the ceria peaks, suggesting only partial incorporation of zirconia in the ceria lattice.

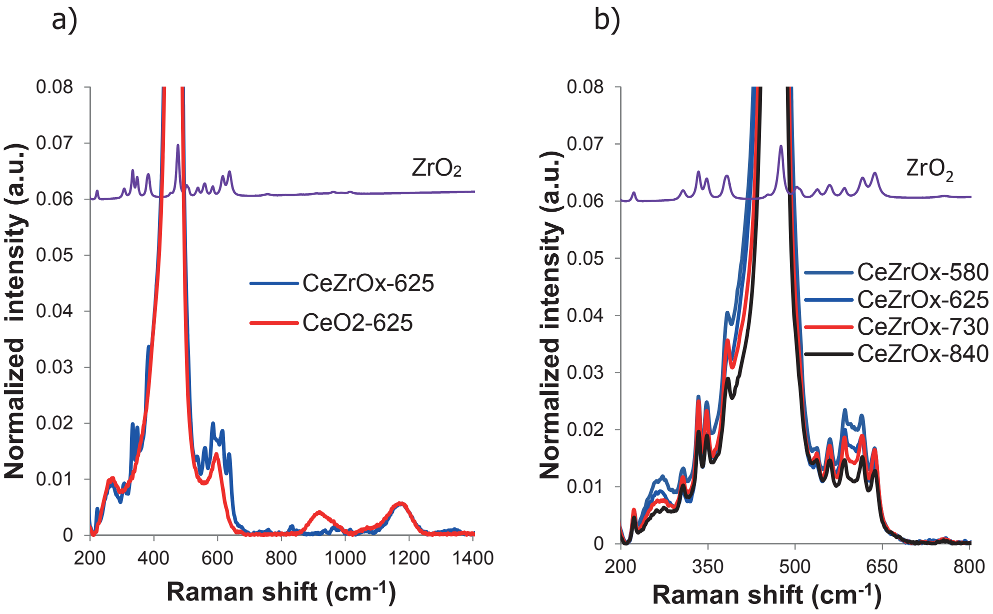

Figure 2.3 Typical Raman spectra of (a) $CeZrO_x$-625 (blue), CeO_2-625 (red) and monoclinic ZrO_2 (violet); (b) The effect of the calcination temperature on oxygen displacement (258 cm^{-1}), oxygen vacancy (600 cm^{-1}), and ceria F_{2g} (464 cm^{-1}) vibrations of $CeZrO_x$ catalysts.

Fig. 2.3b shows that upon increasing calcination temperature the width of the F_{2g} band (464 cm^{-1}) steadily decreases. Further, with increasing calcination temperature the peaks at 258 cm^{-1} and between 550 and 650 cm^{-1} clearly decreased.

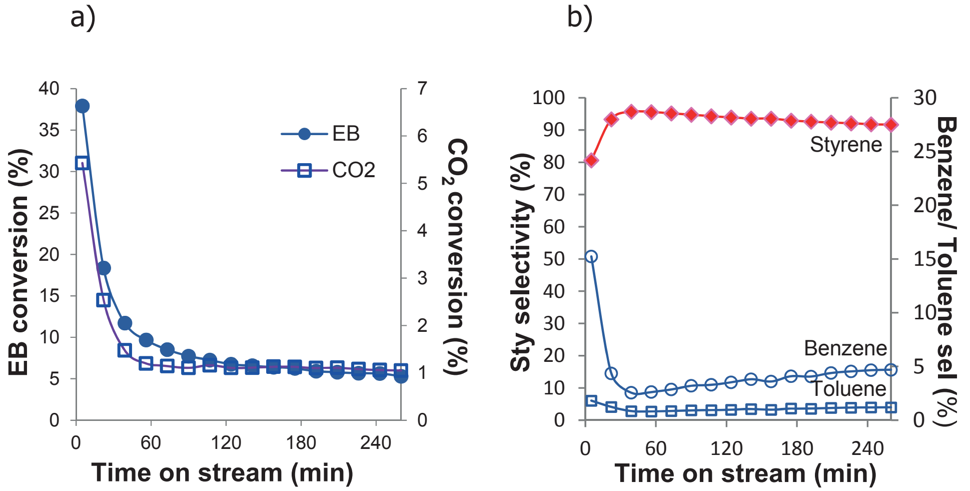

Figure 2.4. Testing results for CeZrO$_x$-625 in EBDH with CO$_2$ as a typical example for all catalysts. Reaction conditions: T=560°C, F= 30ml·min^{-1} CO$_2$:EB=7, m_{cat}=30 mg. (a) Conversion pattern for EB (filled cycles) and CO$_2$ (empty squares) and (b) corresponding aromatic product selectivity.

2.3.2 Catalytic testing

The CeZrO$_x$ catalysts were tested for ethylbenzene (EB) dehydrogenation with CO$_2$ as a soft oxidant aiming at differential conversion in semi-steady state after 240 minutes time on stream (TOS). Typical conversion profiles for EB and CO$_2$ and product selectivity are shown in Fig.2.4. Both EB and CO$_2$ conversion sharply declined in a similar manner during the initial 120 minutes (Fig. 2.4a and Fig. A2.1 in Appendix 2).

The catalysts show similar deactivation patterns for EB and CO$_2$ conversion. The main product of EB dehydrogenation with CO$_2$ was styrene. During deactivation the selectivity to styrene increased at the expense of the production of benzene and toluene. The selectivity to styrene slowly decreased after the initial increase. At the same time a small but steady increase of benzene production was observed to approximately 5% after 240 min TOS, at which point all catalysts exhibited about 92±2% selectivity towards styrene (Fig. 2.4b). Craking producst were formed only initially, in semi-steady state amount was below the detection limit in this study.

The aromatic carbon balance varied between 98.2-99.5%. TGA experiments on the spent catalysts confirmed that the missing amount of carbon can be attributed to catalyst coking. Typically, 2-3 wt.% of carbonaceous deposits were found on the spent catalysts.

In steady state, for all catalysts the ratio of [mol CO$_2$ converted/mol CO produced] equaled 1. Further, the detected amount of produced H$_2$ was about 40% of the observed amount of styrene.

Fig. 2.5 shows the conversion of CO_2 and EB at 240 min TOS per gram of catalyst (a and b) and per m^2 BET surface area (c and d). The conversions obtained with pure CeO_2-625 and monoclinic ZrO_2-625 are given as well. Comparing CeO_2-625 (dashed bar, red) with $CeZrO_x$-625 indicates a positive effect on the conversion due to the presence of zirconia in the sample. The conversion of EB over pure monoclinic ZrO_2-625 was approximately 5% of the conversion found for the $CeZrO_x$ samples, while CO_2 conversion was only 3% (based on the amount of ZrO_2 in the samples). Thus, the increase of conversion for $CeZrO_x$-625 is not only due to the possible presence of a ZrO_2 rich phase (monoclinic zirconia) in the sample. Moreover, monoclinic zirconia has been reported as not particular active for the reaction [46]. On the other side it has been reported that mixed oxides exhibit higher catalytic activity for EBDH with CO_2 compared to their constituent single oxides [28,29].

Increasing calcination temperature led to decreasing EB and CO_2 conversion per gram for the $CeZrO_x$ samples (Fig. 2.5a and b).

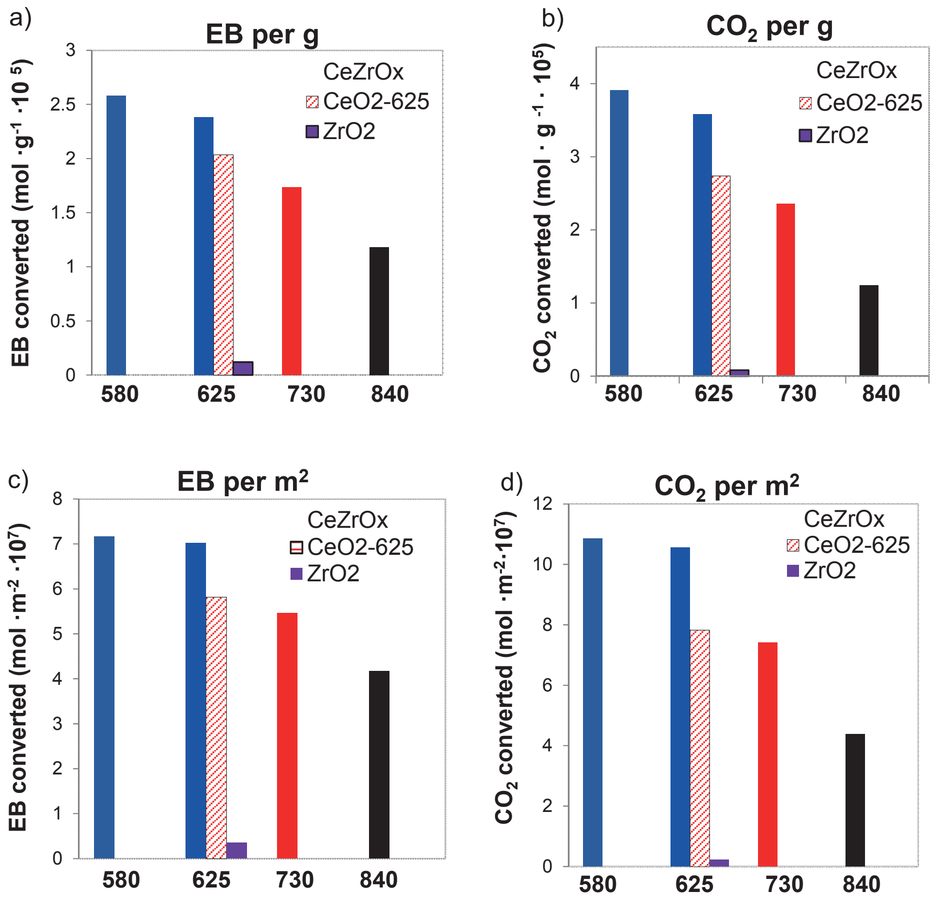

Figure 2.5. EB conversion per g (a) and m^2 (c) and CO_2 conversion per g (b) and m^2 (d) for the $CeZrO_x$ catalysts, pure CeO_2 and monoclinic ZrO_2. Reaction conditions: T= 560°C, F= 30ml·min^{-1} CO_2:EB= 7, m_{cat}= 27-49 mg at 240 min TOS.

Strikingly, when normalized per surface area, the activity per m^2 showed a clear decline with higher calcination temperature (Fig. 2.5 c and d), indicating that the decreasing activity per gram cannot solely be attributed to the decreasing surface area.

Based on the results in Figure 2.5 it should be noted that the catalyst of the highest activity exhibit the rate of $6{,}6 \cdot 10^{-7}$ $mol \cdot s^{-1} \cdot g^{-1}$ approaching the rates reported for cerium oxide catalysts in presence of O_2, i.e. $1{,}7 \cdot 10^{-6}$ $mol \cdot s^{-1} \cdot g^{-1}$

2.4 DISCUSSION

2.4.1 The effect of calcination temperature on ceria structure

The ex-situ characterization of the catalysts by HRSEM (Fig. 2.1), XRD (Fig. 2.2, Table 2.1) and BET (Table 2.1) confirms an increase of particle size and a decrease of surface area with increasing calcination temperature. In addition, the cubic geometry of the catalyst particles converts into a more spherical shape as was observed in the HRSEM pictures. Both XRD and Raman show the presence of small amounts of monoclinic ZrO_2 in the samples, but the amount could not be calculated because of the very low intensity in the XRD plots.

In the Raman spectra (Fig. 2.3) the F_{2g} band at 464 cm^{-1} was initially broad and asymmetric for $CeZrO_x$-580, but became narrower and more symmetric with increasing calcination temperature. In literature this peak narrowing has been attributed to annihilation of oxygen vacancies in the fluorite lattice [47], which was confirmed by the simultaneous decrease of the O-displacement band at 258 cm^{-1}. Because of the superposition of the zirconia bands on the oxygen vacancy band at 600 cm^{-1} it is not possible to uniquely assign the decreasing intensity to a decrease in oxygen vacancies, although this may be suggested based on the decrease of the O-displacement band 258 cm^{-1}.

Thermodynamic calculations predict that ceria shape alteration from cubic to spherical particles favours the exposure of (111) crystal planes at the catalysts surface reducing the number of crystal point defects [31]. The morphology transition of the catalysts with increasing calcination temperature as presented in Fig. 2.1, thus is expected to decrease the oxygen vacancies content. Indeed, the oxygen vacancy content clearly declines with increasing particle size as found with Raman spectroscopy (Fig. 2.3) which is in accordance with results reported by various research groups for small mono-size ceria particles (<10nm), thin ceria films and La^{3+}, Pr^{3+} doped ceria particles studied by Raman spectroscopy [47,48,49].

Fig. 2.6 shows the integrated intensity of the oxygen displacement band (258 cm^{-1}) in the Raman spectra as a function of BET surface area. The band at 258 cm^{-1} was taken as a measure for the concentration of vacancies since it was found that the formation of vacancies is associated with oxygen displacement in the lattice as a result of carbonate formation on the surface [50]. Clearly, the amount of oxygen displacement is linearly related to the BET surface area for the $CeZrO_x$ catalysts, consistent with the increase of particle size and shape change. In Fig. 2.6, the undoped CeO_2-625 sample deviates only slightly from the linear relation between the Zr-doped samples. This suggests that the addition of a low amount of zirconia (Ce:Zr = 92:8 molar ratio) only has a minor effect on the oxygen displacement and corresponding oxygen vacancy concentration after calcination at

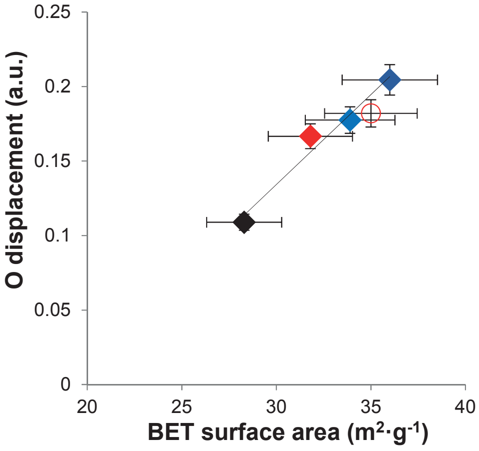

Figure 2.6. BET surface area *vs.* integrated intensity of the oxygen displacement band at 258 cm^{-1} in the Raman spectra of $CeZrO_x$ and CeO_2-625 catalysts (various colours denote $CeZrO_x$ catalysts calcined at increasing temperatures, empty symbol denotes CeO_2-625).

temperatures between 580 and 840°C. The results are consistent with literature reporting decreasing oxygen vacancy concentration for ceria upon calcination [36].

For solid solutions of zirconia and ceria with zirconia concentration up to 40 mol% a stabilizing effect was reported [32]. However, our samples have been prepared with much lower zirconia content, and Raman spectroscopy results (Fig. 2.3) indicated that not all zirconia was incorporated in the lattice, thus the stabilizing effect of zirconia can be considered minor for these samples.

2.4.2 The effect of calcination temperature on ethylbenzene dehydrogenation with CO_2

All catalysts showed a strong deactivation in the first hour of the experiment (Fig. 2.4a and Fig. A2.1 in Appendix 2). In the same period a clear increase in styrene selectivity was observed, while the amount of produced benzene decreased (Fig. 2.4b and Fig. A2.1 in Appendix 2). The strong deactivation of the catalysts could be due to the consumption of active lattice oxygen, which results in an over-oxidation of EB resulting in benzene in addition to styrene. Further, the presence of coke, as confirmed by TGA on the spent catalysts, is an additional possible explanation for the deactivation of the catalysts. The participation of lattice oxygen species in EB dehydrogenation has been reported by several research groups for vanadia and perovskite based catalysts [51,52,53]. To regenerate these sites an oxidant is added to the reactant, often steam or molecular oxygen. In the present study, CO_2 was added instead as a soft oxidant, however, the strong deactivation shows that CO_2 is not able to recover the active oxygen species at the speed of consumption.

The decreasing CO_2 conversion in the first hour (Fig. 2.4a) cannot be due to adsorption by ceria since the samples were first stabilized in CO_2. The deactivation pattern is identical to that of EB conversion, pointing to a relation between the reactions of these molecules. At all times, the ratio of [mol CO_2 converted/ mol CO produced] was close to 1, indicating a reduction of CO_2. In addition, the amount of H_2 detected was always lower than the amount of styrene produced. After deactivation, about 60% of H_2, based on styrene formation, was converted. The disappearance of hydrogen suggests additional pathways like CO_2 dissociation and subsequent production of water from H_2 and surface oxygen as has been proposed in literature [18,21]. Alternatively, H_2 could react with CO_2 as in the reverse water gas shift reaction, as has been proposed by others [23,24]. Unfortunately, we were not able to quantify the amounts of water produced. The exact details of the first stage of the reactions and the effect of CO_2 on the conversion of EB are, however, beyond the scope of this paper, and will be discussed in a paper currently in preparation [54].

Here we focus on the activity of the catalyst at steady-state, *i.e.* after the strong deactivation in the first hour. It should be noted that TOS still is relatively short compared to other studies in literature in which additional active sites due to coke formation were proposed [20]. After consumption of lattice oxygen, ethylbenzene could be converted via non-oxidative dehydrogenation as has been proposed before [33, 34].

In Fig. 2.5a and b, at first sight, the decreasing EB and CO_2 conversion per gram of catalyst with higher calcination temperature can be related to the decreasing surface area. However, Fig. 2.5c and d clearly show that the EB and CO_2 conversion per m^2 also decreased with increasing calcination temperature. Consequently, the explanation for the decreasing activity must be more complex than only a decrease in surface area. Similarly, the OSC capacity of polycrystalline ceria calcined at different temperatures was also found not to be directly related with BET surface area [16].

Reduced catalytic activity of the samples calcined at higher temperatures is in accordance with results reported for mesoporous ceria in oxidative EBDH [15]. The authors proposed that the superior catalytic performance of small ceria crystallites originated from their enhanced red-ox capacity. According to [55] mesostructured ceria exhibited higher surface area and enhanced redox capacity. The enhanced redox capacity will be determined by the number of defect sites as well as the reactivity of those sites, as was found for EB conversion in the presence of N_2O over reactive ceria [16]. The Raman spectra in Fig. 2.3 suggest that the higher catalytic activity for smaller $CeZrO_x$ particles could be related to an increasing number of oxygen deficient domains. Fig. 2.6 showed that the amount of displaced oxygen is linearly related to the BET surface area.

Fig. 2.7 shows the EB conversion per m^2 as a function of oxygen displacement integrated intensity as determined with Raman spectroscopy. Although the Raman experiments were performed *ex-situ* in air, the conditions for all samples were identical. This allows for comparison with the observed catalytic activity of the samples, although it is not a representation of the real number of oxygen vacancies at reaction conditions, which will be determined by the pre-treatment and reaction conditions. In-situ Raman experiments would be needed to further confirm this correlation.

The increasing activity per m^2 with increasing amount of oxygen vacancies in Fig. 2.7 points to an altered reactivity of the vacancies affecting the conversion rate of EB and

CO_2. The inclusion of the pure CeO_2-625 sample in the linear relation in Fig. 2.7 shows that the observed relationship also holds for samples without zirconia.

The observed relation can be explained by the shape change of the particles upon calcination (Fig. 2.1). The alteration from small cubic shaped to larger and more spherical particles increases the exposure of (111) surface planes. The (111) structure is known to have a lower oxygen vacancy stability than (100) planes in ceria cubes [37,50,56,57]. This observation is similar to a recent study reporting on the relation between the reactivity of lattice oxygen sites in perovskite catalysts with styrene formation rates from EB in the presence of steam [53]. In other words, not only the number of oxygen vacancies decreases with increasing particle size due to a lower surface area, but also their reactivity decreases because of the altered size and shape. This in turn affects the observed EB and CO_2 conversion rates. These results imply that the reducibility of ceria defined by both crystallite size and geometry influences the rate of EB dehydrogenation as well as the RWGS reaction. In a following paper the relation between these two reactions over ceria is further investigated [54].

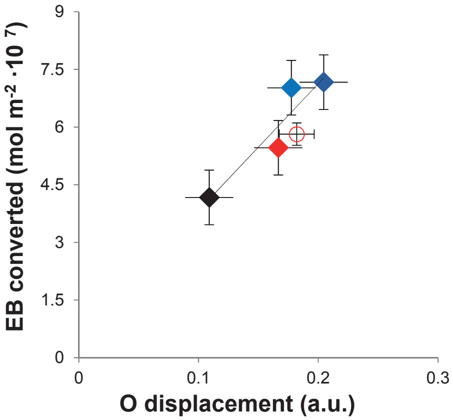

Figure 2.7. Catalyst activity vs. integrated intensity of the oxygen displacement band at 258 cm^{-1} in the Raman spectra of $CeZrO_x$ and CeO_2-625 catalysts (various colours denote $CeZrO_x$ catalysts calcined at increasing temperatures, empty symbol denotes CeO_2-625).

2.5 CONCLUSION

Calcination of $CeZrO_x$ at different temperatures, resulted in a series of catalysts with different morphology and particle size as observed with HRSEM and XRD. Raman spectroscopy revealed annihilation of oxygen vacancies, *i.e.* oxygen displacement sites with increasing calcination temperature. The activity expressed in mol·m^{-2} for ethylbenzene dehydrogenation to styrene in the presence of CO_2 depended not only on the amount but also on the specific reactivity of lattice defects sites, which was determined by the size and shape of the particles.

APPENDIX 2

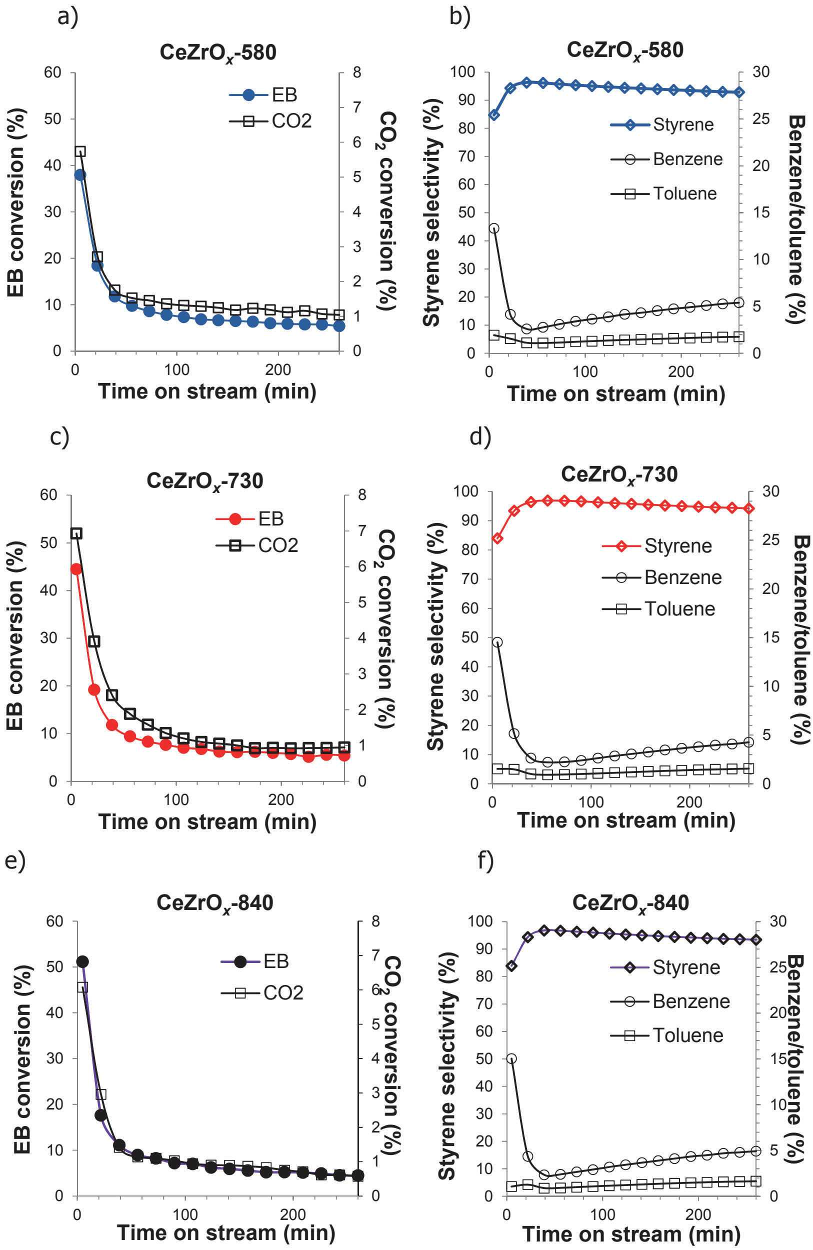

Figure A2.1. Testing results for $CeZrO_x$-580, $CeZrO_x$-730 and $CeZrO_x$-840 in EBDH with CO_2 Reaction conditions: T=560°C, F= 30ml·min^{-1} CO_2:EB=7, m_{cat}=27mg ($CeZrO_x$-580), m_{cat}=38,5mg ($CeZrO_x$-730), m_{cat}=49mg (CeZrOx-840). (a,c,e) Conversion patterns for EB (filled cycles) and CO_2 (empty squares) and (b,d,f) corresponding aromatic product selectivity for $CeZrO_x$-580, $CeZrO_x$-730 and $CeZrO_x$-840 respectively. EB conversion over quartz/ inert at the reaction condition was negligible.

BIBLIOGRAPHY

1. G. Eranna, B.C. Joshi, D.P. Runthala, R.P. Gupta, Crit. Rev. Solid State Mater. Sci. 29 (2004) 111-188.
2. N. Izu, W. Shin, N. Murayama, S. Kanzaki, Sens. Actuators B 87 (2002) 95-98.
3. J.-H. Wang, M. Liu, M.C. Lin, Solid State Ionics 177 (9-10) (2006) 939-947.
4. S.C. Singhal, MRS Bulletin 25(3) (2000) 16-21.
5. T. Kudo, H. Obayashi H, J. Electrochem. Soc. 122(1) (1975)142-147.
6. A. Corma, P. Atienzar, H. García, J.-Y.Chane-Ching, Nat. Mater. 3 (2004) 394-397.
7. A.Z. Turković, Z.C. Orel Solar En. Mater. Solar Cells 45 (1997) 275-281.
8. M. Luo, J. Chen, L. Chen, J. Lu, Z. Feng, C. Li, Chem. Mater. 13 (2001) 197-202.
9. T. Masui, Y. Peng, K. Machida, G. Adachi, Chem. Mater. 10 (1998) 4005-4009.
10. R.H. Nibbelke, M.A.J. Campman, J.H.B.J. Hoebink, G.B. Marin, J. Catal. 171 (1997) 358-373.
11. P. Ratnasamy, D. Srinivas, C.V.V. Satyanarayana, P. Manikandan, R.S. Senthil Kumaran, M. Sachin, V.N. Shetti, J. Catal. 221 (2004) 455-465.
12. N. Yi, R. Si, H. Saltsburg, M. Flytzani-Stephanopoulos, Energy Environ. Sci. 3 (2010) 831-837.
13. R. Si, M. Flytzani-Stephanopoulos, Angew. Chem. Int. Ed. 47 (2008) 2884-2887.
14. T. Staudt, Y. Lykhach, N. Tsud, T. Skála, K.C. Prince, V. Matolín, J. Libuda, J. Catal. 275 (2010) 181-185.
15. J. Xu, L.-C.Wang, Y.-M. Liu, Y. Cao, H.-Y. He, K.-N. Fan, Catal. Lett. 133 (2009) 307-313.
16. B. Murugan, A.V. Ramaswamy, J. Am. Chem. Soc. 129 (2007) 3062-3063.
17. F. Cavani, F. Trifiro, Appl. Catal. A Gen 133 (1995) 219-239.
18. M.B. Ansary, S.-E. Park, Energy Environ. Sci 5 (2012) 9419-9437.
19. M.-O. Sugino, H. Shimada, T. Turuda, H. Miura, N. Ikenaga, T.Suzuki, Appl. Catal. A Gen. 121 (1995) 125-137.
20. N. Mimura, I. Takahara, M. Saito, T. Hattori, K. Ohkuma, M. Ando, Catal. Today 45 (1998) 61-64.
21. J.-S. Chang, S.-E. Park. M.S. Park, Chem. Lett. 26 (1997) 1123-1124.
22. T. Badstube, H. Papp, P. Kustrowski, R. Dziembaj, Catal. Lett. 55 (1998) 169-172.
23. A.L. Sun, Z.F. Qin, J.G. Wang, Appl. Catal. A Gen 234 (2002) 179-189.
24. Y. Sakurai, T. Suzaki, N. Ikenaga, T. Suzuki, Appl. Catal. A Gen. 192 (2000) 281-288.
25. Y. Sakurai, T. Suzaki, K. Nakagawa, N. Ikenaga, H. Aota, T. Suzuki, J. Catal. 209 (2002) 16-24.
26. N. Ikenaga, T. Tsuruda, K. Senma, T. Yamaguchi, Y. Sakurai, T. Suzuki, Ind. Eng. Chem. Res. 39 (2000) 1228-1234.
27. C. Nederlof, F. Kapteijn, M. Makkee, Appl. Catal. A Gen 417-418 (2012) 163-173.
28. B.M. Reddy, D.-S. Han, N. Jiang, S.-E. Park, Catal. Surv. Asia 12 (2008) 56–69.
29. D. R. Burri, K.-M. Choi, J.-H. Lee, D.-S. Han, S.-E. Park, Catal. Commun. 8 (2007) 43–48.
30. A. Trovarelli (Ed.), Catalysis by Ceria and Related Materials, Imperial College Press, London, 2002, pp. 1-528.
31. J.A. van Bokhoven, ChemCatChem 1 (2009) 363-364.
32. E. Mamontov, T. Egami, R. Brezny, M. Koranne, S. Tyagi, J. Phys. Chem. B 104 (2000) 11110-11116.
33. G. Balducci, M.S. Islam, J. Kaspar, P. Fornasiero, M. Graziani, M. Saiful, J.D. Gale, J. Phys. Chem. B 101 (1997) 1750-1753.
34. G. Balducci, J. Kaspar, P. Fornasiero, M. Graziani, M. Saiful Islam, Julian D. Gale, J. Phys. Chem. B 101 (1997) 1750-1753.
35. G. Balducci, P. Fornasiero, R. Di Monte, J. Kaspar, S. Meriani, M. Graziani, Catal.Lett. 33 (1995) 193-200.
36. R. Si, Y.W. Zhang, S.J. Li, B.X. Lin, C.H. Yan, J. Phys. Chem. B 108 (2004) 12481-12488.
37. M. Baudin, M. Wojcik, K. Hermansson, Surf. Sci. 468 (2000) 51-61.
38. K. Zhou, X. Wang, X. Sun, Q. Peng, Y. Li, J.Catal. 229 (2005) 206-212.
39. Y.-C. Chen, K.-B.Chen, C.-S.Lee, M.C.Lin, J.Phys.Chem.C 113 (2009) 5031-5034.
40. G.N. Vayssilov, M. Mihaylov, P.S. Petkov, K.I. Hadjiivanov, K.M. Neyman, J. Phys. Chem. C 115 (2011) 23435-23454.
41. S. Meriani, G. Spinolo, Powder Diffraction 2(4) (1987) 255-256.

42. B.M. Reddy, P. Lakshmanan, A. Khan, C. López-Cartes,T.C. Rojas, A. Fernández, J. Phys. Chem. B 109 (2005) 1781-1787.
43. J.E. Spanier, R.D. Robinson, F. Zhang, S.-W. Chan, I.P. Herman, Phys. Rev. B 64 (2001) 245407.
44. Z. Wu, M. Li, J. Howe, H.M. Meyer III, S.H. Overbury, Langmuir 26 (2010) 16595-16606.
45. J.-M. Costantinia, A. Kahn-Harari, F. Beuneu, F. Couvreur, J. Appl. Physics 99 (2006) 123501.
46. J.-N. Park, J. Noh, J.-S. Chang, S.-E. Park, Catal. Lett. 65 (2000) 75-78.
47. F. Zhang, S.-W. Chan, J.E. Spanier, E. Apak, Q. Jin, R.D. Robinson, I.P. Herman, Appl. Phys. Lett. 80 (2002) 127-129.
48. J.L.M. Rupp, B. Scherrer, L.J. Gauckler, Phys. Chem. Chem. Phys. 12 (2010) 11114-11124.
49. S. Patil, S. Seal, Y. Guo, A. Schulte, J. Norwood, Appl. Phys. Lett. 88 (2006) 243110-243113.
50. M. Nolan, G.W. Watson, J. Phys. Chem. B 110 (2006) 16600-16606.
51. K. Saito, K. Okuda, N.O. Ikenaga, T. Miyake, T.Suzuki, J. Phys. Chem. A 114 (11) (2010) 3845-3854.
52. D.-Y. Hong, V.P. Vislovskiy, S.-E. Park, M.-S. Park, J.S. Yoo, J.-S. Chang, Bull. Korean Chem. Soc. 26 (2005) 1743-1748.
53. R. Watanabe, Y. Sekine, J. Kojima, M. Matsukata, E. Kikuchi, Appl. Catal. A Gen. 398 (2011) 66-72.
54. M. Kovacevic, S. Agarwal, B.L. Mojet, J.G. van Ommen, L. Lefferts, Appl. Catal. A Gen. 505 (2015) 354-364.
55. F. Giordano, A. Trovarelli, C. De Leitenburg, M. Giona, J. Catal. 193 (2000) 273-282.
56. E. Aneggi, J. Llorca, M. Boaro, A. Trovarelli, J. Catal. 234 (2005) 88-95.
57. T.X.T. Sayle, S.C. Parker, C.R.A. Catlow, Surf. Sci. 316 (1994) 329-336.

3

THE EFFECTS OF MORPHOLOGY OF CERIUM OXIDE CATALYSTS FOR DEHYDROGENATION OF ETHYLBENZENE TO STYRENE

ABSTRACT

Ethylbenzene (EB) dehydrogenation in presence and absence of CO_2 was investigated over CeO_2 catalysts of distinct morphologies: cubes, rods and particles. The presence of CO_2 resulted in prolonged catalyst activity and higher initial benzene selectivity compared to the absence of CO_2. However, CO_2 had no effect on the catalytic activity of ceria catalysts after stabilization. CeO_2 cubes exhibited about two times higher activity per m^2 compared to rods and particles, independent of presence or absence of CO_2. Product distribution and Raman spectroscopy characterization of the spent catalysts suggested that superior catalytic activity of CeO_2 cubes originates from the enhanced amount of lattice oxygen species that can be extracted by EB on the (100) crystal planes of ceria cubes, contrary to highly intrinsically stable (111) crystal planes predominantly exposed on rods and particles. We suggest that these O species are consumed in nonselective EB conversion pathways, generating partly-reduced surface sites, which are suggested to act as active sites for selective styrene formation.

Keywords: Ethylbenzene dehydrogenation; ceria; CO_2; cubes; rods; particles

Published as: M. Kovacevic, S. Agarwal, B.L. Mojet, J.G. van Ommen, L. Lefferts, Appl. Catal. A: Gen. 505 (2015) 354-364.

3.1 INTRODUCTION

Styrene molecule (Sty) is a main building block for various polymers: polystyrene, styrene-butadiene rubber, styrene-acrylonitrile and acrylonitrile-butadiene-styrene [1]. It is commercially produced by the dehydrogenation of ethylbenzene (EB) in presence of excess steam acting as: heat supplier, diluent, and coke gasifier. The use of steam is highly energy consuming, and several alternatives to steam have been studied [2]. CO_2 is considered as a promising soft oxidant that could replace steam in the EB dehydrogenation (EBDH) [3,4, 5,6]. CO_2 addition requires less dilution compared to steam due to its high heat capacity. Thermodynamic coupling with reverse water gas shift (RWGS) reaction is proposed to increase the Sty yield at equilibrium [7]. Moreover, CO_2 shows considerable activity for coke gasification [8] and limited catalyst deactivation with CO_2 has been also suggested.

EBDH in presence of CO_2 has been proposed to proceed via Mars Van Krevelen mechanism initially for vanadia based catalysts and later also for other oxide catalysts [9]. The participation of lattice oxygen species in EB dehydrogenation in presence and absence of CO_2 was experimentally demonstrated by transient studies on Cr, V, Fe oxides supported on activated carbon (AC), MgO, alumina and powdered diamond [10]. CO_2 is proposed to dissociate at oxygen vacant sites to form CO and active O, filling the oxygen vacancy and providing active oxygen for the dehydrogenation reaction [3,9,10]. The relation between the amount of extracted oxygen species on Sb promoted V_2O_5 supported on alumina and its catalytic activity in EBDH in presence of CO_2 has been demonstrated using transient experimental studies [11].

There is ample evidence in literature that ceria acts via Mars Van Krevelen mechanism [12] in oxidative dehydrogenation reactions. EBDH has been studied on cerium oxide nanocrystals in the presence of oxidants such as oxygen [13] and N_2O [14]. Supported ceria particles on SBA-15 were reported as a catalysts of prominent activity in EBDH with CO_2 [15].

Ceria gained particular attention as a catalyst with unique redox properties and high oxygen storage capacity (OSC), *i.e.* the ability to reversibly store and release oxygen while switching between Ce^{4+} and Ce^{3+} in a stable fluorite lattice [16]. Distinct ceria morphologies are known to stabilize specific crystal plane orientations. Recent work in our group reported that relative inactive (111) crystal planes are predominantly exposed at the surface of ceria rods in accordance with other reports [17], while highly reactive (110) crystal planes are stabilized at the surface of ceria cubes [18]. Theoretical studies have shown that the formation of oxygen vacancies on (110) and (100) crystal planes of CeO_2 is more favourable compared to (111) planes [19,20]. Therefore, catalytic activity can be accomplished [21] by manipulating the ceria morphology and hence the preferential exposure of the desired crystal planes as intrinsic redox chemistry on CeO_2 surface depends on exposure of specific planes. Many research groups took this advantage to manufacture materials with tailored catalytic properties [22,23,24]. Ceria rods for instance were emphasised as a morphology promising for CO oxidation [24], and 1,2 dichlorethane and ethyl acetate oxidation [25], while ceria nano spheres showed better performances than ceria rods for NO reduction [26]. Prominent activity of ceria cubes compared to rods and particles for WGS reaction has been recently reported by our group [18].

Ceria cubes are known to possess enhanced OSC [27,28]. In our previous study we reported that $CeZrO_x$ cubes exhibited prominent activity compared to the catalysts of spherical geometry in EBDH [29]. This was ascribed to altered reactivity of oxygen vacancies when morphology was changed from cubic to octahedral (spherical). The aim of this study is to further address the effect of morphology using pure ceria catalysts, comparing rods with cubes and particles in EBDH, as well as to address the effect of CO_2 addition.

3.2 EXPERIMENTAL

3.2.1 Materials

Commercially available NaOH pellets (Merck, 99%), $Ce(NO_3)_3{\cdot}6H_2O$ (99.99% Aldrich) and $Ce(OH)_4$ (Merck, 99%) were used for catalyst synthesis.

3.2.2 Catalyst preparation

Cerium oxide rods and cubes were prepared modifying the synthesis procedure reported elsewhere [17,30]. In the preparation of ceria rods 1.75g of $Ce(NO_3)_3{\cdot}6H_2O$ was first dissolved in 11 ml of distilled water. The mixture was rapidly added to 10 mass% NaOH aq solution. Ceria cubes have been prepared performing the mixing *vice versa* [30]. The resulting mixtures were stirred for 10 min (250 rpm), transferred into an autoclave (125 ml) and kept for 18 h in an oven at 130°C. Thus obtained precipitates were centrifuged at room temperature, rinsed with distilled water until pH=7 was obtained and dried overnight at 110°C. Calcination was finally performed in flowing synthetic air at 650°C for 5 h. Irregularly shaped ceria catalyst was obtained by calcining commercial $Ce(OH)_4$ powder under identical conditions.

3.2.3 Catalyst characterization

Catalysts surface area (BET) was determined by N_2-adsorption isotherm obtained at 77K (Micromeritics Tristar). The samples were outgassed in vacuum at 200°C for 24h prior to analysis.

Catalyst morphology was studied by Scanning Electron Microscopy, (SEM) LEO 1550 FEG-SEM equipped with in-lens detector. Transmission electronic microscopy (TEM) images were obtained on a Philips CM300ST-FEG electron microscope operated at an acceleration voltage of 300kV. Samples for TEM measurements were ultrasonically dispersed in ethanol and subsequently droplets of the suspension were deposited on a copper grid coated with carbon.

X-ray diffraction (XRD) patterns were recorded using PANalytical X´pert-APD powder diffractometer equipped with a position sensitive detector analyses over the 2θ-range between 25° and 65° using Cu Kα radiation, $\lambda=0.1544$ nm.

Raman spectroscopy measurements were performed with a Senterra Bruker instrument, equipped with a cooled CCD detector. The spectra of the fresh ceria catalysts were recorded at $\lambda=532$nm, with 2s integration time and 20 co-additions, 10mW laser power and at a resolution of 9-15 cm^{-1}. Spent catalysts (after 5 h time on stream) were studied with lower laser power of 2mW and longer (10s) integration time to prevent damage of the carbonaceous deposits.

Thermal gravimetric analysis (TG, Mettler Toledo) was performed in flowing air. Typically 10mg of the sample was pretreated at 125°C for 30 min prior to gradual temperature increase from room temperature till 800°C with the temperature ramp 10 °C·min^{-1}.

3.2.4 Catalytic testing

Catalytic tests were performed at atmospheric pressure and isothermal conditions (560˚C) in a fixed-bed quartz tubular reactor (4.0 mm i.d.). The amount of catalyst per run was tuned in such a way that Ethylbenzene (EB) conversion reaches 8±2% stable differential level after approximately 150 min time-on-stream (Table A3.1, Appendix 3). EB concentration in the feed was 1 mol%, controlled via the vapor pressure using a double saturator. In the first saturator EB was evaporated at 35°C, followed by condensation at 23°C in the second saturator. The tests were carried out with and without CO_2 keeping the total flow at 30 ml·min^{-1} (balance N_2). When CO_2 was added, a CO_2 to EB ratio was maintained at 7. Prior to the catalytic experiment, catalysts were pretreated in pure N_2 (580°C during 30 min, followed by 560°C during 30 min) in case of experiments without CO_2 addition. Experiments with CO_2 were preceded with a treatment in pure N_2 (580°C during 30 min) and subsequently in pure CO_2 (560°C during 30 min).

Reaction products were analyzed by on-line GC Varian-450 equipped with TCD and FID detector and four columns: Hayesep T, Hayesep Q, Molsieve 13X and CP-Wax. The experiments were reproducible with a typical overall error in the carbon mass balance smaller than 5%.

EB conversion was calculated as the fraction of EB converted *vs*. amount of EB fed. Selectivity to styrene ($Sel._{Sty}$) is defined as the fraction of styrene in the total amount of aromatic products (eq. 3.1.1). In the same manner selectivity to benzene and toluene were calculated.

$$\text{Sel.Sty}\ (\%)=[\text{Styrene}]/([\text{Styrene}]+[\text{Toluene}]+[\text{Benzene}])\cdot 100\% \qquad \text{(eq. 3.1.1)}$$

Equilibrium compositions of the reaction mixture in case of simple dehydrogenation was calculated using equation 3.1.2. In case of CO_2 addition the reversed-water-gas-shift (RWGS) equilibrium was accounted for using equation 3.1.3. Water has not been quantified in this study; it has been calculated from the mole balances as the concentration of styrene minus the concentration of hydrogen as suggested by others [31].

$$K_{SD}=[EB]\cdot[H_2]/[Sty] \qquad \text{(eq. 3.1.2)}$$

$$K_{RWGS} = [CO]\cdot[Sty\text{-}H_2]/([H_2]\cdot[CO_2] \qquad \text{(eq. 3.1.3)}$$

Equilibrium constants were obtained using HSC chemistry 4.0 software: at 560°C for RWGS: K_{RWGS}=0,301 (inverse reaction is WGS: K_{WGS}=3,318) and for the simple dehydrogenation K_{SD}=0,08723.

3.3 RESULTS

3.3.1 Characterization of fresh catalysts

Figure 1 shows the TEM images of ceria catalysts obtained using the three preparation routes, resulting in rods (Figure 3.1a), cubes (Figure 3.1b), and particles (Figure 3.1c). Ceria rods showed the most open stacked structure (Figure A3.1a), followed by ceria cubes (Figure A3.1b) and finally ceria particles that are more densely agglomerated, without any distinct structure (Figure A3.1c).

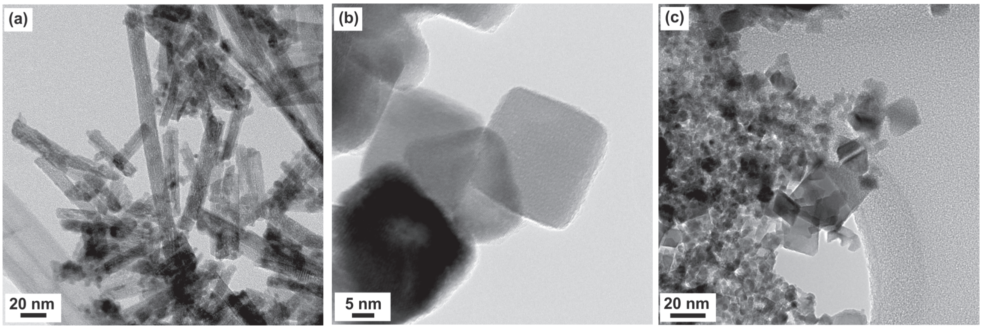

Figure 3.1. TEM images of ceria rods (a), cubes (b) and particles (c).

BET surface areas, as determined by nitrogen physisorption (Table 3.1), decreased in the order: rods > cubes > particles.

Pore size distribution indicated that all samples possess a very small fraction of micro pores (Figure A3.2). Predominantly, all three catalysts are characterized with the presence of meso pores. Particles have broad pore size distribution ranging from 3 to 30 nm (with a maximum at 4 nm). Average pore size for cubes is 18nm. Pore size distribution of rods exhibited a complex pattern with four local maxima. Cumulative pore volume increased in the following order: particles < cubes < rods consistent with the BET surface area increase (Table 3.1, Figure A3.3).

Catalysts structure was further investigated by X-ray diffraction (XRD) (Figure A3.4). Dominant Bragg diffractions were observed at 28.8°, 47.6° and 56.7° 2θ, corresponding to respectively to (111), (220), and (311) crystal planes of the fluorite fcc structure of CeO_2 [32].

Table 3.1. Nitrogen physisorption results

Ceria morphology	BET surface area (m^2/g)	Average pore diameter (nm)	Cumulative pore volume (cm^3/g)
Rods	73	27	251
Cubes	37	18	116
Particles	24	4	43

*After catalytic experiments, the surface area was identical to the area before use.

3.3.2 Catalytic testing

The ceria samples were tested for ethylbenzene (EB) dehydrogenation with CO_2 as a soft oxidant, aiming at differential conversion after initial deactivation. EB conversion with and without CO_2 is shown in Figures 3.2 a-c for respectively cubes, rods and particles. EB conversion without CO_2 rapidly decreased during the initial 40 min time-on-stream (TOS) (Figures 3.2 a-c) for all samples. The presence of CO_2 significantly slowed down the deactivation to a period of about 250 min TOS. This positive effect of CO_2 on EB conversion is most pronounced for ceria cubes (Figure 3.2a). After approximately 250 min TOS, CO_2 has no longer any significant effect on the EB conversion. Further for all samples, pre-treatment with CO_2 resulted in a significantly lower initial EB conversion level.

Conversion of CO_2 as shown in Figures 3.2d-f follows a similar pattern as conversion of EB. Initial CO_2 conversion is about 10%, decreasing to about 2% for all the catalysts with TOS.

Styrene selectivity with and without CO_2 is shown in Figure 3.3a-c. The initial selectivity to styrene was about 80%, independent of the presence of as well as pretreatment with CO_2, and increased to approximately 98% with TOS for all experiments. Remarkably, this increase was retarded by the presence of CO_2 for cubes and rods, whereas no effect of CO_2 was observed for particles. Even more remarkable is the fact that, despite the very similar initial selectivity, the product distribution (Figure 3.3) was strongly influenced by the presence of

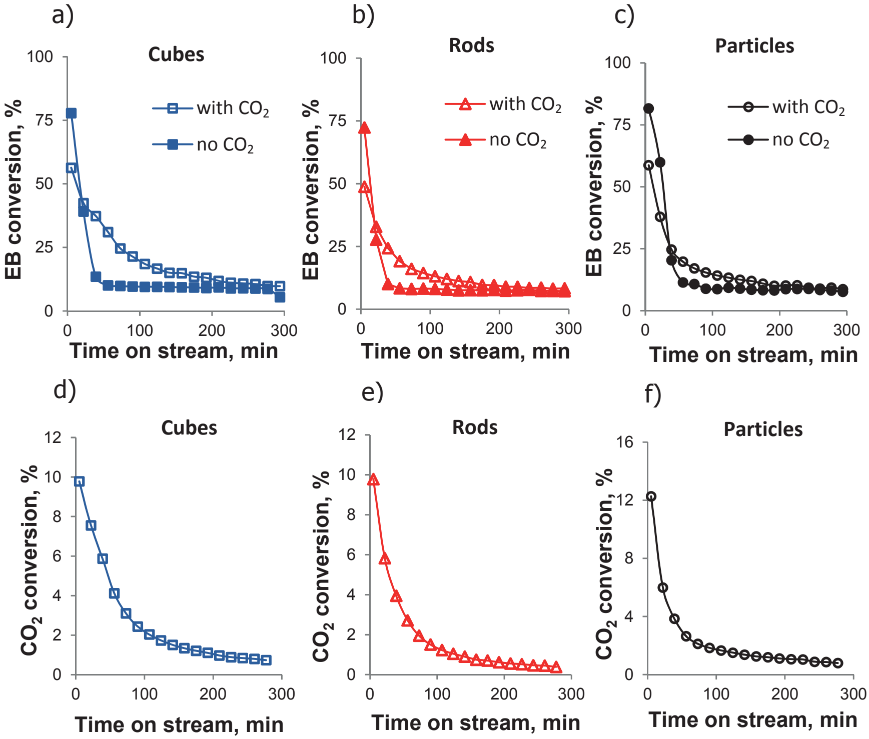

Figure 3.2. EB conversion for ceria cubes (a), rods (b), and particles (c). CO_2 conversion for ceria cubes (d), rods (e), and particles (f).

CO_2. The main initial by-product with CO_2 was benzene (Figures 3.3 d-f), whereas initially more toluene was formed in the absence of CO_2 (Figures 3.3 g-i). Cracking products were below the detection limit in semi steady-state.

Figure 3.4 shows the amounts of hydrogen and CO detected in the presence and absence of CO_2. Without CO_2, the production of H_2 followed the EB conversion pattern, while CO was detected only during initial 40 min time on stream for all investigated samples (Figure 3.4a-c). In the presence of CO_2, H_2 was detected in minor amounts after 30 minutes

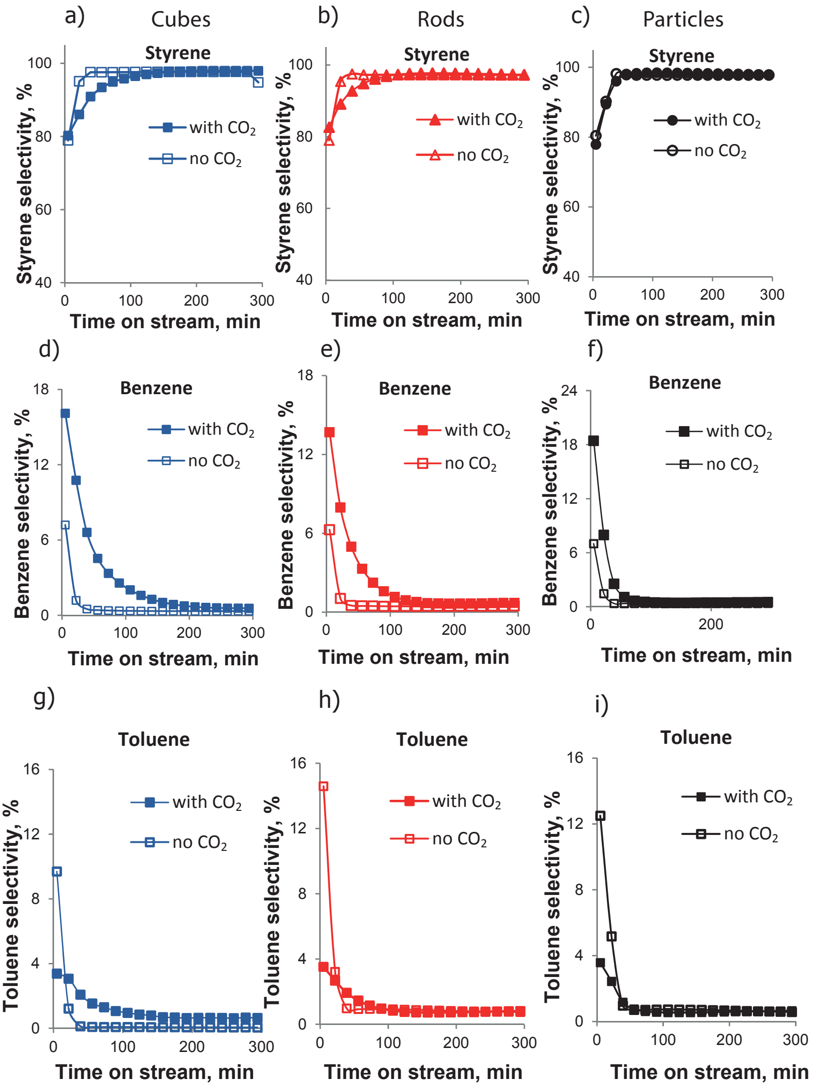

Figure 3.3. The first column: selectivity to styrene (a), benzene (d) and toluene (g) for ceria cubes (blue). Second column: the selectivity to styrene (b), benzene (e) and toluene (h) for ceria rods (red) and the third column: selectivity to styrene (c), benzene (f) and toluene (i) for ceria particles (black).

while at any time CO was found in significant quantities. The amount of CO produced when EB dehydrogenation was carried out in presence of CO_2 (empty symbols Figure 3.4 d-f) is

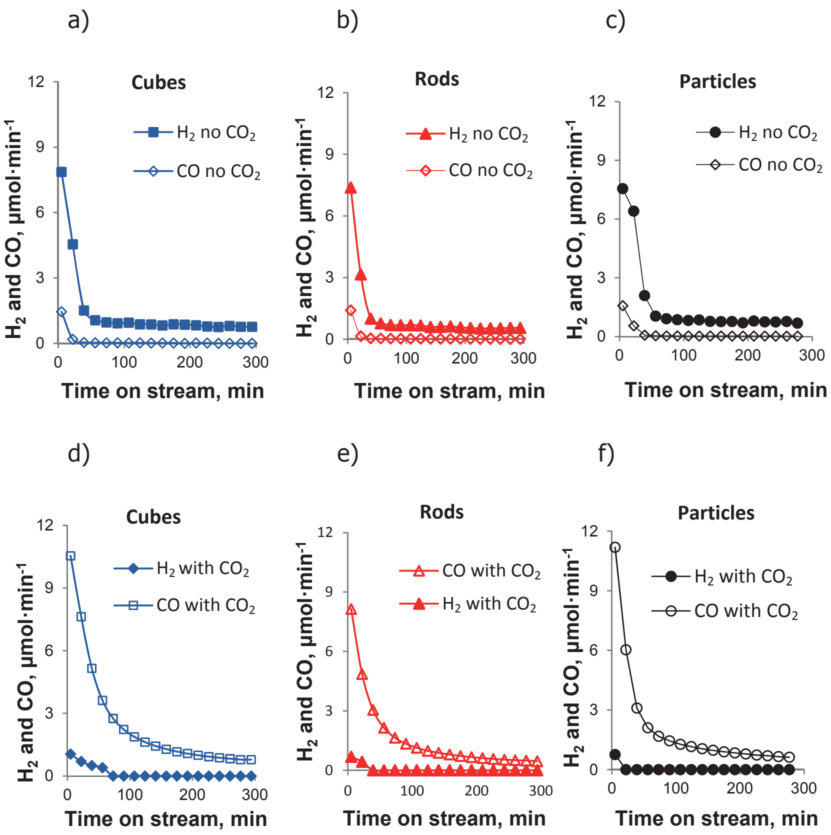

Figure 3.4. The amount of H_2 and CO produced without CO_2 on ceria cubes (a), rods (b), and particles (c). The amount of H_2 and CO produced with CO_2 on ceria cubes (d), rods (e), and particles (f).

higher than the amount of hydrogen generated via dehydrogenation in absence of CO_2 (filled symbols Figures 3.4 a-c).

3.3.3 Characterization of spent ceria catalysts

The amount of coke accumulated on the catalyst surface after 5 h TOS in EB dehydrogenation with and without CO_2 was determined by thermal gravimetric analysis (TGA, Figure 3.5). The amount of coke deposits per g of catalyst increased in the following order: particles < cubes < rods. The amount of coke was about 15% higher after experiments with CO_2, for cubes and rods. For particles the amount of coke was 43% higher after the experiment in CO_2. The amount of coke per m^2 surface area turned out to be very similar for cubes and rods, and was about 25% lower for ceria particles, as shown in Figure 3.5b.

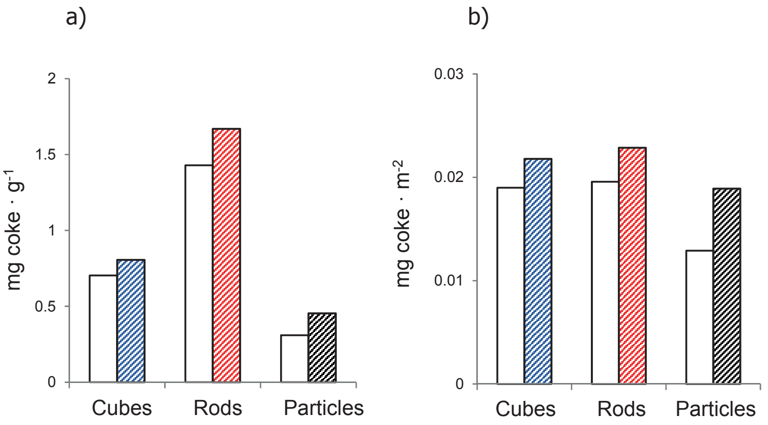

Figure 3.5. The amount of coke (white bars in absence of CO_2, patterned bars in presence of CO_2) after 5h time-on-stream normalized per catalysts weight per g (a) and m^2 (b).

The spent catalysts were further characterized by Raman spectroscopy. In Figure 3.6 a-c Raman spectra of fresh catalysts are compared with spectra of the catalysts spent in EBDH in presence and absence of CO_2.

Spectra of fresh catalysts (full black lines) are dominated by a strong peak at 464 cm^{-1} from the F_{2g} mode of the CeO_2 indicating fluorite lattice structure in agreement with XRD results [33]. Spectra of the spent catalysts are dominated with intense bands at 1335 and 1552 cm^{-1} indicating disordered and graphitic structure of the deposited carbonaceous species, respectively [34].

Figure 3.6d and e provide a magnification of the main peak at 464 cm^{-1} in the spectra presented in Figures 3.6a-c, comparing spent ceria catalysts tested in EB dehydrogenation both in absence and presence of CO_2. When tested in absence of CO_2 new bands evolved in the spectra at 368 cm^{-1}, 410 cm^{-1} and 530 cm^{-1} in addition to oxygen displacement band at 258 cm^{-1} [32]. These are the most pronounced for spent ceria rods (dashed red line) followed by ceria cubes (full blue line) and finally ceria particles (dashed black line).

When catalysts were tested in presence of CO_2 (Figure 3.6e), ceria cubes showed the most pronounced new bands evolution (full blue line) followed by rods (dashed red line) and ceria particles (dashed black line). Remarkable, a very intense overall symmetric 464 cm^{-1} band broadening in the range 258-410 cm^{-1} and at the wavenumbers lower than 600 cm^{-1} was observed in the spectra of spent ceria cubes (full blue line).

3.4 DISCUSSION

3.4.1 Effect of shape on performance after deactivation

At any time on stream, in presence as well as absence of CO_2, the rate of EB conversion, as calculated from the data in Figure 3.2, normalized per catalyst's surface area is about two times higher for ceria cubes as compared to rods and particles (Figure 3.7). Similar trends have been reported by our group and assigned to the higher reactivity of (100) surfaces preferentially exposed in cubes in water gas shift reaction, compared to relatively inert (111) facets exposed at rods and particles [18]. For detailed surface characterization and identification of the exposed crystal planes for the three different morphologies, we refer

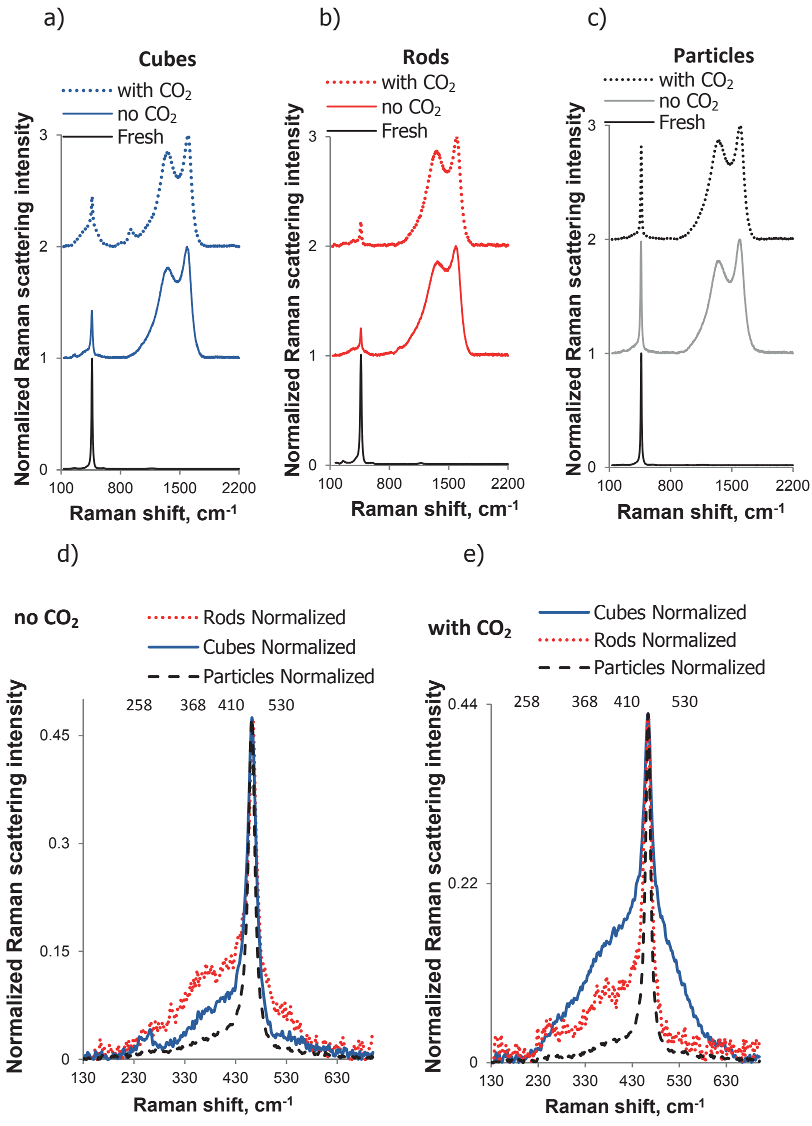

Figure 3.6. Raman spectra of fresh and spent ceria cubes (a), rods (b) and particles (c). Fresh spectra: black lines, spent when tested in presence of CO_2: upper dashed lines and in absence of CO_2 middle lines. Spectra were normalized per the most intense bands: in case of fresh spectra, 464 cm^{-1} band in case of spent spectra: 1552 cm^{-1} band. Spectra details for the spent ceria catalysts in absence of CO_2 :cubes (blue), rods (red) and particles (black) line (d). Spectra details for spent ceria catalysts in presence of CO_2: cubes (blue), rods (red) and particles (black) line. Spectra were scaled per 464 cm^{-1} band of the fresh catalysts for easier comparison.

to earlier work of our group [18]. Based on AC-HRTEM, providing resolution better then 1Å [24,27,33], it was revealed that mostly (111) surfaces are exposed at the surface of ceria rods and particles, whereas ceria cubes and expose mainly (100) surfaces. These ceria nanoshapes exhibited exactly the same trends in activity per surface area in WGS reaction as we report in this study (Figure 3.7) and elsewhere in RWGS reaction [30]. This is furthermore in agreement with the results reported for hydrogen and ethanol oxidation on pure and supported ceria nanoshapes [28,35]. Fundamental studies, though under very different conditions, report that (100) surfaces are more reactive towards methanol [36], water [37], acetaldehyde [38] and acetic acid [39] compared to (111) planes. They reveal that (100) ceria thin films are more susceptible for defects formation in the lattice relocating the surface charge to attain stability [40].

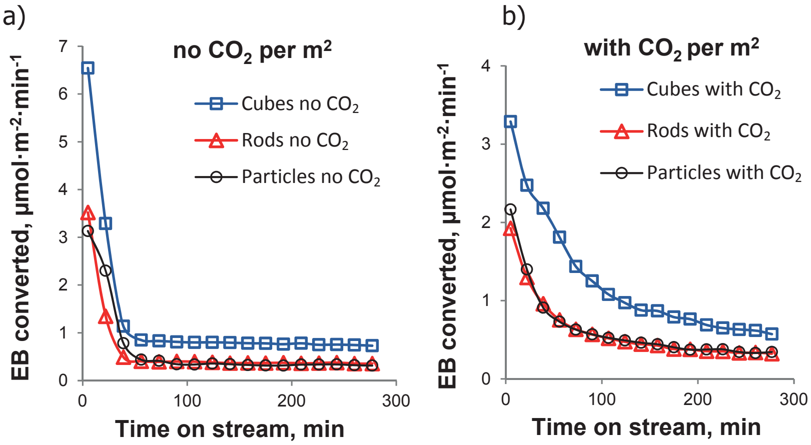

Figure 3.7. Converted amount of EB for various ceria nanoshapes per m^2 in absence of CO_2 (a) and in presence of CO_2 (b)

In absence of CO_2 direct dehydrogenation proceeds, as indicated by Sty/H_2 ratio of 1 corresponding to the stoichiometry of the dehydrogenation (reaction 3.1) (Figure 3.8, filled symbols).

$$EB \rightarrow Sty + H_2 \,(3.1) \qquad \text{(eq. 3.1)}$$

Addition of CO_2 does not affect the rate of EB conversion in steady state, as can be seen in Figure 3.2 and 3.7. However, in presence of CO_2 about 90% of the hydrogen has been consumed via RWGS (reaction 3.2, Figure 3.4) leading to Sty/H_2 ratios far above their stoichiometric values (Figure 3.8, empty symbols). The RWGS reaction is not in thermodynamic equilibrium in the steady state (Figure A3.5).

$$CO_2 + H_2 \rightarrow CO + H_2O \qquad \text{(eq. 3.2)}$$

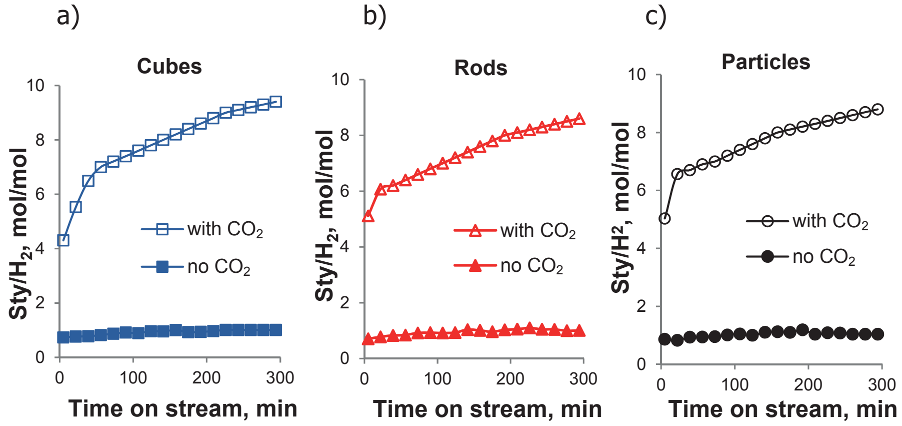

Figure 3.8. Molar ratio of styrene produced vs. hydrogen measured with and without CO_2 for ceria cubes (a), rods (b) and particles (c) in absence (filled symbols) and presence (empty symbols) of CO_2.

3.4.2 Changes in performance with time on stream

In absence of CO_2, EB conversion rate steeply decreased within initial 56 min TOS for all investigated catalysts (Figure 3.2, Figure 3.7). Initially, catalysts are in a high oxidation state contributing to enhanced by-products formation and decreased selectivity to styrene (Figure 3.3). The product distribution (Figure 3.3) and the sharp decrease in EB conversion rate we attribute to the consumption of ceria lattice oxygen, resulting in mainly toluene (reaction 3.3) and benzene (reaction 3.4) both accompanied with CO formation (Figure 3.4), schematically presented in equations 3.3 and 3.4.

$$\mathrm{EB} + \mathrm{CeO_2} \rightarrow \mathrm{Tol} + \mathrm{CO} + \mathrm{H_2} + \mathrm{CeO_{2\text{-}x}} \qquad \text{(eq. 3.3)}$$

$$\mathrm{EB} + \mathrm{CeO_2} \rightarrow \mathrm{Benz} + 2\mathrm{CO} + 2\mathrm{H_2} + \mathrm{CeO_{2\text{-}x}} \qquad \text{(eq. 3.4)}$$

Further, a lower amount of Sty compared to H_2 is observed in the first hour on-stream (Figure 3.8, filled symbols), indicating that styrene and by-products have been further condensed into carbonaceous deposits, as confirmed by TGA (Figure 3.5) and Raman (Figure 3.6a-c) results.

From the integrated amount of CO produced during initial 56 min TOS according to reactions 3.3 and 3.4, we estimated the amount of lattice oxygen species extracted by EB (Table 3.2). It should be noted that the numbers presented in Table 3.2 are based on the assumption that production of toluene and benzene is accompanied by hydrogen formation (reactions 3.3 and 3.4). Water formation was below the detection limit. The amount of hydrogen expected to be produced according reactions 3.1, 3.3 and 3.4 is compared to the amount of hydrogen actually measured in Figure A3.6 (Appendix 3). For ceria rods and cubes we obtained excellent agreement between measured and calculated values indicating that estimated numbers in Table 3.2 are correct and that water formation is negligible. In case of ceria particles, a minor difference between calculated and measured H_2 is observed, initially. This may be attributed to initial formation of hydrogen containing species

Table 3.2. The amount of lattice oxygen extracted by EB calculated based on CO integrated amount produced in absence of CO_2

	Cubes	Rods	Particles
µmol O·g^{-1}	477 ± 24	508 ± 25	197 ± 10
µmol O·m^{-2}	13,0 ± 0,6	7,0 ± 0,4	8,2 ± 0,4
ML*	~ 2,2	~ 1,42	~ 1,30

* the amount of extracted surface/lattice oxygen species *vs*. theoretical monolayer capacity [µmol/µmol]

(cracking products) following benzene and toluene formation initially. However, we cannot rule out formation of water, introducing a minor error in the numbers for particles in Table 3.2.

As shown in Table 3.2 the amount of lattice oxygen extracted per m^2 decreases in the following order: cubes > particles ~ rods, resembling the order in the catalytic activity per m^2 (Figure 3.7). We assign this to the presence of the highly intrinsically stabile (111) crystal planes exposed, the lowest amount of oxygen species has been extracted from the surface of ceria rods. Contrary, at the (100) crystal planes of ceria cubes with lower energy of formation of oxygen vacancies [19,20], approximately double amount of oxygen species has been extracted by EB per m^2. The extent of reduction is relatively mild, although the amount of oxygen removed is exceeding somewhat the monolayer capacity (Table 3.2) [26,41]. Therefore, removal of oxygen is not confined to the surface, but sub-surface or bulk are contributing, as would be expected for ceria. As deduced from hydrogen balance (Figure A3.6, Appendix 3), surface lattice oxygen species initially participate in nonselective EB conversion pathways (reactions 3.3 and 3.4) while styrene formation follows a simple dehydrogenation route (reaction 3.1). The amount of styrene initially formed is below the thermodynamic equilibrium of the dehydrogenation reaction (Figure A3.7, Appendix 3) [42]. As deduced from Figure 3.7a and Table 3.2, more reducible surfaces (ceria cubes compared to rods and particles) exhibited higher activity for EB dehydrogenation both initially and after stabilization. We suggest that in steady state, oxygen deficient Ce^{3+}-O-Ce^{4+} sites, generated upon removal of surface lattice oxygen species, are active for dehydrogenation of EB to styrene, as demonstrated previously [14]. Even in absence of an oxidant, oxygen deficient surfaces of ceria cubes exhibited higher activity compared to rods and particles (Figure 3.7a). We can not however rule out that the difference is caused by difference in surface structure of (111) terminated surface *versus* (100) terminated surfaces.

Pre-treatment with CO_2 resulted in a significantly lower initial EB conversion for all samples (Figure 3.2). This might be ascribed to the presence of carbonate [43] hindering both reaction pathways, *i.e.* nonselective EB conversion involving O species and selective styrene formation on reduced active sites. Strong interaction of ceria with CO_2 has been suggested to inhibit the Ce/AC reactivity in EBDH with CO_2 in the temperature range 550-650°C [44]. However, the fact that the EB conversion profiles in absence and presence of CO_2 are crossing each other, (Figure 3.2) suggest that these carbonate species probably decomposed in the course of the reaction. In presence of CO_2, all the catalysts approached the equilibrium oxidation state in steady state slower as compared to in absence of CO_2 (Figure 3.2). CO_2 is probably partially replenishing consumed active oxygen species prolonging the time needed to reach equilibrium oxidation state of the catalyst in absence of CO_2 (reaction 3.6) [9,10].

Partial re-oxidation of CeO_{2-x} with CO_2 has indeed been reported before [45]. The creation of active oxygen species by CO_2 dissociation to CO and O [11] apparently affects the product distribution, i.e. more benzene (equation 3.4) compared to toluene (reaction 3.3) has been initially produced (Figure 3.3). This was accompanied by slightly higher coke accumulation as compared to results obtained in absence of CO_2 (Figure 3.5), which seems reasonable because benzene is a well-known precursor in coke formation.

$$CO_2 + CeO_{2-x} \rightarrow CO + CeO_2 \qquad \text{(eq. 3.5)}$$

We further estimated the cumulative amount of toluene and benzene produced prior reaching stable EB conversion levels, to evaluate initial catalytic performances of these ceria nanoshapes in EBDH in presence of CO_2 (Table 3.3).

As shown in Table 3.3 the amount of toluene and benzene produced per gram decreases in the following order: cubes > rods > particles. When expressed per surface area, these amounts decrease as follows: cubes > rods ~ particles, resembling the trends in catalytic activity (Figure 3.7) and the order of the amount of extracted oxygen species by EB per m^2 in absence of CO_2 (Table 3.2). Apparently, there is a correlation between the amount of O species per surface area that can be extracted by EB and the integrated amount of by-products formed in presence of CO_2 per surface area (Figure 3.9). This suggests that formation of by-products proceeds according reactions 3.3 and 3.4, both in presence and absence of CO_2 and that extractable O species also constitute active sites for initial by-product formation, which initially can be re-activated by CO_2 in a Mars Van Krevelen mechanism via reaction 3.5.

EBDH with CO_2 can proceed via either an one-step pathway, *i.e.* a direct oxidation of EB with CO_2 (reaction 3.6) in a concerted manor, or via a two-step pathway: dehydrogenation (reaction 3.1) followed by RWGS (reaction 3.2) [46,47].

$$EB + CO_2 \rightarrow Sty + CO + H_2O \qquad \text{(eq. 3.6)}$$

First, we compare the measured amount of hydrogen with the theoretical value assuming that the RWGS reaction is in equilibrium (calculated with equation 3.3, experimental part).

Table 3.3. The integrated amount of Toluene and Benzene produced in presence of CO_2

	Cubes	Rods	Particles
µmol Toluene·g^{-1}	193 ± 10	144 ± 7	50 ± 3
µmol Toluene·m^{-2}	5,4 ± 0,3	2,0 ± 0,1	2,2 ± 0,1
µmol Benzene ·g^{-1}	547 ± 27	378± 19	124 ± 6
µmol Benzene·m^{-2}	15,2± 0,8	5,2 ± 0,3	5,2 ± 0,3

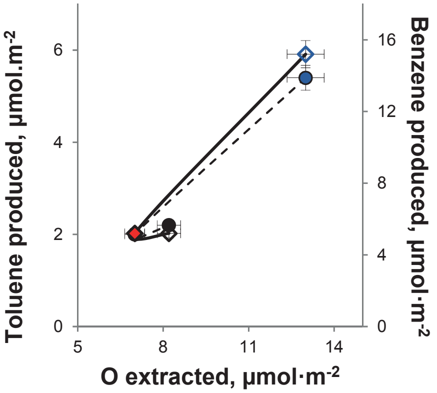

Figure 3.9. Amount of toluene (filled cycles) and benzene (empty diamonds) produced in presence of CO_2 per m^2 vs. the amount of lattice oxygen species extracted by EB in absence of CO_2 per m^2.

After an initial period, the measured concentration of H_2 is higher than the calculated value at RWGS equilibrium (Figure A3.8, Appendix 3). This means that H_2 must be a primary product and that RWGS is relatively slow, which seems reasonable for ceria, clearly indicating that a two-step pathway is proceeding. Likewise, the concentration of produced CO is well below the CO concentration calculated according the WGS equilibrium (Figure A3.9, Appendix 3). Therefore, CO cannot be a primary product, proving that an one-step pathway (reaction 3.6) followed by WGS, can be excluded.

In contrast, one step pathway has been reported as the main route over Na_2O/Al_2O_3 and V/Al_2O_3 catalyst, while over Fe_2O_3/Al_2O_3 both pathways have been reported to proceed [44,45,46]. Both pathways have also been suggested for V-MCM-41, Cr-MCM-41, Cr/AC and Ce/AC catalysts [48,49]. It is not possible to rule out a minor contribution of a direct pathway in this study, but it is evident that the two step pathway via dehydrogenation and RWGS is the dominant pathway over ceria under the conditions in this study.

3.4.3 Characterization of the spent ceria catalysts with Raman spectroscopy

When catalysts were tested both in absence and presence of CO_2, pronounced broadening of the 464 cm^{-1} peak has been observed due to evolution of new bands (Figures 3.6 d and e). In absence of CO_2, this was the most pronounced for ceria rods, followed by cubes and finally particles (Figure 3.6d). In presence of CO_2, the observed trends were in the order cubes >> rods > particles (Figure 3.6e). Broadening is known to be associated with expansion of the ceria lattice induced by formation of defects [50,51,52].

Moreover, lattice expansion/ distortion as observed is in line with the evolution of the band near 530 cm^{-1}, originating from the formation of oxygen vacancies. Bands at 540-560 cm^{-1} and 562 to 599 cm^{-1} have been assigned to vacancies in doped and pure ceria, respectively [53,54]. Recently, our group suggested that shoulders at 404 and 487 cm^{-1} arise due to formation of defects, as studied by UV Raman spectroscopy [55]. Without going into the depth, we used Raman spectroscopy as a finger print technique to detect the degree of reduction of catalysts after EB dehydrogenation. The amount of extracted lattice O species by EB in absence of CO_2 (Table 3.2) correlates with the intensity of both 368 and 530 cm^{-1} bands (Figure 3.6 d). Clearly, the intensity of both 368 cm^{-1} and 530 cm^{-1} bands increased with increasing amount of lattice O extracted by ethylbenzene (Figure 3.10a). The band at 368 cm^{-1} is taken as a measure of the degree of the fluorite lattice distortion and the band at 530 cm^{-1} is a measure for oxygen vacancy abundance in the spent ceria sample.

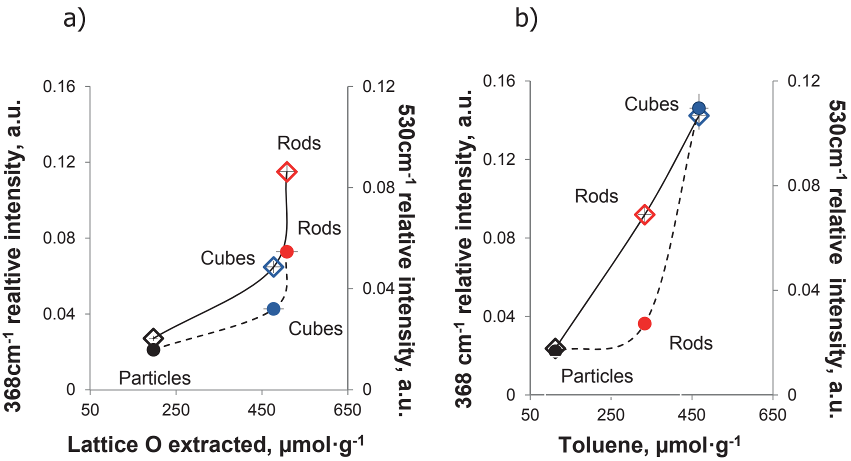

Figure 3.10. Correlation between intensity of Raman at 368cm^{-1} (empty diamonds) and 530cm^{-1} (filled cycles) with the amount of lattice oxygen species extracted by EB in absence of CO_2 (a) and the amount of toluene produced in presence of CO_2 (b).

Further, the cumulative amount of toluene produced in presence of CO_2 (Table 3.3), which is an indirect measure for the amount of extractable lattice oxygen as discussed above, correlates with both 368 and 530 cm^{-1} band intensities (Figure 3.6 d, Figure 3.10 b). As presented in Figure 3.10, the degree of reduction of ceria nanoshapes after EB dehydrogenation has a relation with the amount of oxygen species extracted in absence and presence of CO_2. In absence of CO_2 ceria cubes and rods have the highest reduction degree (Figure 3.10a), while in presence of CO_2 the reduction degree induced by EB in spent ceria catalysts is highest for ceria cubes (Figure 3.10b). The fact that the order changes on adding CO_2, may hint that the reactivity of CO_2 with the surface of the nanoparticles may be structure sensitive. Spent ceria rods in presence of CO_2 exhibited bigger difference of relative intensity of Raman bands at 368 cm^{-1} and 530 cm^{-1} compared to cubes and particles. This clearly indicates that the interaction of CO_2 with the surface of ceria rods is different compared to cubes and particles. This may be attributed to differences in the surface structure, i.e. ceria rods possess higher fraction of surface steps, voids, internal pores compared to particles (and cubes) [18], or it may be due to clustering of vacancies as reported in [17].

Although Raman spectroscopy measurements were performed ex-situ, and the oxidation state of the catalysts is very likely to change with exposure to ambient conditions, the trends in the degree of reduction are apparently still preserved. Also, deposition of carbon does apparently not mask the effect.

3.5 CONCLUSION

EBDH over cerium oxide catalysts of various morphologies, *i.e.* cubes, rods and particles, show similar behaviour. Initially, oxygen rich ceria causes over-oxidation of EB, forming CO, benzene, and toluene. Presence of CO_2 increased the amount of oxygen species available via a Mars Van Krevelen mechanism, prolonging the time window in which by-products are formed, before reaching stable operation with high selectivity to styrene. Removal of oxygen is qualitatively in agreement with the formation of oxygen vacancies and lattice distortion as observed with Raman spectroscopy. After reaching stable operation, dehydrogenation is found to proceed via a two-step pathway, *i.e.* EB dehydrogenation followed by consecutive RWGS reaction in case CO_2 is present. Cubes, having specifically exposed (100) crystal planes of low intrinsic stability provide more oxygen during initial formation of CO, benzene and toluene. In addition, in stable operation ceria cubes exhibited remarkable higher activity per m^2 for dehydrogenation of EB as compared to rods and particles, suggesting that EB dehydrogenation proceeds on partly-reduced surface sites.

APPENDIX 3

Table A3.1. The amount of the catalyst used for the testing (mg)

	Cubes	Rods	Particles
With CO_2	58	44	142
No CO_2	40	35	142

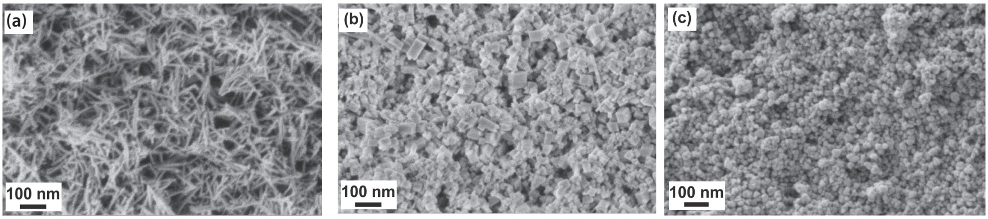

Figure A3.1. SEM images of ceria rods (a), cubes (b) and particles (c).

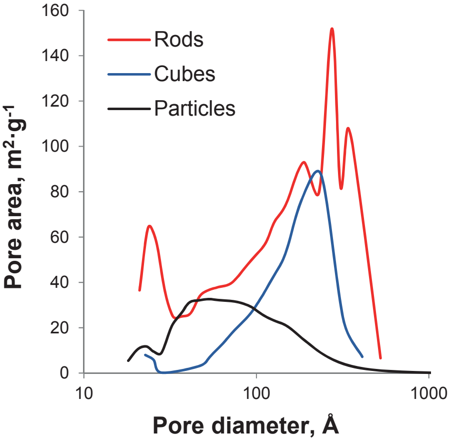

Figure A3.2. Pore size distribution for ceria rods, cubes and particles

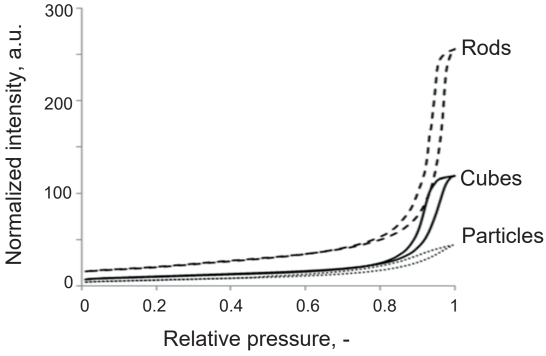

Figure A3.3. Adsorption/desorption hysteresis for ceria rods, cubes and particles

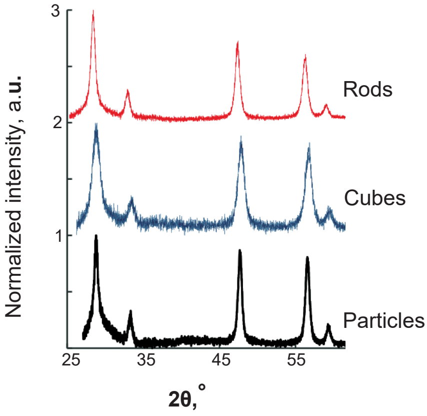

Figure A3.4. XRD patterns for ceria rods, cubes and particles

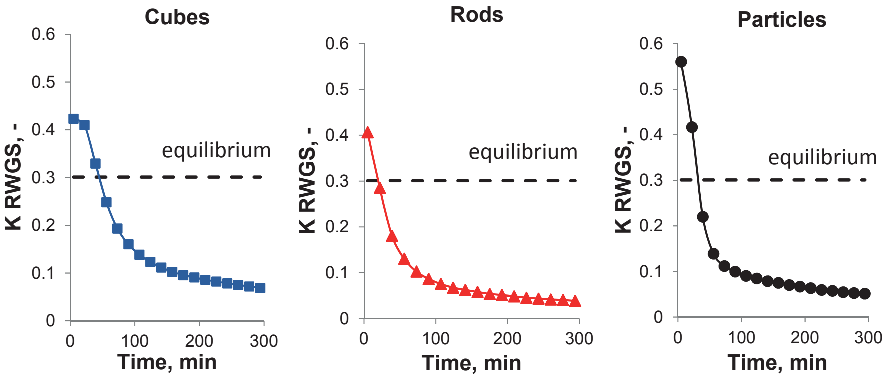

Figure A3.5. Comparison: the calculated K_{RWGS} (reverse water gas shift) vs. equilibrium K_{RWGS}

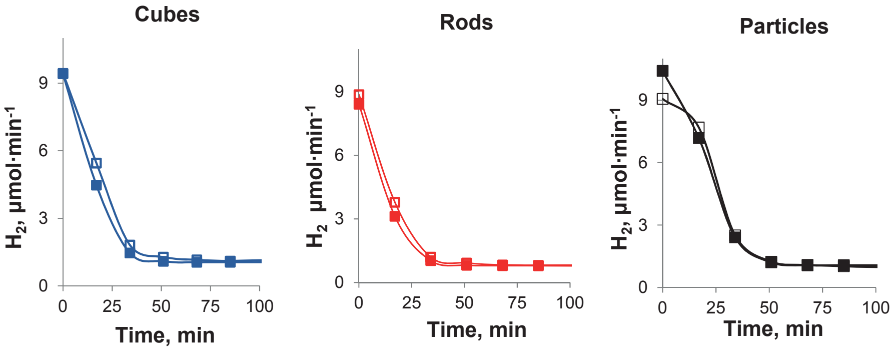

Figure A3.6. Amount of hydrogen measured (empty symbols) vs. cumulative amount of hydrogen (calculated, filled symbols) expected to be produced following simple dehydrogenation: EB → Sty + H_2 and by-products formation: EB + CeO_2 → Tol + CO+ H_2 + CeO_{2-x}
and EB + CeO_2 → Benz + 2CO+ $2H_2$ + CeO_{2-x}

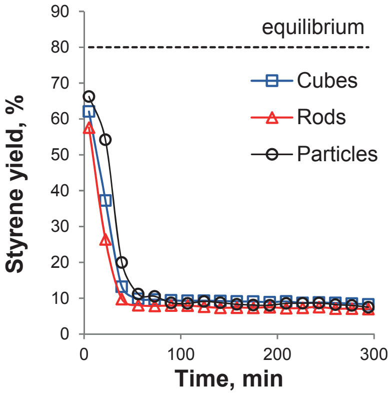

Figure A3.7. Styrene yield measured vs. styrene yield compared to thermodynamic equilibrium.

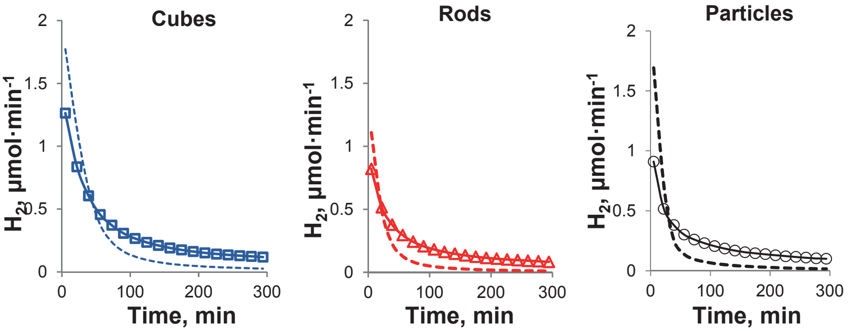

Figure A3.8. Comparison: the amount of hydrogen measured (line with symbols) vs. calculated at the reverse water gas shift (RWGS) equilibrium (dashed line)

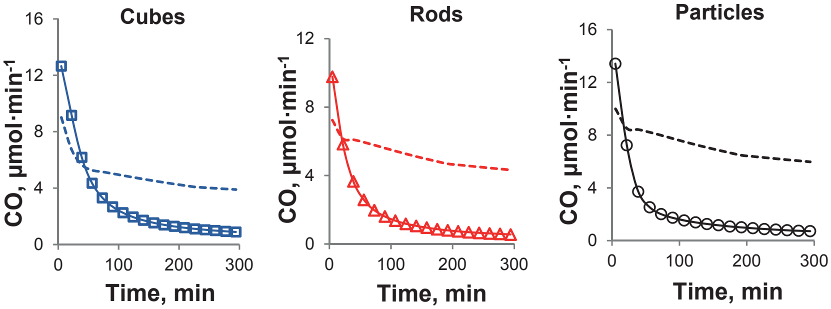

Figure A3.9. Comparison of the amount of CO measured (line with symbols) vs. calculated at the water gas shift (WGS) equilibrium (dashed line).

BIBLIOGRAPHY

1. G.R. Meima, P.G. Menon, Appl. Catal. A: Gen. 212 (2001) 239-245.
2. F. Cavani, F. Trifiro, Appl. Catal. A: Gen. 133 (1995) 219-239.
3. J.S. Chang, S.E. Park, M.S. Park, Chem. Lett. 26 (1997) 1123-1124.
4. M. Sugino, H. Shimada, T. Turuda, H. Miura, N. Igenaga, T. Suzuki, Appl. Catal. A 121 (1995) 125-137.
5. Y. Sukurai, T. Suzaki, K. Nakagawa N. Ikenaga, H. Aota, T. Suzuki, Chem.Lett. 29 (2000) 526-527.
6. Y. Sukurai, T. Suzaki, K. Nakagawa, N. Ikenaga, H. Aota, T. Suzuki, J.Catal 209 (2002) 16-24.
7. S. Chen, Z. Qin, A. Sun, J. Wang, J. Natural Gas Chem. 15 (2006) 11-20.
8. J.A. Moulijn, M.B. Cerfontain, F. Kapteijn, 63 (1984) 1043–1047.
9. M.B. Ansari, S.E. Park, Energy Environ.Sci. 5 (2012) 9419-943.
10. K. Saito, K. Okuda, N.O. Ikenaga, T. Miyake, T. Suzuki, J. Phys. Chem. A 114 (11) 488 (2010) 3845–3854.
11. J.-S. Chang, V.P. Vislovsky, M.-S. Park, D.Y. Hong, J.S. Yoo, S.-E. Park, Green Chem. 5 (2003) 587-590.
12. P. Mars, D.W. van Krevelen, Spec. Suppl .Chem. Eng. Sci. 3 (1954) 41–59.
13. J. Xu, L-C. Wang, Y-M. Lui, Y. Cao, H.-Y. He, K.-N. Fan, Catal. Lett. 133 (2009) 307-313.
14. B. Murugan, A.V. Ramaswamy, J. Am. Chem. Soc 129 (2007) 3062-3063.
15. D. R. Burri, K.-M. Choi, J.-H. Lee, D.-S. Han, S.-E. Park Catal. Commun. 8 (2007) 43–48.
16. A. Trovarelli, Catal. Rev. 38(4) (1996) 439–520.
17. X. Liu, K. Zhou, L. Wang, B. Wang, Y. Li, J. Am. Chem. Soc. 131 (2000) 3140-3141.
18. S. Agarwal, L. Lefferts, B.L. Mojet, D.A.E. Ligthart, E.J.M. Hensen, D.R.G. Mitchell, W.J. Erasmus, B.G. Anderson, E.J. Olivier, J.H. Neethling, A.K. Datye, ChemSusChem 6 (10) (2013) 1898-1906.
19. D.C. Sayle, S.A. Maicaneanu, G.W. Watson, J. Am. Chem. Soc 124 (2002) 11429-11439.
20. T.X.T. Sayle, S.C. Parker, C.R.A. Catlow, Surf. Sci. 316 (1994) 329-336.
21. J.A. van Bokhoven, ChemCatChem 1 (2009) 363-364.
22. D. Zhang, X. Du, L. Shi, R. Gao, Dalton Trans. 41 (2012) 14455-14475.
23. A. Tschope, W. Liu, M. Flytzani-Stephanopoulos, J. Y. Ying, J. Catal. 157 (1995) 42 – 50.
24. K. Zhou, X. Wang, X. Sun, Q. Peng, Y. Li, J. Catal. 229 (2005) 206-212.
25. Q. Dai, H. Huang, Y. Zhu, W. Deng, S.Bai, X.Wang, G.Lu, Appl. Catal. B: Environ. 117-118 (2012) 360-368.
26. L. Liu, Y. Cao, W. Sun, Z. Yao, B. Liu, F. Gao, L. Dong, Catal. Today 175 (2011) 48-54.
27. H.-X. Mai, L.-D. Sun, Y.-W. Zhang, R. Si, W. Feng, H.-P. Zhang, H.-C. Liu, C.-H. Yan, J. Phys. Chem. B 109 (2005) 24380 – 24385.
28. T. Dasaunay, G. Bonura, V. Chiodo, S. Freni, J.-P. Couzinie, J. Bourgon, A. Ringuede, F. Labat, C. Adamo, M. Cassir, J. Catal. 297 (2013) 193-201.
29. M. Kovacevic, R. Brunet Espinosa, L. Lefferts, B.L. Mojet, Appl. Catal. A: Gen. 469 (2014) 1-7.
30. M. Kovacevic, B.L. Mojet, J.G. van Ommen, L. Lefferts, Catal. Lett. 146 (2016) 770-777.
31. C. Nederlof, G. Talay, F. Kapteijn, M. Makkee, Appl. Catal. A: Gen. 423-424 (2012) 59-68.
32. S. Meriani, S. Spinolo, Powder Diffr. 2 (4) (1987) 255-256.
33. Z. Wu, M. Li, J. Howe, H.M. Meyer III, S.H. Overbury, Langmuir 26 (2010) 16595–16606.
34. N. Larouche, B.L. Stansfield, Carbon 48 (2010) 620-629.
35. H. Li, G. Qi, Tana, X. Zhang, W. Li, W. Shen, Catal. Sci. Technol. 1 (2011) 1677-1682.
36. D.R. Mullins, P.M. Albrecht, Langmuir 29 (2013) 4559-4567.
37. M. Molinari, S.C. Parker, D.C. Sayle, M.S. Islam, J. Phys. Chem. C 116 (2012) 7073–7082.
38. D.R. Mullins, P.M. Albrecht, J. Phys. Chem. C 117 (2013) 14692-14700.
39. D.R. Mullins, P.M. Albrecht, F. Calaza, Top. Catal. 56 (2013) 1345-1362.
40. H. Nörenberg, J.H. Harding, Surf. Sci 477 (2001) 17-24.
41. Y. Madier, C. Descorme, A.M.L. Govic, D. Duprez, J. Phys. Chem. B 103 (1999) 10999-11006.
42. N. Mimura, M. Saito, Catal. Lett. 55 (2000) 173-178.
43. M. Nolan, G.W. Watson, J. Phys. Chem. B 110 (2006) 16600–16606.
44. N. Ikenaga, T. Tsuruda, K. Senma, T. Yamaguchi, Y. Sakurai, T. Suzuki, Ind. Eng. Chem. Res. 39 (2000) 1228-1234.
45. T. Staudt, Y. Lykhach, N. Tsud, T. Skála, K.C. Prince, V. Matolín, J. Libuda, J.Catal. 275 (2010) 181–185.

46. N. Mimura, I. Takahara, M. Saito, T. Hattori, T. Ohkuma, M. Ando, Catal. Today 45 (1999) 61-64.
47. A. Sun, Z. Qin, S. Chen, J. Wang, J. Mol. Catal A: Chem. 210 (2004) 189-195.
48. Y. Qiao, C. Miao, Y. Yue, Z. Xie, W. Yang, W. Hua, Z. Gao, Micropor.Mesopor.Mat. 119 (2009) 150-157.
49. Y. Ohishi, T. Kawabata, T. Shishido, T. Takaki, Q. Zhang, Y. Wang, K. Takehira, J. Mol. Cat. A: Chem. 230 (2005) 49-58.
50. F. Zhang, S.-W. Chan, J.E. Spanier, E. Apak, Q. Jin, R.D. Robinson, I.P. Herman, Appl. Phys. Lett. 80 (2002) 127.
51. J.E. Spanier, R.D. Robinson, F. Zhang, S.-W. Chan, I.P. Herman, Phys. Rev. B 64 (2001) 245407.
52. S. Tsunekawa, K. Ishikawa, Z.-Q. Li, Y. Kawazoe, A. Kasuya, Phys. Rev. Lett. 85 (2000) 3440-3443.
53. S. Patil, S. Seal, Y. Guo, A. Schulte, J. Norwood, Appl. Phys. Lett. 88 (2006) 243110.
54. Y. Lee, G. He, A.J. Akey, R. Si, M. Flytzani-Stephanopoulos, I.P. Herman, J. Am. Chem. Soc. 133 (2011) 12952-12955.
55. S. Agarwal, X. Zhu, E.J.M. Hensen, L. Lefferts, B.L. Mojet, J. Phys. Chem. C 118 (2014) 4131-4142.

4

EFFECTS OF MORPHOLOGY OF CERIUM OXIDE CATALYSTS FOR REVERSE WATER GAS SHIFT REACTION

ABSTRACT

Reverse water gas shift reaction (RWGS) was investigated over cerium oxide catalysts of distinct morphologies: cubes, rods and, particles. Catalysts were characterized by X-ray diffraction, Raman spectroscopy, and Temperature programmed reduction (TPR) in hydrogen. Nanoshapes with high concentration of oxygen vacancies contain less surface oxygen removable in TPR. Cerium oxide cubes exhibited two times higher activity per surface area as compared to rods and particles. Catalytic activity of these nanoshapes in RWGS reaction exhibited a relation with the lattice microstrain increase, however, a causal relationship remained unclear. Results presented in this study suggest that superior catalytic activity of ceria cubes in RWGS originates from the greater inherent reactivity of (100) crystal planes enclosing cubes, contrary to less inherently reactive (111) facets exposed at rods and particles.

Keywords: Reverse water gas shift; ceria cubes; rods; particles

Published as: M. Kovacevic, B.L. Mojet, J.G. van Ommen, L. Lefferts, Catal. Lett. 146 (2016) 770-777.

4.1 INTRODUCTION

Catalytic conversion of CO_2 to CO via RWGS reaction is a promising alternative for CO_2 utilization [1,2]. Water gas shift (WGS) and RWGS occur in all chemical processes when CO_2 and H_2, or CO and H_2O coexist in a reaction mixture [2]. RWGS is reported to increase the desired product yield at equilibrium when coupled with dehydrogenation of hydrocarbons [3,4,5]. WGS is commonly used in combination with steam reforming of hydrocarbons aiming to maximize hydrogen yield [6,7,8]. It plays an vital role in Fischer-Tropsch synthesis, ammonia and methanol production. Two extensively discussed mechanisms in literature for (R)WGS are redox and associative formate decomposition [9]. Efficient catalysts have been designed for low and high temperature applications. However, designing an robust and active catalyst that can operate in a single stage (R)WGS reactor still remains a challenge [10,11].

Cerium oxide is widely employed in catalysis because of its unique oxygen storage capacity (OSC), the ability to reversibly store and release oxygen while formally switching between Ce^{4+} to Ce^{3+} in a stable fluorite lattice [12]. The degree of the oxygen - ion mobility in the ceria lattice is associated with the size, dispersion and abundancy of oxygen vacancy defects [13,14,15]. Theoretically, oxygen vacancy formation and ability of the catalyst to act as oxygen donor-acceptor is related to the stability of particular crystal facets of the ceria surface [16,17]. Although discrepancy in literature exist regarding exposed crystal planes at the surfaces of ceria rods, recent studies in our group demonstrated that stable (111) crystal planes are mainly exposed at the surface of both ceria rods and octahedra while ceria cubes are enclosed by mainly (100) crystal terminations [18]. Therefore, manipulation of catalyst shape is an approach for tuning the fraction of reactive crystal planes at the ceria surface and this is becoming a novel strategy in obtaining advanced catalytic materials with superior OSC and catalytic reactivity [19,20].

Ceria nanocubes of average 10 nm size exhibit considerable OSC at a temperature as low as 150°C, that is for 250°C lower than the temperature needed for cerium oxide particles of irregular shape to exhibit comparable OSC [21]. Enhanced OSC of cube and rod shaped ceria originate both from its surface and bulk structure [22].

Ceria nanoshapes have been investigated in *i.e.* CO oxidation [23,24,25], NO reduction [26], and WGS reaction [27]. Ceria nanorods exhibited superior activity in oxidation of CO, 1,2-dichlorethane, ethyl-acetate and ethanol [19,28,29,30], methanol conversion in presence of CO_2 [31], methanol [32] and acetaldehyde decomposition [33] compared to ceria cubes and octahedra. Moreover, shuttle-shaped particles composed of closely packed ceria nanorods displayed higher activity for CO oxidation compared to ceria nanorods [34], which is attributed to an enhanced porosity, surface area, and oxygen deficiency of these samples compared to ceria rods.

Ceria nanocubes on the other hand displayed greater activity compared to nanoparticles of irregular morphology in the selective oxidation of toluene and benzene [35]. Pure and supported ceria nanocubes exhibited twice higher activity in oxidation of hydrogen and ethanol compared to rods and particles [36,37]. Similar trends were reported by our group in WGS and ethylbenzene dehydrogenation [18,38]. In this study we report the effect of well-defined morphologies of CeO_2 on catalytic activity during the RWGS reaction. To the best of our knowledge this has not been studied before.

4.2 EXPERIMENTAL PART

4.2.1 Materials

Commercially available NaOH pellets (Merck, 99%), $Ce(NO_3)_3{\cdot}6H_2O$ (99.99% Aldrich) and $Ce(OH)_4$ (Merck, 99%) were used for catalyst synthesis.

4.2.2 Catalyst preparation

Cerium oxide rods and cubes were prepared modifying the synthesis procedure reported elsewhere [25]. In the preparation of ceria rods 1.75g of $Ce(NO_3)_3{\cdot}6H_2O$ was first dissolved in 11 ml of distilled water. The solution was rapidly added to 73 ml of 10 mass % NaOH aqueous solution. In the preparation of ceria cubes mixing was performed *vice versa:* NaOH aqueous solution was rapidly added to previously dissolved $Ce(NO_3)_4{\cdot}6H_2O$ in distilled water. The resulting mixtures were stirred for 10 min (250 rpm), transferred into an autoclave (125 ml) which was placed in an oven at 130°C for 18 h and was allowed to cool to room temperature. Thus obtained precipitates were centrifuged at room temperature, rinsed with distilled water until pH= 7 was obtained and dried overnight at 110°C. Finally, the sample was calcined in flowing synthetic air at 650°C for 5 hrs. at the heating rate of $5°C{\cdot}min^{-1}$ Irregularly shaped ceria catalyst was obtained by calcining commercial $Ce(OH)_4$ under identical conditions.

4.2.3 Catalyst characterization

Catalysts surface area (BET) was determined by N_2-adsorption isotherm obtained at 77K (Micromeritics Tristar). The samples were outgassed in vacuum at 200°C for 24 h prior to analysis.

Catalyst morphology was studied by Scanning Electron Microscopy, (SEM) LEO 1550 FEG-SEM equipped with in-lens detector. Transmission electronic microscopy (TEM) images were obtained on a Philips CM300ST-FEG electron microscope operated at an acceleration voltage of 300kV. Samples for TEM measurements were ultrasonically dispersed in ethanol and subsequently droplets of the suspension were deposited on a copper grid coated with carbon.

X-ray diffraction (XRD) was performed a using PANalytical X´pert-APD powder diffractometer equipped with a position sensitive detector analyses over the 2θ-range between 25° and 65° using Cu Kα radiation, λ= 0.1544 nm. The average crystallite size was estimated using the Scherer's equation assuming spherical particle geometry. We further used peak width analysis to estimate lattice microstrain employing the equation [39,40]:

$$(\delta 2\Theta)^2/\tan^2\Theta_0 = K{\cdot}\lambda/(D{\cdot}(\delta 2\Theta/\tan\Theta_0{\cdot}\sin\Theta_0 + 16\varepsilon^2)) \qquad \text{(eq. 4.1)}$$

where Θ_0 stands for the position of peak maximum, $\delta 2\Theta$ denotes FWHM in radians, K is a Scherrer's constant that equals 0.9 assuming spherical grains, λ is the X-ray wavelength and D and ε represent the average grain size and the lattice microstrain, respectively. By plotting $(\delta 2\Theta)^2/\tan^2\Theta_0$ *vs.* $\delta 2\Theta/\tan\Theta_0{\cdot}\sin\Theta_0$ for several diffraction peaks, $K{\cdot}\lambda/D$ can be calculated from the slope, allowing determination of the crystallite size, while microstrain values can be extracted from the ordinate intercept which equals $16\varepsilon^2$. Scherrer's equation can be derived from equation 4.1 assuming that physical origin of the XRD peak broadening is due to the small grain size exclusively, neglecting any broadening caused by the strain accumulated in the lattice.

Raman spectroscopy measurements were performed with a Senterra Bruker instrument, equipped with a cooled CCD detector. The spectra were recorded at λ=532nm, with 2s integration time and 20 co-additions, 10mW laser power and at a resolution of 9-15 cm^{-1}. Spectra were measured *ex-situ* at room temperature in ambient air on as prepared catalysts (calcined and cooled to room temperature slowly in flowing air).

Temperature programmed reduction was performed in 5% H_2 in He with a heating rate of 5°C·min^{-1} from 30 to 600°C. 50mg of the catalyst was pre-treated at 450°C in oxygen for 60 min prior to analysis. Signals were recorder using TCD detector. Water has been removed using cold trap. System was calibrated with NiO.

4.2.4 Catalytic testing

The catalytic tests were performed at atmospheric pressure and isothermal conditions (560˚C) in a fixed-bed quartz tubular reactor (4.0 mm i.d.). The tests were carried out in 3% H_2, 37% CO_2 balance N_2, in a total flow of 30 ml·min^{-1}. Prior to reaction, catalysts were pretreated in pure N_2 at 580°C (30 min) and consequently in pure CO_2 at the reaction temperature (30 min). The amount of catalyst per run was tuned in such a way that CO_2 conversion was kept below 5%, ensuring differential experiments. Reaction products were analyzed by on-line GC Varian-450 equipped with TCD and FID detector and four columns: Hayesep T, Hayesep Q, Molsieve 13X, and CP-Wax. The experiments were reproducible with a typical overall error in the carbon mass balance smaller than 5%.

4.3 RESULTS AND DISCUSSION

4.3.1 Catalysts synthesis and characterization

Figure 4.1 shows the high resolution scanning electron microscopy (HRSEM) images of ceria catalysts obtained by three different routes: ceria rods (a), cubes (b) and particles (c). TEM images of these ceria nanoshapes clearly confirm distinct crystallite shape and morphology of these samples (Appendix 4, Figure A4.1) [38].

In this study ceria cubes were obtained at lower temperature and lower OH^- conc. (2 mol·L^{-1}) than commonly reported in literature (6 mol·L^{-1}) [22,41]. Several studies indicated that when both temperature and OH^- concentration are low (100°C, $C_{NaOH} < 1$ mol·L^{-1}) isotropic growth of $Ce(OH)_3$ nuclei proceeds resulting in ceria polyhedra formation [41,42,43]. However, at OH^- concentration above 1 mol·L^{-1} dissolution/ recrystallization is significant and anisotropic growth of $Ce(OH)_3$ nuclei is leading formation of rods, unless $Ce(OH)_3$ intermediate decomposes at higher temperatures (180°C) resulting in formation of cubes [22,41,42,43]. Apparently, the temperature of the hydrothermal treatment of 130°C in this study was sufficient to induce $Ce(OH)_3$ decomposition and consequently, the formation of ceria cubes. In this way, morphology of ceria can be controlled, even in absence of modifiers such as ethylenediamine inducing anisotropic crystal growth [44].

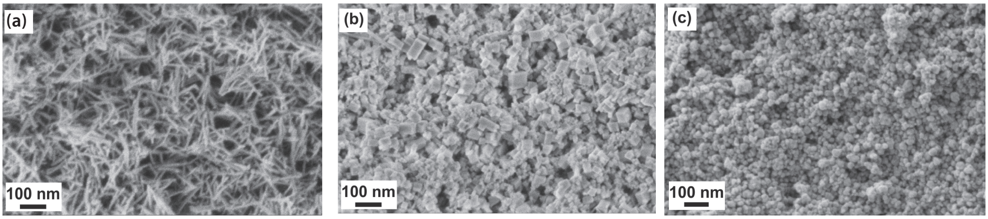

Figure 4.1. HRSEM images of ceria rods (a), cubes (b) and particles (c), adopted and modified from [38].

Table 4.1 shows the BET surface areas as determined by nitrogen physisorption, revealing decreasing surface area from rods to cubes and finally particles (Table 4.1).

Catalyst structure was further investigated by X-ray diffraction (XRD). Dominant Bragg diffractions were observed at 28.8°, 47.6°, and 56.7° 2θ, corresponding to respectively (111), (220) and (311) crystal planes of the fluorite fcc structure of CeO_2 (Figure 4.2) [34,45]. The average crystallite size as determined by the Scherrer's equation and equation 4.1, including micro-strain, increased in the order: cubes < rods < particles. These two methods result in identical numbers, considering the experimental error, indicating that peak broadening is dominated by the particle size effect over any effect of microstrain. Calculated crystallite size of ceria particles is consistent with the particle diameter deduced based on SEM images (Table 4.1, column c). Ceria rods have a width of about 10 nm and average length of 160 nm (Figure 4.1a), while the size estimated by XRD results in a value in between (Table 4.1). Average crystallite size of ceria cubes deduced from SEM images is 37 nm (Figure 4.1b), which is significantly higher compared to XRD estimate of 18 nm (Figure 4.1b, Table 4.1). Similar discrepancies in literature in case of ceria cubes were assigned to the broad crystallite size distribution, which is also evident in Figure 4.1b [46]. The assumption that crystallites have spherical geometry also contributes to this discrepancy.

Interestingly, the lattice microstrain is significantly higher in cubes than those in rods and particles (Table 4.1). Lattice microstrain is known to be associated with lattice expansion

Table 4.1. Catalysts structural and textural properties according N_2-physisorption, XRD and SEM; particle size calculated based on Scherrer's equation (a), eq. 4.1 including microstrain (b) and SEM images (c) and lattice microstrain, ε for ceria rods, cubes and particles.

Ceria morphology	**BET surface area (m^2/g)**	**Crystallite size, Scherrer's eq., d (nm)[a]**	**Crystallite size, eq. 4.1 including microstrain, d (nm)[b]**	**Crystallite size, SEM images, d (nm)[c]**	**Width particle-size distribution, SEM images (nm)[c]**	**Lattice microstrain, ε (%)**
Rods	73±4	24±1	25±2	10*	4	0,08±0,008
Cubes	37±2	18±1	19±2	37	20	0,15±0,02
Particles	24±1	30±1	30±3	26	6	0,08±0,008

* Denotes the width of ceria rods corresponding to the average length of 160 nm.

caused by increasing content of oxygen vacancies in the fluorite lattice [47]. Theoretical studies predicted decreasing energy of oxygen vacancy formation with increasing lattice microstrain [48]. Raman spectroscopy was, therefore, used to characterize the oxygen vacancy abundances. Figure 4.3a shows the Raman spectra of fresh ceria catalysts, as prepared. The spectra are dominated by a strong peak at 464 cm^{-1} from the F_2g mode of the CeO_2 fluorite lattice, in agreement with the XRD patterns (Figure 4.2) [48]. Two weaker bands identified are assigned to oxygen displacement (258 cm^{-1}) and oxygen vacancies (600 cm^{-1}) [49].

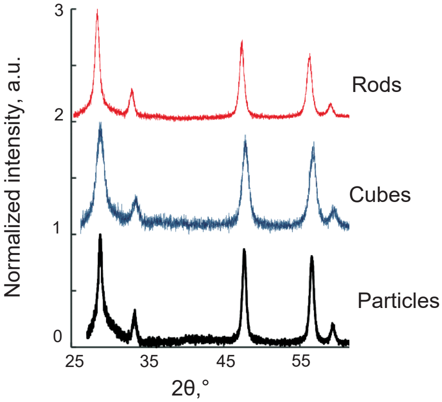

Figure 4.2. XRD patterns for rods, cubes and particles (from top to bottom)

As presented in Figure 4.3b, the intensities of oxygen displacement and oxygen vacancy bands are the highest for ceria rods, followed by ceria cubes and particles. These trends are further in agreement with the increasing broadening of the 464 cm^{-1} band in the order particles > cubes > rods (Figure 4.3b). Similar observation has been reported for ceria nanowires [50] and related to disorder in oxygen sub-lattice due to thermal and/ or grain size induced non-stoichiometry originating from combined effects of lattice strain and phonon confinement [51,52,53]. In this study, however, we observed no relation between the lattice micro-strain, estimated following the eq. 4.1 (Table 4.1) and Raman 464 cm^{-1} band broadening of these ceria samples (Figure 4.3). Total amount of oxygen consumed expressed per catalysts surface area, per gram and monolayer capacity (ML) is presented in Table 4.2.

Hydrogen temperature programmed reduction (H_2-TPR) was further used to study the reducibility of these ceria nanoshapes. TPR profiles of ceria particles (Figure 4.4) reveal a minor reduction peak at 210°C and the main reduction peak at about 485°C, while ceria cubes and rods have broad reduction peaks with maxima at 425°C and 560°C. Peaks below 600°C are assigned to consumption of surface oxygen [54], in contrast to reduction peaks above 800°C would indicate bulk reduction of CeO_2 to Ce_2O_3 [55].

Total amount of oxygen consumed expressed per catalysts surface area, per gram and monolayer capacity (ML) is presented in Table 4.2.

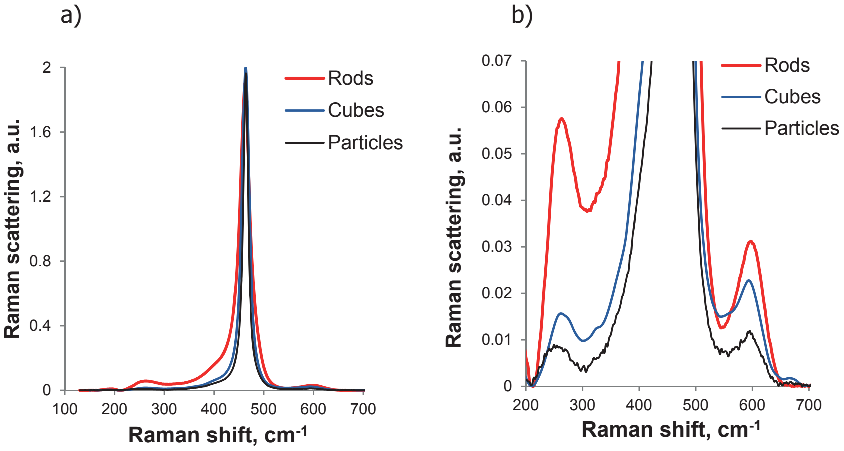

Figure 4.3. Full Raman spectra of ceria rods, cubes and particles (a); Oxygen displacement (258 cm^{-1}) and oxygen vacancy (600 cm^{-1}) vibration bands for cerium oxide rods, cubes, and particles (b). The spectra are normalized on the intensity of the main peak at 464 cm^{-1}.

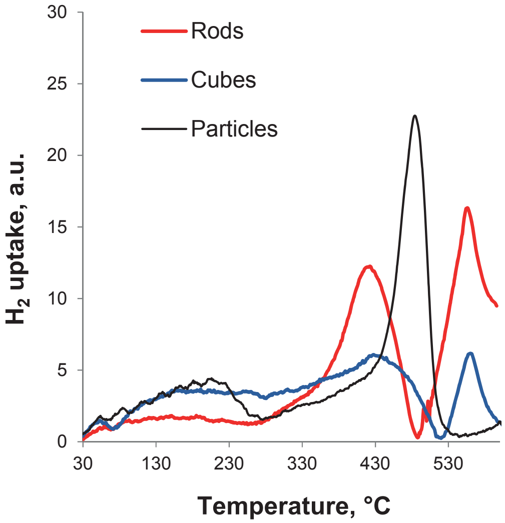

Figure 4.4. H_2-TPR results for ceria rods, cubes and particles

When normalized per surface area overall reducibility of these catalysts decrease from ceria particles to cubes and finally rods (Table 4.2). The amount of consumed oxygen species is below one monolayer for all the investigated catalysts (Table 4.2).

4.3.2 Catalytic testing results in RWGS reaction

Catalytic activity of the ceria catalysts was investigated in RWGS reaction at 560°C. Figure 4.5 compares catalytic activities of ceria cubes, rods and particles expressed as the amount

Table 4.2. The overall amount of oxygen consumed in H_2-TPR normalized per m^2, gram and expressed as theoretical monolayer capacity (ML) on ceria rods, cubes and particles*.

Ceria morphology	µmol·m^{-2}	µmol·g^{-1}	Monolayer capacity (ML)*,**
Rods	1,1 ± 0,05	81 ± 4	0,19
Cubes	1,8 ± 0,1	63 ± 3	0,29
Particles	3,7 ± 0,2	84 ± 4	0,62

* the amount of consumed surface oxygen species vs. theoretical monolayer capacity (ML) [µmol/µmol].

**numbers significantly differ from the amounts presented in Table 3.2. This could be ascribed to the different surface chemistry of EB and H_2 with ceria surfaces.

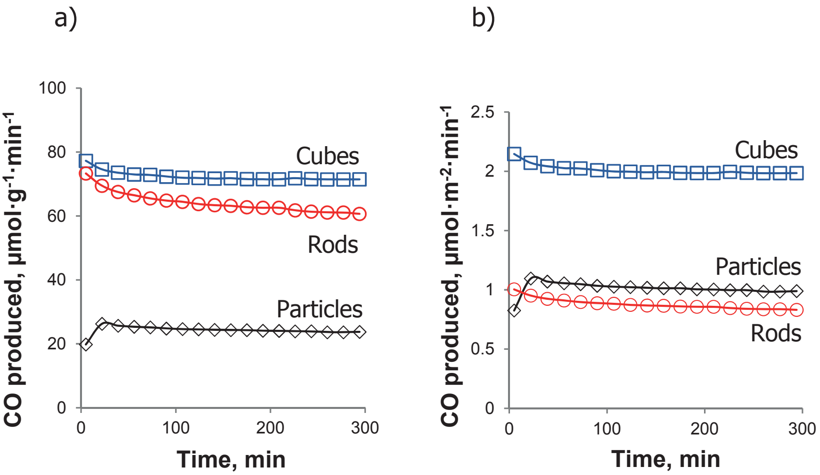

Figure 4.5. Catalytic activity of ceria rods, cubes and particles expressed as the rate of CO production per g (a) and m^2 (b).

of CO produced per gram of ceria (Figure 4.5a) and per m^2 (Figure 4.5b). Ceria cubes are the most active compared to the other two morphologies, both per gram and per m^2. Catalytic activity of ceria rods is slightly lower per gram compared to that of cubes and about two times lower per m^2. Ceria particles show about two times lower activity compared to cubes both per gram and per m^2. Minor deactivation was observed in all cases.

4.3.3 Discussion

Oxygen vacancy abundances in these ceria catalysts decrease in the order: rods > cubes > particles (Figure 4.3b), consistent with results in literature revealing higher intrinsic oxygen deficiency in ceria rods compared to cubes and octahedra [46]. It is reasonable to assume that bulk oxygen deficiency induces oxygen deficiency at the surface of these nanoshapes. TPR shows that reduction below 600°C results in removal of oxygen in sub-monolayer amounts (Table 4.2), which is well in agreement with the claim that only surface oxygen is involved [54] when reducing ceria below 600°C. Comparison of Raman spectroscopy and TPR results confirms that catalysts with higher abundancy of oxygen vacancies according Raman spectroscopy (rods > cubes > particles) indeed contain less reducible surface oxygen species (rods < cubes < particles, Table 4.2).

Ceria cubes contain more lattice microstrain compared to rods and particles (Table 4.1). Increasing lattice microstrain is reported to enhance the oxygen ion diffusivity and OSC of ceria [56] and $Ce_{1-x}Zr_xO_2$ nanoparticles, respectively [57]. Hence, it would be expected that ceria cubes exhibit higher reducibility compared to rods and particles. We however observed no relation between the overall catalysts reducibility in hydrogen (Table 4.2) and lattice microstrain in ceria nanoshapes (Table 4.1). This further supports the suggestion that the low temperatures (below 600°C) reduction in H_2 causes removal of exclusively surface oxygen.

Catalysts were characterized under identical conditions and tested under identical conditions, allowing searching for correlations between structural properties and corresponding catalytic activity in RWGS. Increasing lattice microstrain (Table 4.1) seemingly correlates with the observed catalytic activity of these nanoshapes in RWGS (Figure 4.5b); cubes are more active per surface area and contain clearly higher micro-strain. Similar correlations between lattice microstrain and catalytic activity for CO oxidation and WGS have been reported for doped ceria nanoparticles of irregular morphology [58,59] and supported ceria nanoshapes [27]. Theoretical simulations predicted increasing catalytic activity of ceria nanorods in CO oxidation with increasing lattice microstrain [60]. It has been suggested that increasing microstrain enhances active metal – ceria support interaction, resulting in improved dispersion of the active phase, stabilization of the active metal species in a lower valence state and enhanced overall reducibility [27,61]. Supported ceria cubes were moreover reported to possess lower lattice microstrain and corresponding lower catalytic activity in WGS compared to rods [27]. This has been attributed to low stability of (100) crystal planes enclosing cubes compared to relatively more stable (111) surface terminations of rods. Stable catalytic performance of ceria cubes in RWGS (Figure 4.4) suggests that the cubic shape and surface termination are stable under reaction conditions in this study.

For detailed identification of the exposed crystal facets for the three studied ceria nanoshapes, we refer to work previously reported by our group [18]. AC-HRTEM studies providing sub-Angstrom resolution, higher than previously reported [22,24] clearly revealed (111) crystal planes exposed at ceria rods and particles [25,31,62,63] whereas ceria cubes are enclosed by mainly (100) facets [18]. These ceria nanoshapes exhibited exactly the same trends in activity per surface area for WGS reaction (decreasing from ceria cubes to rods and finally particles) as reported in this study on RWGS reaction (Figure 4.5b) [18]. This result is expected based on the principle of the microscopic reversibility [18]. WGS has been suggested in literature to proceed *via* active hydroxyl species (–OH) on the ceria surface [64]. The observed correlation between lattice micro-strain (Table 4.1) and catalytic activity in (R) WGS (Figure 4.5b) hence might originate from increased an reactivity of reactive -OH species and/ or other surface intermediates on the strained ceria surfaces. However, this is clearly not supported by theoretical calculations, predicting that lattice microstrain has no effect on the reactivity of hydroxyl species terminating ceria surface [48]. Ceria cubes, exposing (100) facets, exhibit distinct –OH bands with discrete interaction with CO, compared to rods and octahedra, resulting in enhanced reactivity in WGS, as reported by our group [18].

The order of the catalytic activity: cubes > rods ~ particles (Figure 4.5b) is moreover consistent with the results reported for oxidation of hydrogen and ethanol over pure and supported ceria nanoshapes [36,37]. Fundamental studies in addition revealed higher inherent reactivity of (100) crystal planes of ceria for methanol [65], water [66], acetaldehyde [67] and acetic acid [68] compared to (111) facets, though under very different conditions compared to realistic reaction conditions. This has been attributed to the lower coordination numbers in (100) facets, inducing higher reactivity of both cerium and oxygen at (100) ceria surfaces compared to (111) facets [69]. Results presented in this study suggest that higher reactivity of ceria cubes in RWGS is due to the superior inherent reactivity of (100) crystal planes enclosing cubes, contrary to less inherently reactive (111) facets enclosing rods and particles in RWGS. Although catalytic activity apparently correlates with the lattice micro-strain, it remains unclear whether this relationship is causal. Lattice micro-strain might well be a consequence of the specific crystal structure including the surface termination, instead of cause of the observed prominent activity of ceria cubes compared to rods and particles in RWGS.

4.4 CONCLUSION

Cerium oxide catalysts of distinct morphology, *i.e.* cubes, rods, and particles of irregular shape, were characterized and investigated for reverse water gas shift reaction (RWGS). The nanoshapes as prepared differ in bulk-defect-concentration; high defect concentrations induce high concentrations of oxygen vacancies in the surface as evidenced by low amount of oxygen that can be removed from the surface via reduction. Catalytic testing under differential conversion of CO_2 revealed superior catalytic activity of ceria cubes per m^2 as compared to rods and particles. Catalytic activity of these catalysts in RWGS reaction exhibited an apparent correlation with lattice microstrain, however, any causal relationship remains unclear. Results presented in this study suggest that superior catalytic activity of ceria cubes in RWGS in caused by highly inherently reactive (100) facets exposed at cubes compared to relatively inert (111) crystal planes enclosing rods and particles.

APPENDIX 4

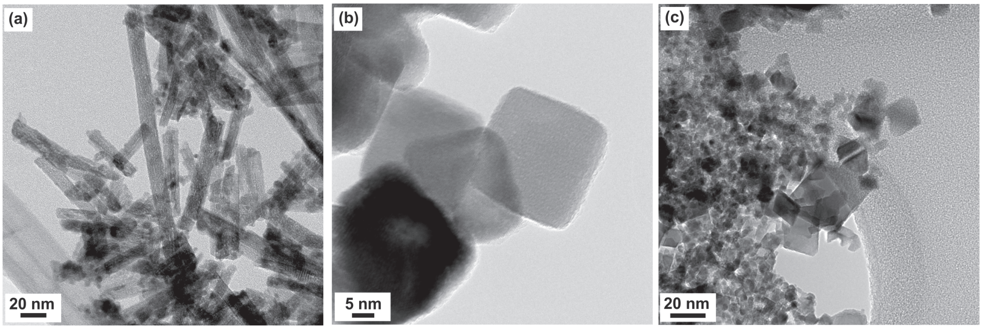

Figure A4.1. TEM images of ceria rods (a), cubes (b), and particles (c) as reported in Chapter 3 [38].

BIBLIOGRAPHY

1. X. Xiaoding, J.A. Moulijn, Energy Fuels 10 (1996) 305-325.
2. W. Wang, S. Wang, X. Ma, J. Gong, Chem. Soc. Rev. 40 (2011) 3703–3727.
3. G. Towler, S. Lynn, Chem. Eng. Sci. 49 (1994) 2585-2591.
4. S.E. Park, S.C. Han, J. Ind. Eng. Chem. 10 (2004) 1257-1269.
5. M.B. Ansary, S.E. Park, Energy Environ. Sci. 5 (2012) 9419-9437.
6. D.S. Newsome, Catal. Rev. 21 (1980) 275-318.
7. D. Moon, Catal. Surv. Asia 12 (2008) 188-202.
8. W. Ruettinger, O. Ilinich, R.J. Farrauto, J. Power Sources 118 (2003) 61-65.
9. C. Rhodes, G.J. Hutchings, A.M. Ward, Catal. Today 23 (1995) 43-58.
10. T. Tabakova, V. Idakiev, D. Andreeva, I. Mitov, Appl. Catal. A: General 202 (2000) 91-97.
11. R.M. Navarro, M.A. Pena, J.L.G. Fierro, Chem. Reviews 107 (2007) 3952-3991.
12. A. Trovarelli, Catal. Rev.-Sci. Eng. 38 (1996) 439-520.
13. C.J. Zhang, A. Michaelides, D.A. King, S.J. Jenkins, Phys. Rev. B 79 (2009) 75433.
14. S. Babu, R. Thanneeru, T. Inerbaev, R. Day, A.E. Masunov, A. Schulte, S. Seal, Nanotechnology 20 (2009) 85713.
15. M.V. Ganduglia-Pirovano, A. Hofmann, J. Sauer, Surf. Sci. Rep. 62 (2007) 219-270.
16. T.X.T. Sayle, S.C. Parker, D.C. Sayle, Phys. Chem. Chem. Phys. 7 (2005) 2936-2941.
17. J.A. van Bokhoven, ChemCatChem 1 (2009) 363-364.
18. S. Agarwal, L. Lefferts, B.L. Mojet, D.A.E. Ligthart, E.J.M. Hensen, D.R.G. Mitchell, W.J. Erasmus, B.G. Anderson, E.J. Olivier, J.H. Neethling, A.K. Datye, ChemSusChem 6 (2013) 1898-1906.
19. K. Zhou, Y. Li, Angew. Chem. Int. Ed. 51 (2012) 602-613.
20. C. Sun, H. Li, L. Chen, Energy Environ. Sci. 5 (2012) 8475-8505.
21. J. Zhang, H. Kumagai, K. Yamamura, S. Ohara, S. Takami, A. Morikawa, H. Shinjoh, K. Kaneko, T. Adschiri, A. Suda, Nano Lett. 11 (2011) 361-364.
22. H.X. Mai, L.D. Sun, Y.W. Zhang, R. Si, W. Feng, H.P. Zhang, H.C. Liu, C.H. Yan, J. Phys. Chem. B 109 (2005) 24380-24385.
23. Tana, M. Zhang, J. Li, H. Li, Y. Li, W. Shen, Catal. Today 148 (2009) 179-183.
24. K. Zhou, X. Wang, X. Sun, Q. Peng, Y. Li, J. Catalysis 229 (2005) 206-212.
25. X. Liu, K. Zhou, L. Wang, B. Wang, Y. Li, J. Am. Chem. Soc. 131 (2009) 3140-3141.
26. L. Liu, Y. Cao, W. Sun, Z. Yao, B. Liu, F. Gao, L. Dong, Catal. Today 175 (2011) 48-54.
27. R. Si, M. Flytzani-Stephanopoulos, Angew. Chem. Int. Ed. 47 (2007) 2884-2997.
28. Z. Wu, M. Li, S.H. Overbury, J. Catal. 285 (2012) 61-73.
29. Q. Dai, H. Huang, Y. Zhu, W. Deng, S. Bai, X. Wang, G. Lu, Appl. Catal. B: Environ 117-118 (2012) 360-368.
30. M. Li, Z. Wu, S.H. Overbury, J. Catal. 306 (2013) 164-176.
31. S. Wang, L. Zhao, W. Wang, Y. Zhao, G. Zhang, X. Ma, J. Gong, Nanoscale, 5 (2013) 5582-5588.
32. Z. Wu, M. Li, D.R. Mullins, S.H. Overbury, ACS Catal. 2 (2012) 2224-2234.
33. A.K.P. Mann, Z. Wu, F.C. Calaza, S.H. Overbury ACS Catal. 4 (2014) 2437-2248.
34. C. Sun, L. Chen, Eur. J. Inorg. Chem (2009) 3883-3887.
35. J. Lv, Y. Shen, L. Peng, X. Guo, W. Ding, Chem. Commun. 46 (2010) 5909–5911.
36. T. Dasaunay, G. Bonura, V. Chiodo, S. Freni, J.-P. Couzinie, J. Bourgon, A. Ringuede, F. Labat, C. Adamo, M. Cassir, J. Catal. 297 (2013) 193-201.
37. H. Li, G. Qi, Tana, X. Zhang, W. Li, W. Shen, Catal. Sci. Technol. 1 (2011) 1677-1682.
38. M. Kovacevic, S. Agarwal, B.L. Mojet, J.G. van Ommen, L. Lefferts, Appl. Catal. A: General 505 (2015) 354-364.
39. H.S. Nalwa, Handbook of nanostructured materials and nanotechnology, Academic press, 1999.
40. V.L. Tellkamp, M.L. Lau, A. Fabel, E.J. Lavernia, Nonostruct. Mater. 9 (1996) 489-492.
41. Q. Yuan, H.-H. Duan, L.-L. Li, L.-D. Sun, Y.-W. Zhang, C.-H. Yan, J. Colloid Interface. Sci. 335 (2009) 151-167.
42. M. Hirano, E. Kato, J. Am. Ceram. Soc. 79 (1996) 777-780.
43. M. Hirano, E. Kato, J. Am. Ceram. Soc. 82 (1999) 786-788.

44. C. Sun, H. Li, H. Zhang, Z. Wang, L. Chen, Nanotechnology 16 (2005) 1454-1463.
45. S. Meriani, S. Spinolo, Powder Diffr. 2 (4) (1987) 255-256.
46. Z. Wu, M. Li, J. Howe, H.M. Meyer III, S.H. Overbury, Langmuir 26 (2010) 16595-16606.
47. Y. She, Q. Zheng, L. Li, Y. Zhan, C. Chen, Y. Zheng, X. Lin, Int. J. Hydrogen Energy, 34 (2009) 8929–8936.
48. D. Ma, Z. Lu, Y. Tang, T. Li, Z. Tang, Z. Yang, Phys. Lett. A 378 (2014) 2570–2575.
49. J.-M. Costantinia, A. Kahn-Harari, F. Beuneu, F. Couvreur, J. Appl. Phys 99 (2006) 123501-123507.
50. C. Sun, H. Li, Z.X. Wang, L. Chen, X. Huang, Chem. Lett. 33 (2004) 622-623.
51. W.H. Weber, K.C. Hass, J.R. McBride, Phys. Rev. B 48 (1993) 178-185.
52. I. Kosacki, T. Suzuki, H.U. Anderson, P. Colomban, Solid State Ionics 149 (2002) 99-105.
53. J.E. Spanier, R.D. Robinson, F. Zhang, S.W. Chan, I.P. Herman, Phys. Rev. B 64 (2001) 245407-8.
54. G. Ranga Rao, Bull. Mater. Sci. 22 (1999) 89-94.
55. J.Z. Shyu, K. Otto, J. Catal. 115 (1989) 16-23.
56. M.J. Rushton, A. Chroneos, Sci. Reports 4 (2014) 6068.
57. R. Si, Y.W. Zhang, S.J. Li, B.X. Li, C.H. Yan, J. Phys. Chem. B 108 (2004) 12481-12488.
58. L. Lei, Z. Ying-Ying, C. Chong-Qi, S. Yu-Sheng, L. Xing-Yi, Z. Qi, Acta Phys. -Chim. Sin. 25 (2009) 1397-1404.
59. P. Sudarsanam, B. Mallesham, D.N. Durgasri, B.M. Reddy, RSC Adv. 4 (2014) 11322-11330.
60. T.X.T. Sayle, M. Cantoni, U.M. Bhatta, S.C. Parker, S.R. Hall, G. Mobus, M. Molinari, D. Reid, S. Seal, D.C. Sayle, Chem. Mater 24 (2012) 1811-1821.
61. S.Y. Yao, W.Q. Xu, A.C. Johnston-Peck, F.Z. Zhao, Z.Y. Liu, S. Luo, S.D. Sensanayke, A. Martinez-Arias, W.J. Liu, J.A. Rodriguez, Phys. Chem. Chem. Phys. 16 (2014) 17183-1795.
62. N. Ta, J.J. Liu, S. Chena, P.A. Grozier, Y. Li, A. Chen, W. Shen, J. Am. Chem. Soc. 134 (2012) 20585-20588.
63. N.J. Lawrence, J.R. Brewer, L. Wang, T.-S. Wu, J. Wells-Kingsbury, M.M. Ihrig, G. Wang, Y.L. Soo, W.-N. Mei, C.L. Cheung, Nano Lett. 11 (2011) 2666-2671.
64. K.G. Azzam, I.V. Babich, K. Seshan, L. Leffers, J. Catal 251 (2007) 153-162.
65. D.R. Mullins, P.M. Albrecht, Langmuir 29 (2013) 4559-4567.
66. M. Molinari, S.C. Parker, D.C. Sayle, M.S. Islam, J. Phys. Chem. C 116 (2012) 7073-7082.
67. D.R. Mullins, P.M. Albrecht, J. Phys. Chem. C 117 (2013) 14692-14700.
68. D.R. Mullins, P.M. Albrecht, F. Calaza, Top. Catal. 56 (2013) 1345-1362.
69. A.K.P. Mann, Z. Wu, S.H. Overbury in: Catalysis by Materials with Well-Defined Structures (Ed: Z. Wu, S.H. Overbury), pp.71-97, Elsevier, Amsterdam, 2015.

5

CONCLUSIONS AND OUTLOOK

This chapter presents the main conclusions of the work presented, and provides a perspectives on future research.

5.1 CONCLUSIONS

Styrene production via ethylbenzene dehydrogenation (EBDH) is one of the ten most important petrochemical processes [1]. Possessing highly reactive double bond which facilitates self-polymerization and polymerization with other monomers, styrene is the fourth utmost essential bulk monomer following ethene, propene and terephthalic acid, respectively [2]. Its global demand was 27 Mt/a (in 2010), while capacity utilization rates have been predicted to grow further by 2019 [2].

In this thesis we report on the structure-activity relationship for CO_2 mediated EBDH over tailored cerium oxide nanoparticles employed as model catalysts. Results presented contribute in extending the scope of the reactions investigated so far over cerium oxide catalysts of well-defined morphologies from small model compounds (CO, H_2, CH_4) towards more industrially relevant applications and more complex reactants (such as ethylbenzene); hence in generalizing the concept of the "shape and morphology effects in ceria catalysis".

Concept of using CO_2 as a soft/ mild oxidant is based on the thermodynamic calculations revealing clearly higher styrene yield at equilibrium when reverse water gas shift (RWGS) reaction is coupled with ethylbenzene dehydrogenation as compared to direct (conventional) dehydrogenation [3]. CO_2 mediated EBDH has been for the first time probed over cerium oxide catalysts. RWGS reaction has not been studied over ceria nanoparticles of distinct morphology before, to the best of our knowledge, though affirmative results for ceria cubes as compared to rods and octahedra in a reverse reaction, WGS have been recently reported by the group of Lefferts [4].

There is ample evidence in literature that ceria acts via a Mars Van Krevelen, MvK mechanism [5] in oxidative dehydrogenation reactions, in which the rate determining step is commonly abstraction of an oxygen ion by a substrate (hydrocarbon) and creation of an oxygen vacancy at the catalyst's surface/ lattice. EBDH has been suggested to proceed via a MvK mechanism over cerium oxide nanoparticles in presence of N_2O [6]. Apparently, reactions proceeding via a MvK mechanism show morphology dependant behaviour over ceria catalysts [7].

According to the Wolf's rule the crystal planes exposed at the surfaces of a crystallite depend on its morphology [8]. Experimental and theoretical studies reveal that ceria cubes expose mainly (100) crystal planes while rods and octahedra, polyhedra, or spheres exhibit primarily (111) facets [9,4]. These are moreover characterized by distinct cerium and oxygen ion coordination in the lattice [10,11] further clearly impacting the energy required for an active oxygen ion abstraction/ oxygen vacancy formation: (110) < (100) < (111) at these facets [12]. Stabilities of these surfaces in addition, clearly differ exhibiting the trend: (100) < (110) < (111) [13]. Therefore, distinct inherent red-ox, (acid-base) and catalytic properties for cerium oxide catalysts of well-defined morphologies [7] is expected and has been recently demonstrated in e.g. *WGS* [14] and oxidation of hydrogen, carbon monoxide and acetaldehyde [15,16,17].

Zirconia (*Zr*) is commonly employed ceria dopant used to enhance low temperature oxygen storage capacity (*OSC*) in the ceria lattice [18]. **First part** of the thesis focuses on the catalytic activity of zirconia doped ceria for CO_2 mediated EBDH. A series of $CeZrO_x$

catalysts was prepared by calcining hydrothermally obtained precipitate at increasing temperature in the flowing air. All the samples exhibited a sharp activity decline (within 120 min TOS) which we further attributed to the initial depletion of active oxygen species favoring formation of by-products in addition to styrene. Catalyst characterization by HRSEM, XRD and Raman spectroscopy, revealed respectively a morphology transition from regular cubic to spherical with increasing calcination temperature, an average crystallite diameter increase and oxygen vacancy annihilation. Gradual catalysts activity decline expressed per surface area (compared for all the samples at 240 min TOS) suggests that superior catalytic activity of these nanoshapes originates from the (100) crystal planes exposed at cubes which morphology is still preserved at the lowest calcination temperature. These facets exhibit a higher abundancy and greater intrinsic reactivity of oxygen vacancies as compared to (111) facets enclosing $CeZrO_x$ spheres.

In chapter three we report on the effects of ceria morphology: rods, cubes and particles as well as the effects of the CO_2 addition on the catalytic activity of pure ceria catalysts in EBDH. Presence of CO_2 resulted in an enhanced active oxygen species availability via a Mars Van Krevelen mechanism, resulting in a prolonged catalysts activity, and minor styrene selectivity as compared to in absence of CO_2. CO_2 however shows no effect on the catalytic activity after the stabilization. We used Raman spectroscopy as a finger print technique to characterize the degree of lattice distortion/ reduction in the spent ceria nanoshapes. Raman results revealed a relation between the abundancy of oxygen ions extracted by EB in absence of CO_2, catalytic activity per surface area, and the degree of the fluorite lattice distortion/ oxygen deficiency in the spent ceria catalysts. Ceria cubes exposing mainly (100) crystal planes exhibited clearly higher abundancy of lattice oxygen species extracted by EB initially, higher lattice distortion and higher activity in EBDH as compared to ceria rods and particles enclosed by (111) facets of higher inherent stability. Interestingly, ceria cubes preserve remarkably higher activity as compared to rods and particles in stable operation, clearly indicating that selective styrene formation proceeds at partially reduced surfaces generated upon O species removal via non-selective EB conversion pathways.

In chapter four ceria model catalysts of distinct morphology: cubes, rods and particles were investigated for the reverse water gas shift reaction (RWGS). Temperature programmed reduction in H_2 (H_2-TPR) and Raman spectroscopy results indicated lower reducibility of the nanoshapes possessing higher bulk/ surface oxygen deficiency. Catalytic testing under differential conversion of CO_2 revealed superior catalytic activity of ceria cubes for RWGS expressed per surface area as compared to rods and particles. Remarkably, all the catalyst exhibited rather stable operation, minor deactivation was observed in all cases. Catalytic activity further exhibited an apparent correlation with the lattice microstrain, however any causal relationship remained unclear. WGS has been suggested previously to proceed *via* active hydroxyl species (–OH) on the ceria surfaces [19]. Ceria cubes, exposing (100) facets, were found to exhibit discrete interaction with CO, compared to rods and octahedra, resulting in enhanced reactivity in WGS [3]. Results presented in this study suggest that superior catalytic activity of ceria cubes in RWGS is caused by highly inherently reactive (100) facets exposed at ceria cubes contrary to relatively inert (111) crystal planes enclosing rods and particles.

CO_2 mediated EBDH has been used in this study solely as a model reaction to assess the inherent reactivity of various ceria crystal planes exposed at cerium oxide nanoparticles of distinct morphology. Results presented in this thesis revealed that addition of CO_2 apparently has no effect on the catalytic performances of these ceria nanoshapes (activity/ selectivity/ stability) in EBDH once catalysts attain the stable oxidation state and a semi-steady conversion. However, longer time on stream experiments would be clearly required to examine the real catalytic performances of these ceria nanoshapes [20]. Recent work in the group of Makee clearly demonstrated that 5 h time-on-stream is relatively short time to predict the performance of various catalytic systems in EBDH and might be a wrong performance indicator under the practically relevant time on stream [20,21].

Moreover, the initial activity decay in CO_2 mediated EBDH should be attributed primarily to the adjustment of the catalysts' oxidation state. Real catalysts deactivation due to the excessive coke deposition is expected to occur at longer time on stream (> 20 h) [20]. Interestingly, clear absence of coke deposits on cerium oxide surfaces in presence of CO_2 has been recently demonstrated [22]. Hence, it can be expected that extensive coke formation at the surface of these ceria nanoshapes at longer time on stream might be limited. In addition, very stable conversion after the initial activity decrease might suggest that these levels would be maintained at longer time on stream. In order to assess if these ceria cubes show a promise for a further catalyst development, longer time on stream measurements (preferably at conversion/ weight hourly space velocity/ EB dilution closer to a commercially employed would be desirable. This was, however, beyond the scope of the current thesis.

The effects of CO_2 addition for EBDH have been extensively discussed in literature [23]. Positive [24,25,26], negative [27] as well as the absence of any effects [20] of the CO_2 addition to the inert/steam employed as a carrier on the catalytic performances of various catalytic systems in EBDH have been reported. However, as indicated by C.Nederlof [21] all the catalysts investigated so far exhibited several times lower activity compared to the commercially employed K-Fe based catalyst for a steam-aided dehydrogenation under comparable conditions. Furthermore, all the catalysts displayed a severe deactivation due to the extensive carbonaceous deposition with the only exception of VSbO on a magnesium doped alumina [28]. Cerium oxide (in presence of CO_2) shows a promise in that respect, though stability tests are clearly pending [22].

CO_2 mediated EBDH is relatively new topic, hence the benefits of the CO_2 addition for EBDH instead of conventionally used steam are not yet fully evaluated. CO_2 can replace conventionally used steam for heat supply circumventing the steps of it's condensation and re-evaporation prior to the steam recycle. It has been suggested that hence lowered energy consumption leads to potential energy savings up to 60% [29,30]. However, *overall* process improvements will be time-consuming and perhaps "neither rewarding nor worthwhile" [21]. In other words, cost of CO_2 supply, separation, compression, recycling and CO conversion still limits the potential of CO_2 mediated EBDH to becoming a feasible alternative to conventional (steam aided) dehydrogenation [21].

Cerium oxide is a well known promoter of the commercial Fe-K based catalysts used in the amounts of 5 - 60 mass. %, enhancing catalytic activity [31]. It has been demonstrated that addition of cerium clearly decreases the activation energy for styrene formation over

K-Fe catalysts [32]. Enhancement of the catalytic activity of a commercial catalyst in presence of ceria has been extensively discussed by Trovarelli et al. However fundamental insights of the reactivity of ceria in EBDH are still missing.

Several research groups, including ours, focused on getting fundamental understanding of the reactivity of oxygen deficient ceria surfaces in EBDH (in presence of CO_2 [22], O_2 [33], N_2O [34]) reporting interestingly on high specific rates of styrene formation [33]. However, catalytic testing was performed under high EB dilution in these studies, hence it cannot be directly compared with the activity of a commercial catalyst to assess the potential of using these ceria catalysts in EBDH. Nevertheless, CO_2 addition has been demonstrated clearly to minimize/ inhibit the coke deposition at the ceria surfaces [22]. Therefore, cerium oxide is certainly a promising candidate for the CO_2 mediated EBDH.

In presence of other oxidants such as O_2, cerium oxide on the other hand shows high activity (comparable with the best catalyst in literature, however at the selectivity of about 84%). However, It should be noted that stability of ceria still remains an issue. As observed by Trovareli *et al.*, after the number of runs catalyst undergo severe sintering [32].

Below are presented the recommendations concerning further fundamental studies.

5.2 GENERAL RECOMMENDATIONS

5.2.1 High surface area cubes

Based on the results presented in this thesis and the work reported by our group [3], cerium oxide cubes are highly promising catalysts as compared to rods and particles/ octahedra. These are characterized by highly inherently reactive (100) crystal planes exposed which are about two times more reactive (in ethylbenzene dehydrogenation, reverse water gas shift and water gas shift reaction) per surface area as compared to (111) facets enclosing rods and particles/ octahedra. As commonly reported, ceria cubes however possess significantly lower surface area as compared to rods/ wires.

It would be highly desirable to obtain cerium oxide cubes of higher specific surface area than usually stated employing for instance organic templates- (e.g. oleic acid) and microwave assisted- hydrothermal methods, both resulting in ceria cubes of uniform crystallite size (~4 nm), and enhanced surface area [35,36,37].

5.2.2 Ceria nanotubes

1D tubular nanoshapes received particular attention since the discovery of carbon nanotubes by *Iijima et al.* [38]. Cerium oxide nano*tubes* however, have not been extensively explored in catalysis as compared to other ceria tailored morphologies. Strikingly, theoretical predictions reveal negative strain energies at these surfaces clearly indicating high stability of these exclusively exposed (100) crystal planes at ceria nano*tubes* [39]. We recommended to investigate these 1D ceria or $CeZrO_x$ nanoshapes [40] for reactions proceeding *via* a *Mars Van Krevelen* mechanism, e.g. CO_2 mediated ethylbenzene dehydrogenation.

Our preliminary results regarding ceria nanotubes synthesis and characterization are presented in Appendix 5. Catalytic activity of these ceria nano*tubes* per m^2 was almost identical with the activity of $CeZrO_x$ cubes probably suggesting that (100) crystal planes predominantly encloses both morphologies.

Interestingly, by modifying the procedure described in [25] by using ZrO_2 dopants of various structure, $CeZrO_x$ nanoshapes of clearly distinct morphologies can be obtained (Appendix 5, Figure A5.1). HRTEM would be needed to confirm nanotubes formation. We recommend to study more into depth how structure and surface area of the dopant (zirconia) govern the resulting morphology and aspect ratio of thus obtained $CeZrO_x$ crystallites (Figure A5.1).

5.2.3 Cerium nanocubes with enhanced defect sites abundancies

Exposing ceria nanoshapes to low oxygen pressure has been reported to enhance significantly oxygen deficiency at low index ceria facets. So far results have been reported for ceria rods as compared to nanoparticles of irregular morphology. We suggest to investigate *in situ* effects of low pressure pretreatments (inducing controlled desorption of molecular oxygen and controlled induced oxygen deficiency on facets exposed) on ceria cubes/ nanotubes and to correlate catalytic activity of thus engineered (100) surfaces in EBDH with CO_2. This would contribute to better understanding on the role of vacancies in ethylbenzene and CO_2 activation.

For the low pressure thermal activation of ceria nanoshapes we refer to studies by *Lawrence et al.* [41].

5.2.4 More detailed characterization of low-coordinated sites

We further recommend to characterize these low index ceria surfaces by infrared spectroscopy using CO as a probe molecule. Carbonyl formation at -192°C although at temperatures much lower than applied in the actual catalytic reaction proves to be a useful tool to distinguish between the Lewis acid sites of various coordinative unsaturation. Ce^{4+} sites of lower coordination are expected to exhibit stronger interaction with CO and bands at clearly higher frequencies (wavenumbers) as compared to these of the free gas phase CO molecule. To the best of our knowledge LT-FTIR characterization of tailored ceria nanoparticles at -192°C is still pending. Our preliminary results (Appendix 5, Figure A5.2) indicate a clear difference in spectra of $CeZrO_x$ tubes, cubes and spheres.

Likewise, pyridine desorption studies might be employed to estimate the strength/ quantity of acid/ basic sites at these ceria nanoshapes [42].

5.2.5 Swing experiments. Oxidation role of CO_2

Swing experiments with altering oxidation and reduction steps [43] with pure reductant (ethylbenzene) and oxidant (CO_2) in the feed are highly recommended to confirm *MvK* mechanism occurring in the oxidative dehydrogenation proposed in this thesis. Step response studies with ethylbenzene and CO_2 alternatively have been conducted over supported vanadium and iron catalysts by *Nederlof et al.* [44]. In addition we suggest to perform labeled CO_2 transition studies which would allow us to examine in any different pathways/ mechanism proceed between the various crystal planes in activating, dissociating CO_2. Similar work has been performed by *Bueno-López et al.* over pure and metal supported ceria nanoparticles of irregular morphology [45].

APPENDIX 5

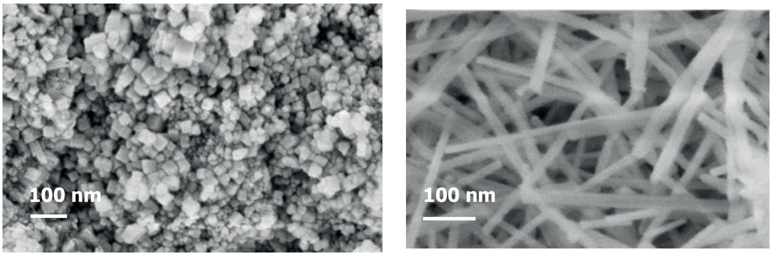

a) Monoclinic, low BET ZrO_2 dopant b) Tetragonal ZrO_2 dopant

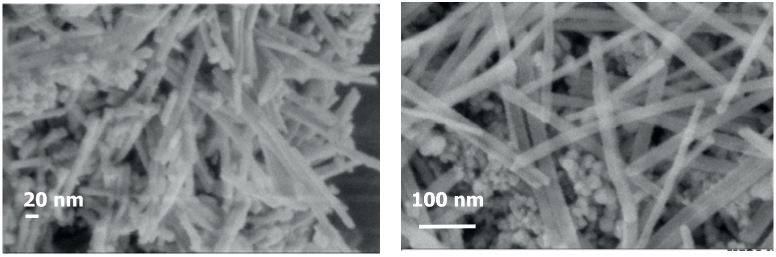

c) Monoclinic, high BET ZrO_2 dopant d) Tetragonal & monoclinic ZrO_2

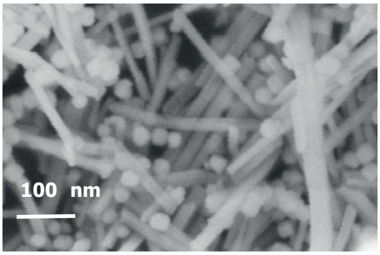

e) Yttrium stabilized ZrO_2 dopant

Figure A5.1 HRSEM images of $CeZrO_x$ nanoshapes obtained modifying the procedure described in [25] by using monoclinic, tetragonal and cubic zirconia dopant. $CeZrO_x$ cubes (a), tubes (b), rods (c) and mixture of tubes/ rods/ particles (d, e).

Experimental part LT-FTIR

IR spectra of adsorbed CO molecule are recorded on self-supported wafers of the catalyst (5-40 mg) with a Bruker Tensor 27 FTIR with a data point resolution of 4 cm^{-1}. The wafers were placed in a home-made IR transmission cell, similar as described by *Trionfetti et al.* [46]. Prior to CO exposure the samples were heated in flowing He (5°C·min^{-1}, 20 ml min) and kept at 450°C for 15 min. The samples were subsequently cooled down to liquid nitrogen temperature (LNT) in flowing He and exposed to 25% CO in He (20 ml·min^{-1}) for 45 min. The spectra were recorded prior to CO adsorption (used as baseline for the spectra presented in Figure A5.2) and during both CO adsorption and desorption during 90 min at LNT. Desorption spectra are presented below.

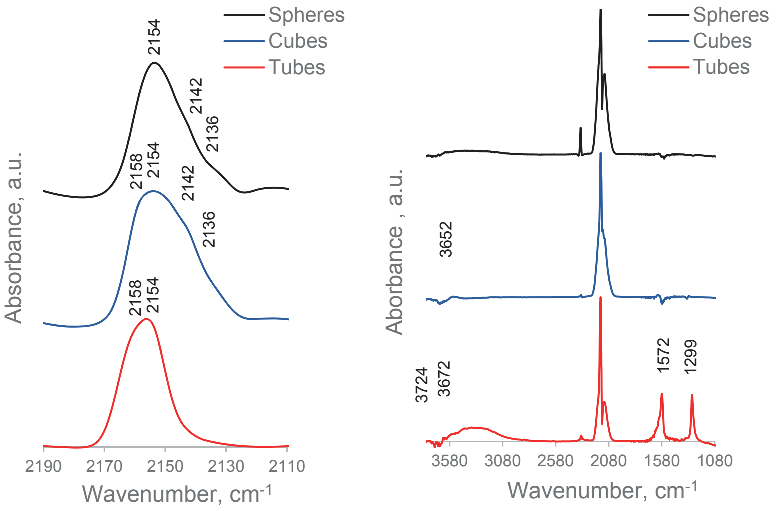

Figure A5.2. Baseline corrected *in-situ* FTIR-CO spectra at LNT of CeZrO$_x$ spheres, cubes, and tubes, (a) spectra detail 2110-2190 cm^{-1} additionally corrected for the gas-phase molecular CO vibration; (b) full spectra not corrected for the gas-phase molecular CO vibration.

Preliminary LT-FTIR results

In situ LT-FTIR-CO spectra of CeZrO$_x$ spheres, cubes and tubes are presented in Figure A5.2 a and b. Preliminary results indicate that ceria tubes and cubes possess unique band at 2158 cm^{-1} in addition to the band at 2154 cm^{-1} present in all the three nanoshapes (Figure A5.2a). This band has been previously assigned to CO-OH interaction [47]. It also might originate from the interaction of CO with the Ce^{4+} sites of lower coordination causing the shift in the CO-Ce^{4+} frequency towards higher wavenumbers as expected at (100) surfaces of lower coordination exposed at tubes and cubes compared to (111) crystal planes exposed at spheres. Band at 2157 cm^{-1} has been previously reported to be associated with defects associated with Ce^{3+} sites [48].

First assumption that this band is due to the interaction of CO with OH groups (H bonded CO [49] at ceria tubes (even present after the pre-treatment at 450°C in He) is in line with the band at 1299 cm^{-1} suggesting existence of formate species [29] which has, however, been observed only in case of ceria tubes. Moreover, this ceria morphology exhibited clearly different ratio of isolated *vs*. associated –OH groups and seemingly various amount of consumed –OH groups (negative signals observed at 3652 and at 3672 and 3724 cm^{-1}, for cubes and tubes respectively (Figure A5.2b)). Bands at 1400-1445 cm^{-1} are not relevant due to the contribution of gas phase molecular vibration.

BIBLIOGRAPHY

1. B.M. Reddy, D.S. Han, N. Jiang, S.E. Park, Catal. Surv. Asia 12 (2008) 56-69.
2. http://www.prweb.com/releases/2015/07/prweb12839982.htm, accessed December 2015; C. Nederlof, Catalytic dehydrogenations of ethylbenzene to styrene, PhD Thesis, pp. 2, TU Delft, Delft, 2012.
3. G. Towler, S. Lynn, Chem. Eng. Sci. 49 (1994) 2585-2591.
4. S. Agarwal, L. Lefferts, B.L. Mojet, D.A.E. Ligthart, E.J.M. Hensen, D.R.G. Mitchell, W.J. Erasmus, B.G. Anderson, E.J. Olivier, J.H. Neethling, A.K. Datye ChemSusChem 6 (2013) 1898-1906.
5. P. Mars, D.W. van Krevelen, Spec. Suppl. Chem. Eng. Sci. 3 (1954) 41–59.
6. B. Murugan, A.V. Ramaswamy, J. Am. Chem. Soc. 129 (2007) 3062-3063.
7. A.K.P. Mann, Z. Wu, S.H. Overbury in: Catalysis by Materials with Well-Defined Structures (Ed: Z. Wu, S.H. Overbury), pp. 71-97, Elsevier, Amsterdam, 2015.
8. G. Wulff, Z. Kristallogr. 34 (1901) 449-530.
9. Catalysis by materials with well-defined structures, (Ed: Z. Wu, S.H. Overbury), Elsevier, 2015, Amsterdam.
10. M.V. Ganduglia-Pirovano, A. Hofmann, J. Sauer, Surf. Sci. Rep. 62 (6) (2007) 219–270.
11. Z. Wu, M. Li, D.R. Mullins, S.H. Overbury, ACS Catal. 2 (11) (2012) 2224–2234.
12. T.X.T. Sayle, S.C. Parker, D.C. Sayle, Phys. Chem. Chem. Phys 7 (2005) 2936-2941.
13. M. Nolan, S. Grigoleit, D.C. Sayle, S.C. Parker, G.W. Watson, Surf. Sci. 576 (2005) 217-229.
14. R. Si, M. Flytzani-Stephanopoulos, Angew. Chem. Int. Ed. 47 (2008) 2884-2997.
15. T. Dasaunay, G. Bonura, V. Chiodo, S. Freni, J.-P. Couzinie, J. Bourgon, A. Ringuede, F. Labat, C. Adamo, M. Cassir, J. Catal. 297 (2013) 193-201.
16. Z. Wu, M. Li, S.H. Overbury, J. Catal. 285 (2012) 61–73.
17. A.K.P. Mann, Z. Wu, F.C. Calaza, S.H. Overbury, ACS Catal. 4 (2014) 2437-2448.
18. Y. Madier, C. Descorme, A.M. Le Govic, D. Duprez, J. Phys. Chem. B 103 (1999) 10999-11006.
19. K. Azzam, I. Babich, K. Seshan, L. Lefferts, J. Catal. 251 (2007) 163-171.
20. C. Nederlof, F. Kapteijn, M. Makkee, Appl. Catal. A: Gen. 417-418 (2011) 163-173.
21. C. Nederlof, Catalytic dehydrogenations of ethylbenzene to styrene, PhD Thesis, TU Delft, Delft, 2012.
22. L. Zhang, Z. Wu, N.C. Nelson, A.D. Sadow, I.I. Slowing, S.H. Overbury, ACS Catal. 2015, 5, 6426–6435.
23. M. Bismillah Ansari, S.-E. Park, Energy Environ. Sci. 5 (2012) 9419.
24. N. Mimura, M. Saito,Catal. Lett. 58 (1999) 59.
25. D.R. Burri, K.M. Choi, D-S. Han, J.-B. Koo, S.-E. Park, Catal. Today 115 (2006) 242.
26. D.R. Burri, K.M. Choi, S.-C. Han, A. Burri, S.-E. Park, J. Mol. Catal. A: Chem. 2007, 269, 58.
27. T.Hirano, Appl. Catal. 26 (1986) 65-79.
28. B.M. Reddy, D.S. Han, N. Jiang, S.E. Park, Catal. Surv. Asia. 12 (2008) 56-69.
29. N. Mimura, I. Takahara, M. Saito, T. Hattori, K. Ohkuma, M. Ando, Studies in Surface Science and Catalysis, 114 (1988) 415.
30. N. Mimura, I. Takahara, M. Saito, T. Hattori, K. Ohkuma, M. Ando. Catal.Today 45 (1998) 61.
31. A. Murakami, H. Unei, m. Teranishi, m. Ohta, US Patent 5190906 (1993).
32. A. Trovarelli, C.de Leitenburg, M.Boaro, G.Dolcetti, Catal.Today 50 (1999) 353-367.
33. J. Xu, L.-C. Wang, Y.-M. Liu, Y. Cao, H.-Y. He, K.-N. Fan, Catal. Lett. 133 (2009) 307.
34. B. Murugan, A.V.Ramaswamy, J.Am.Chem.Soc. 129 (2007) 3062-3063.
35. S. Yang, L. Gao, J. Am. Chem. Soc. 128 (2006) 9330-9331.
36. J. Lv, T. Shen, L. Peng, X. Guo, W. Ding, Chem. Commun. 46 (2010) 5909-5911.
37. F. Gao, Q. Lu, S. Komrneni, J.Nanosci.Nanotechnol. 6 (12) (2006) 3812-3819.
38. S. Iijima, Nature 354 (1991) 56-58.
39. J.J. Plata, I. Ruiz-Tagle, A.M. Márquez, J. Fdez.Sanz, J. Phys.Chem.Lett. 3 (15) (2012) 2092–2096.
40. Y.-C. Chen, K.-B. Chen, C.-S. Lee, M.C. Lin, J. Phys. Chem. C 113 (2009) 5031-5034.
41. N.J. Lawrence, J.R. Brewer, L. Wang, T.-S. Wu, J. Wells-Kingsbury, M.M. Ihrig, G. Wang, Y.-L. Soo, W.-N. Mei, C.L. Cheung, Nano Lett. 11 (2011) 2666-2671.

42. M.I. Zaki, G.A.M. Hussein, S.A.A. Mansour, H.A. El-Ammawy, J. Mol. Catal. 51 (1989) 209-220.
43. C. Doornkamp, V. Ponec , J. Mol. Catal. A: Chemical 162 (2000) 19-32.
44. C. Nederlof, G. Talay, F. Kapteijn, M. Makkee, Appl. Catal. A: Gen. 423-424 (2012) 59-68.
45. A. Bueno-López, K. Krishna, M. Makkee, Appl. Catal. A: General 342 (2008) 144-14.
46. C. Trionfetti, New insight in oxidative conversion of alkanes: Exploring Li- promoted MgO catalysts and plasma micro-reactors, PhD Thesis, University of Twente, Enschede, 2008.
47. C. Binet, M. Daturi, J.-C. Lavalley, Catal. Today 50 (1999) 207-225.
48. M.I. Zaki, B. Vielhaber, H. Knözinger, J. Phys. Chem. 90 (1986) 3176-3183.
49. F. Romero-Sarria, A. Penkova, L.M. Martinez T., M.A. Centeno, K. Hadjiivanov, J.A. Odriozola, Appl. Catal. B: Environ. 84 (2008) 119–124.

SCIENTIFIC CONTRIBUTIONS

Publications

M. Kovacevic, R. Brunet Espinosa, L. Lefferts, B.L. Mojet, Calcination effects on $CeZrO_x$ geometry and styrene production from ethylbenzene, Appl. Catal.A: Gen. 469 (2014) 1-7.

M. Kovacevic, S. Agarwal, B.L. Mojet, J.G. van Ommen, L. Lefferts, The effects of morphology of cerium oxide catalysts for dehydrogenation of ethylbenzene to styrene, Appl.Catal. A Gen. 505 (2015) 354-364.

M. Kovacevic, B.L. Mojet, J.G. van Ommen, L. Lefferts, Effects of morphology of cerium oxide catalysts for reverse water gas shift reaction, Catal. Lett. 146 (2016) 770-777.

Oral presentation

M. Kovacevic, B.L. Mojet, L. Lefferts, Direct effect of ceria structure on styrene production from ethylbenene, NCCC-XIII, 5-7th March 2012, Netherlands.

Poster presentations

M. Kovacevic, B.L. Mojet, L. Lefferts, Direct effect of ceria morphology on styrene production, 15th ICC, 1st-6th July 2012, Munich, Germany.

M. Kovacevic, S. Agarwal, B.L. Mojet, L. Lefferts, Structure activity relationships for ceria in Ethylbenzene Dehydrogenation, NCCC-XII, 28th February – 2nd March 2011, Noordwijkerhout, Netherlands.

S. Agarwal, B.L. Mojet, M. Kovacevic, L. Lefferts, Tailored ceria nanoparticles for highly active OH species – Green future, NCCC-XII, 28th February – 2nd March 2011, Noordwijkerhout, Netherlands.

M. Kovacevic, L. Lefferts, Ethylbenzene to Styrene using CO_2 as a soft oxidant, NCCC-XI, 1st- 3rd March 2010, Noordwijkerhout , Netherlands.

S. Agarwal, B.L. Mojet, M. Kovacevic, L. Lefferts, How to enhance the activation of water on inorganic oxides?, 6th EFCATS summer school – Catalysis and surface science for renewables & energy, 13th - 19th September 2010, Izmir, Turkey.

M. Kovacevic, C. Huiskes, H.J.M. Bouwmeester L. Lefferts, Oxidative dehydrogenation of Ethylbenzene to Styrene using CO_2 as a soft oxidant, NCCC-X, 2nd - 4th March 2009, Noordwijkerhout, Netherlands.

ACKNOWLEDGMENTS

Work presented in this thesis would be impossible without the people who supported me. I would like to take this opportunity to acknowledge them.

Dear Leon, thank you very much for giving me the opportunity to perform my Ph. D. in your group. I am grateful for all the discussions, suggestions, remarks and all your efforts during the project. Thank you very much for all the challenging questions. I believe they helped me to develop thinking clearly and will be of use in the future. Thank you, Leon, for your detailed and prompt responses during the writing part of this thesis. Without that accomplishment of this Ph. D. would be impossible. I am grateful to Dr. Jan van Ommen, my assistant promoter for his contribution. Dear Jan, thank you very much for your availability, flexibility, for good ideas and inspiring discussions! Without your inputs and presence (mainly via emails) reaching to this stage would be impossible. I highly appreciate your efforts in following my research topic.

I would like to acknowledge the committee members for their inputs on the content of this thesis. I specially thank to Prof. M. Makkee for his detailed feedback on the content which certainly improved my perspective on this research. Dr. R. Terrorde, thank you very much for the fruitful discussions during ASPECT project meetings. I acknowledge ASPECT (Advanced Sustainable Processes by Engaging Catalytic Technologies) for the financial support.

I would like to thank Dr. B. L. Mojet for her contribution. Prof. Seshan, thank you for all the nice discussions, for your availability and support.

Bert, thank you very much for all your help in the lab, without you this work would not be possible. Thank you for our borrel evenings and happy times we shared.

I would like to acknowledge Roger Brunet Espinosa for his contribution to this thesis. Thank you Roger for the data collection and analysis during your master thesis project. Roald, thank you very much for translating the Summary of this thesis. I knew I always can count on your help. Keep up the good spirit and sharing the knowledge with others.

Igor and Jana, thank you for your friendly attitude, for our Slavic parties.

Dear Karin, thank you for all the lab work. I can still recall ordering the parts to start building my set-up. The frame was our first project. Thank you for asking: Kako si? and for all warm hugs. Those meant a lot to me. Dear Louise, thank you for inviting us often for cultural events and sharing some Sonia’s secrets and a balance records in your office.

Dear paranymphs, Inga and Liza, thank you for sharing a lot of this journey, for our wonderful horse-back riding lessons, dinners, Switzerland trip and much more. I think finally (!!) we can plan our girls’ trip to Greece.

My dear CPM colleagues, thanks for being a family to me. Fun in Enschede started with Cristiano, Davide and Anil. I can still recall our dinners in Antica Villa, Oldenzaal with Kumi, Vijay and Hrudya. Hrudya, thank you for your honest friendship in our Calslaan days. You were like a small sister to me. I wish you all the best in life in US. Dear Italians, it was such a great start. I still recall our twingo trip to Frankfurt and nights out in Paddy's :). I have no words to thank to Kumar and Vijay for their support and friendship.

Dearest Okice & Micko thank you very much for keeping the candle burning, for your real friendship. This summer, I guess, North Sea Jazz festival is ours. I have no words to thank you for everything!!! Dear Lucija and Alpi, thank you for constant support in the last months in all possible ways. Thank you for nice evenings out, kayaking, and much more. Our days in Amsterdam were simply wonderful.

Shilpa, ceria nanoshapes shaped our lives in many different ways. I still recall how happy we were some days and nights out in Enschede, our bike trips, Munich time, Groningen by car trip and more; you are specially dear to me, I am looking forward spending much more time with you and in the near future!

I would like to thank to my friend Ivana Lolin for her presence, inspiration, understanding and full support at any time. Thank you, Ivon for everything!

Bertolina, Gacia, it was great going out, shopping, and a bit complaining in Enschede. What else to do in between the catalytic testing measurements? Thank you for sharing a lot with me! I hope we will get a chance to spend much more time together in the near future. Zeljko, prijatelju, I really appreciate your willingness to share and help. I wish you all the best in future! Chris, it was “awesome”! Thank you for Duerningenstraat times, some long borrels, hard and happy times. But we know that a smoot sea never made a good sailor!

Dear Arturito, thank you for our lunches, hugs, cycling home together from our Meander, for teaching me how to dance. Thank you for your care and support. Masoud and Fatemeh, thank you dear people for cheering me up! If I could have more paranymphs, mate, you would be the one. Dennis, it was always nice discussing with you, thank you for our small chats in ME 364 and for tolerating some noise and complains.

Astrid, how happy I was when I moved to Beverwijk realizing you are close by in Zaandam. Thanks for very nice time together. Sonny boy, I really regret we did not spend more time together! My best wishes to you and your small family! Dear Rao, you are the next! Keep up the good work!

I would like to thank to other people I met during this journey. It is difficult not to forget someone. Thanks to Arie, Lianne, Lidy, Sabine, Maaike, Jacqueline, Kamilla, Kaisa, Chau, Chieh-Chao, Dejan, Marica, Sanja, Maksa, Anja, Bojan, Sale, Zarko, Uros, Gorica, Dragan,

Prasad, Bilge, Janet, Maurizio, Can, Laura, David, Masha, Ruben, Jouline, Songbo, Jose, Alvaro, Alfonso, Edit, Ana, Luis, Elif, Sergio, Zeynep, Tom, Can, Julian, David, Vincent, Nikolay, Oscar, Micheline, Ruben, Maria, Hirsa, Ana, Gina, Gerrit, Chantal, Jake, Derk, Pieter, Marcelino, Oana, Valerya, Eleni, Cem, Laura, Milica, Christine and Dejan.

Many thanks to Prof. Goran Boskovic, Prof. Erne Kis, Srdjan, Tamara, Ruzica, tetka Marija Popovic, my small sister Natasha, and to my dear friends Bojana, Jasna, Slavica, Marija, Dragana, Alenka, Jadranka and Tanja for their kind support.

Deepest gratitude goes to my family, to my mother Snezana Kovacevic for her unconditional love, unlimited support and infinite understanding.

Marijana Kovacevic
27th Apri 2016, Amsterdam.

Marijana Kovacevic was born in Belgrade, Serbia in 1979. She received her M. Sc. degree in October 2005 from the University of Novi Sad, Faculty of Technology, Department of Chemical Engineering. In January 2006 she joined the Laboratory for Physical Chemistry and Catalysis at the same University as a research scientist.
In February 2008 she started her Ph. D. degree at the University of Twente, The Netherlands in the Catalytic Processes and Materials group. Since August 2012 she works as a Process engineer in The Netherlands.
The outcome of her Ph. D. research is presented in this thesis.

ISBN 978-90-365-4130-5